Dissertation zur Erlangung des akademischen Grades
doctor rerum naturalium (Dr. rer. nat.)

Influencing pattern formation and localization through disorder

vorgelegt der
Naturwissenschaftliche Fakultät II - Chemie und Physik
der Martin-Luther-Universität Halle-Wittenberg

von
Lukas Jahnke

Halle (Saale), Mai 2009
Verteidigungstermin:
Halle (Saale), 25. November 2009

Gutachter:
1. Prof. Dr. Jan W. Kantelhardt (Betreuer)
2. Prof. Dr. Steffen Trimper
3. Prof. Dr. Michael Schreiber

FÜR
SONJA
TALEA
MADITA

Contents

I. Introduction 1

1. Structures of disordered systems 2
   - 1.1. Electronic materials 2
   - 1.2. Glasses and gels 5
   - 1.3. Complex networks 8

2. Dynamics of disordered systems 12
   - 2.1. Electronic dynamics 12
   - 2.2. Classical wave dynamics 15
   - 2.3. Reaction and diffusion dynamics 16

3. Pattern formation and localization 20
   - 3.1. Pattern formation 20
   - 3.2. Localization 23

II. Summary and discussion 33

III. Publications 41

4. Comparison of models and lattice-gas simulations for Liesegang patterns 42
   - 4.1. Introduction 42
   - 4.2. Experimental findings and empirical universal laws 43
   - 4.3. Models 45
   - 4.4. Lattice-gas simulations 55
   - 4.5. Summary and outlook 62

5. Consequences of fluctuations in Liesegang pattern formation 64
   - 5.1. Introduction 64
   - 5.2. Nucleation and growth model for Liesegang pattern formation 65
   - 5.3. Lattice-gas simulation 66
   - 5.4. Corrections to the mean-field spacing law 68
   - 5.5. Fluctuations due to thermal motion 69
   - 5.6. Fluctuations due to heterogeneous nucleation 70
   - 5.7. Summary and conclusion 72

6. Equidistant band formation of precipitation in a reaction-diffusion process 73

7. The effect of a small magnetic flux on the metal-insulator transition 79
7.1. Introduction 79
7.2. Model and finite-size scaling approach 80
7.3. Phase diagram and scaling behavior of the transition 83
7.4. The critical level spacing distribution 85
7.5. Summary and concluding remarks 86

8. Wave localization in complex networks with high clustering 87

9. Wave localization on complex networks 93
9.1. Introduction 93
9.2. Statistical properties of the spectra of complex networks 97
9.3. Complex networks with high clustering 103
9.4. Summary 108

Bibliography 109

Veröffentlichungen 123

Danksagung 125

Preface

A quantum leap in solid state physics was the understanding that macroscopic objects can be described using the symmetries of the Hamiltonian. For instance, if translational symmetry is present, the atomic structure of the macroscopic objects is described by the solution of a unit cell. Disorder, for example a random potential landscape, breaks translational symmetry. Other symmetries are untouched by disorder, such as orthogonal or unitary transformations of the Hamiltonian. Physicists in the seventies and eighties of the last century realized that phase transitions even in disordered solids can be described in a scaling ansatz. This scaling is due to the underlying symmetry of the Hamiltonian and is therefore universal. One type of phase transition in disordered solids is the disorder-induced metal-insulator transition. A metallic solid is transformed to an insulator by an increase of disorder. Therefore the initially extended electronic wave function localizes.

Disorder also has an impact on classical systems, for example, reaction-diffusion systems. Especially interesting is the effect of disorder and fluctuations in systems where ordering mechanisms occur, as in the case of phase separation of particles. In the last years, trend words as *self-assembly*, *self-organization*, and *pattern formation* were used to describe different kinds of ordering reactions. These are investigated driven by the motivation to design devices using reaction-diffusion dynamics. The Liesegang pattern formation is a prominent example, due to the simple descriptions of pattern distances and widths. Commonly, Liesegang patterns are described by mean-field approximations. In such scenarios, the concentrations of particles are approximated as smooth functions and the reaction is described by differential equations. In nature, fluctuations of the particle concentrations are present due to disorders such as defects, impurities etc. An important progress achieved in the last decade is the understanding that fluctuations do not necessarily destroy pattern formation. In contrary, they are able to enhance or induce pattern formation and order.

The publications presented in Part III are the core of this thesis. In Part I the general context of these publications is introduced, while in Part II they are summarized and discussed in relation with each other. Part I is divided into three chapters. In Chapter 1 different examples of compositionally and structural-topologically disordered systems are described, starting with percolation. Realizations of the tight-binding approximation for different types of disorders are introduced, for instance, the Anderson model, a binary alloy system, quantum percolation, and the random phase model. Gels and glasses are mesoscopic examples of structurally disordered systems. Their properties, especially their local structures, are described. At last, the general properties of complex networks are introduced with emphasis on the description of clustering.

In Chapter 2 the transport dynamics of particles in disordered systems are discussed. At first the tight-binding model for electron transport in disordered media is derived. Results for applications are presented, for example, for quantum percolation, and for the Anderson model with and without magnetic field. Furthermore it is shown that the tight-binding model is not only valid for quantum wave transport in disordered media, but also for classical waves. Finally reaction-diffusion dynamics are derived and discussed with focus on the influence of disorder.

Chapter 3 is devoted to the understanding of Liesegang pattern formation and the localization of electronic wave functions in disordered media. In the context of Liesegang pattern formation four important laws are introduced and mean-field predictions are discussed. The section on localization deals with a scaling ansatz to describe the metal-insulator transition. Additionally, a common statistical method is introduced called level spacing statistic. Eventually, numerical and experimental studies dealing with the critical parameters of the metal-insulator transition are discussed.

In Part II the publication presented in Part III are summarized and discussed. Chapters 4 to 6 deal with investigations of Liesegang pattern formation in disordered materials, whereas the aim of Chapters 7 to 9 is to understand the affect of a small magnetic field and of topological-structural disorder for metal-insulator phase transitions.

Chapter 4 is a detailed review of different models on Liesegang pattern formation. In addition, a lattice-gas model to simulate Liesegang patterns is introduced. Different methods to analyze simulation and experimental results are presented. In Chapter 5 the lattice-gas model is used to investigate how disorder and fluctuations effect the pattern formation process. Additionally, effective mean-field descriptions incorporating disorder and fluctuations are derived. In Chapter 6 these results are applied for designing equidistant and more complex patterns. Chapter 7 is the first publication dealing with calculations on localization effects. A prediction for the shift of the metal-insulator transition induced by a small magnetic field is tested in extensive numerical calculation and confirmed. Finally, the topic of Chapters 8 and 9 is the influence of topological disorder on metal-insulator and optical localization transitions. Topological disorder is introduced, using different types of networks and variations of local topological structures in complex networks. At last, the bibliography and the acknowledgments complete this thesis.

Lukas Jahnke
Halle (Saale), May 2009

Part I.

Introduction

1. Structures of disordered systems

Two types of disorder are considered in this thesis which are compositional disorder and structural-topological disorder. In compositionally disordered systems disorder is induced by a non-periodic potential landscape. Dropping the fixed lattice structure creates structural-topological disorder, either by displacements of the atoms, or introducing additional long-range interactions, replacing the lattice by a complex network.

In Section 1.1 examples for both types of disorder in electronic systems are discussed. Additionally, the tight-binding Hamiltonian will be introduced as an example of a disordered electronic system on a lattice. Section 1.2 describes gels and glasses as examples of non-isotropic structures. Complex networks are treated in Section 1.3.

1.1. Electronic materials

In ordered electronic materials the system properties are characterized by long-range translational symmetry. Starting from a perfectly ordered lattice, there are different possibilities to introduce disorder. For compositional disorder the potential landscape is disordered, the simplest model is a random distribution of two different kinds of atoms on a lattice. Further distortions are impurities and vacancies. If vectorial properties (spins) are present, compositional disorder can also be induced by their random orientation.

Disorder is alternatively introduced by relaxation of the lattice structure, called structural-topological disorder. Such types of disorder can be found, e.g., in glassy systems, porous media, or amorphous semiconductors. The simplest model of a structurally disordered system is percolation [29]. A common percolation model is site percolation, where the sites of an ordered lattice are randomly occupied with probability p, as sketched in Figure 1.1. This picture, e.g., corresponds to cases where the occupied sites resemble conducting parts and the unoccupied sites resemble insulating parts of the solid. The connected sites of the lattice are called clusters. For a small occupation concentration p the conducting parts are spatially separated and small (see Figure. 1.1(a)), thus the solid is an insulator. On contrary, for high p a large cluster emerges which reaches from one side of the lattice to the other (see Figure. 1.1(c)). This cluster becomes infinitely large on an infinite lattice, therefore it is called infinite cluster. Transport of particles between the edges is now possible and the solid becomes a metal. An infinite cluster emerges for the first time for the critical occupation concentration, called p_c (see Figure. 1.1(b)). At this critical concentration the system undergoes a geometrical phase transition. For $p < p_c$ the solid is an insulator, whereas for $p > p_c$ a metal. The phase transition is called geometric, because the transition is induced by the geometry of the system, still the description is equivalent to a thermodynamical phase transition. Besides metal-insulator transitions, this percolation model can also describe transport properties in porous media or spreading of diseases and forest fire [29].

Besides site percolation, other variations exist, e.g., percolation in continuum space or bond percolation. The latter is similar to site percolation, with the difference that not the sites are occupied randomly, but the bonds connecting the sites are wired with probability p_b. For all types of percolation different variations of the lattice structure exist, e.g., different dimensions,

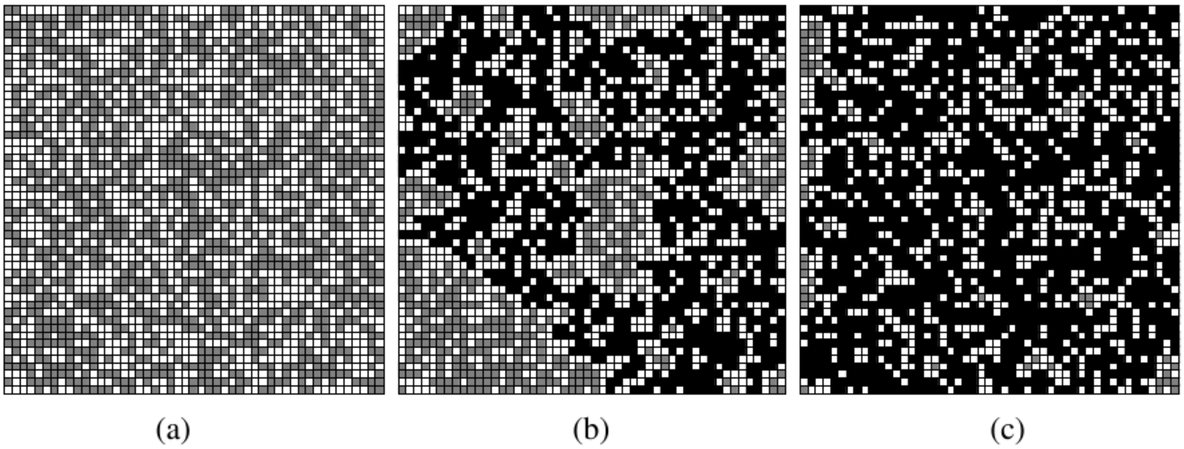

Figure 1.1.: Site percolation on a quadratic lattice: The sites of the finite clusters are colored gray, the infinite cluster is colored black, and the unoccupied sites are white. The occupation concentration is (a) $p = 0.5$, (b) $p = 0.593$, and (c) $p = 0.7$.

triangular and honeycomb lattices. An interesting lattice is the Cayley tree (see Figure. 1.2(a)), because most percolation quantities can be calculated analytically. On a Cayley tree all sites have z neighboring sites connected only with one bond, such that loops are not present. The Cayley tree can be build iteratively, starting from the first site. For the next level, z new bonds and sites are connected from a site of the last level. Site and bond percolation are identical, because in this case the bond is the only connection to the site . Percolation can be defined by connecting the sites of the next level with a connection probability p. If a site is unoccupied (gray circles in Figure. 1.2(b)) the branches growing from this site will all be unoccupied for all levels (white circles in Figure. 1.2(b)). The critical connection probability p_c for the Cayley tree is analytically derived as $p_c = 1/(z-1)$. For higher connection probabilities $p > p_c$, in one iteration on average more than one new branch is attached. Thus the mass of the structure grows exponentially when the size is scaled linearly, as in the case of an infinite dimensional object. For $p < p_c$ the growth of the Cayley tree dies out after a few iteration steps.

The critical occupation probability p_c for a quadratic lattice is $p_c \approx 0.59$ for site percolation and $p_{b,c} \approx 1/2$ for bond percolation. For cubic lattices the corresponding critical occupation probabilities are $p_c \approx 0.31$ and $p_{b,c} \approx 0.25$ (see [29] and references therein). The probability P_∞ for a site to be part of the infinite cluster is zero below p_c and increases above p_c as

$$P_\infty = (p - p_c)^\beta. \tag{1.1}$$

The linear size of the finite clusters, below and above p_c, is characterized by the correlation length ξ. The correlation length is defined as the mean distance between two sites on the same finite cluster and represents the characteristic length scale in percolation. When p approaches p_c, ξ increases,

$$\xi \propto |p - p_c|^{-\nu}, \tag{1.2}$$

with the same critical exponent ν below and above the threshold. While p_c depends explicitly on the type of the lattice, the critical exponents β and ν are universal, depending only on the dimension. The critical exponents for quadratic and cubic lattices are $\beta \approx 5/36$, $\nu \approx 4/3$ and $\beta \approx 0.417$, $\nu \approx 0.875$, respectively. For the Cayley tree they are $\beta = 1$ and $\nu = 1/2$.

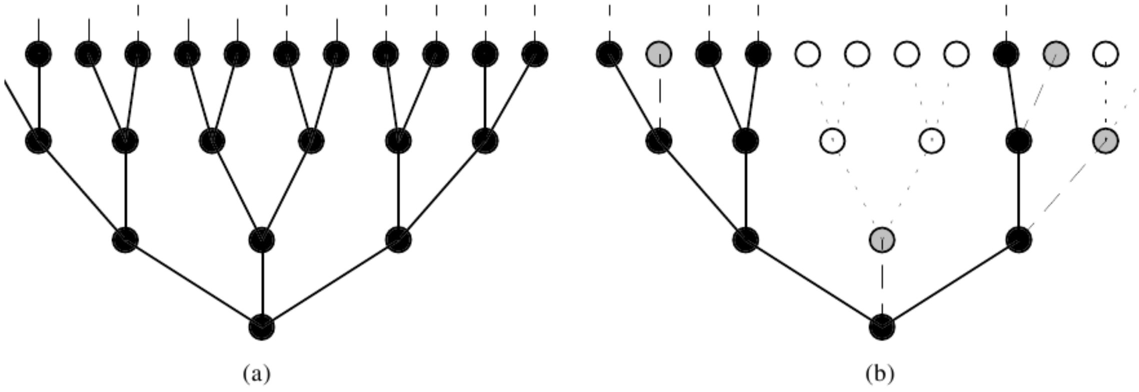

Figure 1.2.: The first three iterations of a Cayley tree with $z = 3$. (a) All sites are occupied. (b) The percolation model. The black sites are occupied, the gray sites are not occupied, the white sites are not connectible to the large cluster.

The infinie cluster at criticality is a stochastic fractal [193]. It is self-similar[1] on all length scales larger than the lattice constant and smaller than the size of the lattice. The fractal properties of the infinite cluster can be measured using non-integer fractal dimensions: non-fractal objects have an integer valued dimension d, such that the mass of the object M scales with the size r as a power-law: $M \propto r^d$. For an infinite cluster the mass scales in average as

$$\langle M(r) \rangle \propto r^{d_f} \tag{1.3}$$

where $d_f \approx 2.5$ for a cubic lattice, $d_f \approx 1.9$ for a quadratic lattice, and $d_f = 4$ for the Cayley tree. Generally, the fractal dimension d_f is smaller than the lattice dimension, because the cluster does not fill the whole space, but d_f is still larger than the dimension of the corresponding hyper plane. The fractal dimension d_f of a percolation cluster only depends on the dimension and not on the concrete lattice structure.

Near p_c, on length scales smaller than ξ, also the finite clusters are self-similar. Above p_c the infinite cluster can be regarded as an homogeneous system, if the length scales are larger than ξ, whereas it is self-similar for smaller ξ, i.e.,

$$M(r) \propto \begin{cases} r^{d_f} & r \ll \xi, \\ r^d & r \gg \xi. \end{cases} \tag{1.4}$$

The structure of disordered systems like percolation clusters can be reasonably described by potential landscapes and hopping probabilities for particles moving on the cluster. An approach, equally suitable for compositional and structural disorder, is a discretized Hamiltonian in a tight-binding approximation (see Section 2.1),

$$H = \sum_i \epsilon_i a_i^\dagger a_i - \sum_{(i,j)} t_{j,i} a_j^\dagger a_i, \tag{1.5}$$

with a_i and $a_i^\dagger$ as the creation and annihilation operators of particles at position $\mathbf{R}_i$, respectively. This approach is suitable for numerical studies of disordered systems, because the discretized

---

[1] Self-similarity is a key property of fractals: If a small piece is cut out of a fractal and magnified isotropically to the size of the original, both the original and the magnification are geometrically equivalent.

Hamiltonian can be mapped to the memory structure of personal computers. The first part of the Hamiltonian (1.5) stands for the on-site disordered potential, whereas the second part describes the nearest neighbor hopping probabilities of the quantum mechanical object.

Disorder is inserted into the Hamiltonian (1.5) by random site energies and/or hopping matrix elements derived from a probability distribution function. An example for compositional disorder is the two-component alloy A_pB_{1-p}, where each site is occupied by an A or B atom with probability p or $1-p$. The probability distribution for the on-site energies is given as

$$P(\epsilon_i) = p\delta\left(\epsilon_i - \epsilon_A\right) + (1-p)\delta(\epsilon_i - \epsilon_B)\,, \tag{1.6}$$

where $\epsilon_{A,B}$ are the site energies of atom A and B, respectively. In the limit $\epsilon_B - \epsilon_A \to \infty$ the wave function of the A subband vanishes identically on the B sites, making them completely inaccessible for the quantum particles. This situation pictures non-interacting electrons, moving on a random ensemble of lattice points, a percolation cluster. Therefore this case is called quantum percolation model [24, 171]. Thus a compositionally disordered system can be transformed into a structurally disordered system. The main difference for both types of disorders on a lattice is that compositional disorder is induced by a potential Landscape, whereas for structural disorder some sites are completely unaccessible.

The Anderson model [9] illustrates another, more complex example. In this model the random on-site energies are derived from a box probability distribution of width W,

$$P(\epsilon_i) = \begin{cases} \frac{1}{W} & -W/2 \le \epsilon \le W/2, \\ 0 & \text{otherwise.} \end{cases} \tag{1.7}$$

or a Gaussion distribution

$$P(\epsilon_i) = \frac{1}{\sqrt{2\pi\sigma^2}} \exp\left(-\frac{\epsilon_i^2}{2\sigma^2}\right), \tag{1.8}$$

with $\sigma^2 = W^2/12$. Results of such investigations are presented in Chapters 7 to 9. An analog model using a Lorentz distribution as the potential distribution

$$P(\epsilon_i) = \frac{W}{\pi(W^2 + \epsilon_i^2)} \tag{1.9}$$

is called the Lloyd model.

An example for off-diagonal disorder is the random phase model where

$$t_{i,j} = t\exp(\imath\phi_{i,j}), \tag{1.10}$$

are the off-diagonal elements with $0 \le \phi_{i,j} \le 2\pi$ random phases. This model describes a spinless electron traveling in a random magnetic field. Interestingly, a magnetic field can be introduced as a special kind of disorder. The effect of a magnetic field are further discussed in Sections 2.1 and 3.2 whereas the results of the effect of small magnetic fluxes are presented in Chapter 7.

1.2. Glasses and gels

Two prominent examples of disordered structures with relevance for reaction-diffusion systems are glasses and gels. Both materials are ideal to investigate reaction-diffusion phenomena, because convection is mostly suppressed.

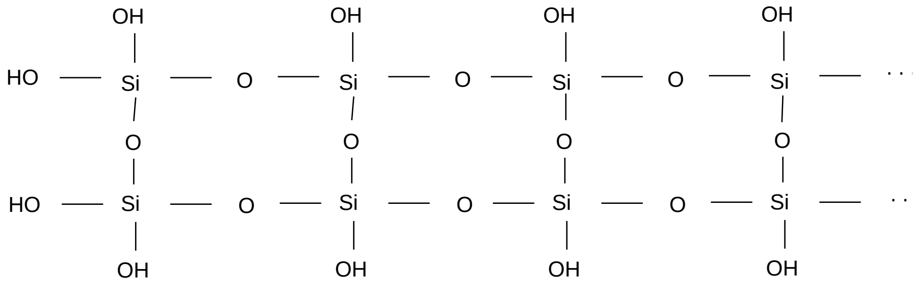

Figure 1.3.: Chemical structure formula for silica hydrogel. Due to the weak $\mathrm{Si}-\mathrm{O}$ bonding this structure does not correspond to the geometric structure of the gel. In contrast, rings of larger sizes, broken linkages, and dynamical changes of linkages occur.

A gel, as a material, can not be defined rigorously. It is usually a two component system of solid and liquid nature. Typical types of gels are silica gels, agars, gelatins and soft soaps. Gels are created from suspensions or solutions. The molecules of the first, solid component are three dimensionally cross linked. The second component, usually water, penetrates this network as a continuous phase. Therefore, a gel can be compared with a loosely interlinked polymer. Linkages are formed by cooling, by chemical reactions, or by inserting additives.

In the following silica hydrogel is examined as an example for a gelic structure. This gel is a solution of sodium metasilicate. Monosilicic acid is produced in accordance with the dynamic equilibrium

$$\mathrm{Na_2SiO_3} + 3\mathrm{H_2O} \leftrightharpoons \mathrm{H_4SiO_4} + 2\mathrm{NaOH}, \tag{1.11}$$

and polymerizes with liberation of water. This reaction proceeds until a three-dimensional network of $\mathrm{Si}-\mathrm{O}$ links is established as shown in Figure 1.3. The geometrical structure is not rectangular, as the chemical structure formula suggests. Rings of larger sizes form, linkages break, and pores emerge, even large enough for ions or small particles to diffuse through the gel.

Glasses have an even longer history than gels, both in art craft and in technology. Glazed stones found in Egyptian tombs can be dated back to 12,000 B.C. In the middle ages glass technology was brought to perfection as can be seen in colorful church windows all around Europe. Today, glasses are common and essential in technology. Most of the commercially used glasses are compositions of oxides, which are silica based. In the past decades interest in non-oxide glasses has emerged. Although scientifically interesting, these are not further considered in this thesis.

Important types of oxide glasses are vitreous silica glasses, inexpensive soda-lime glasses, or borosilicate glasses. Vitreous silica glasses are highly pure $\mathrm{SiO_2}$ composites with the largest refractory index in commercially used glasses. In addition to their refractoriness, they have a high chemical resistance to corrosion, a very low electrical conductivity, a near-zero coefficient of thermal expansion, and good UV transparency. Soda-lime glasses can be produced abundantly by large-scale continuous melting of inexpensive materials such as soda, limestones, and sand. They have good chemical durability, high electrical resistivity, and good spectral transmission in the visible region. Because of the relative high coefficient of thermal expansion, they are prone to thermal shock failure. For borosilicate glasses small amounts of alkali are added to silica and boron oxides. A low thermal expansion coefficient and good resistance to chemical attack characterizes this glass family.

Similar to gels, it is not trivial to define glasses. The peculiarity of glasses is their melting temperature. Surprisingly, they do not have a sharp, well-defined melting point. Glasses are essentially isotropic in the absence of applied forces and internal stress. Therefore, glasses re-

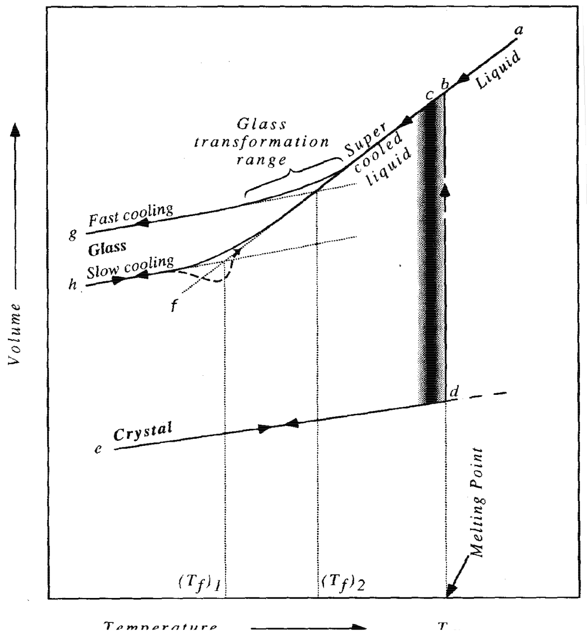

Figure 1.4.: The volume-temperature digram for a glass-forming liquid in comparison to a crystal solid-liquid phase transition. Figure taken from [206]

semble a solid liquid. Varshneya [206] tries to define glasses using different phrases as *solid with liquid like structure*, *a non-crystalline solid*, or generally as *amorphous solid*. A common definition would be an *amorphous solid* which undergoes a *glass transition*.

An example of a glass transition compared with a crystal solid-liquid phase transition is given in Figure 1.4. When a liquid is cooled, the volume reduces along the path *abc*. The melting point corresponds to the temperature T_m, assumed to be at point *b*. For crystals, this point is defined as the temperature where the crystallized solid and the liquid have the same Gibbs free energy and the emerging crystal is in equilibrium with the remaining liquid. Crystallization depends on fast nucleation and growth, therefore the transition point is smeared, represented by the gray shadowed vertical line. A fast volume shrinkage accompanies the crystallization process and a further volume reduction takes place on a much slower pace afterwards. If crystallization does not occur below T_m, e.g., fast cooling (quenching), the liquid reaches a supercooled state, corresponding to path *bcf*. In contrast to crystallization, no discontinuities are observed in the volume shrinkage. By cooling the volume shrinks further, due to the lower kinetic energy of the sample, and the viscosity of the supercooled liquid rapidly increases. If the temperature is low enough, the mobility of the molecules is too small to rearrange into a crystalline structure characteristic for this temperature. As a result, the state line departs smoothly from path *bcf* and reaches a near straight line mostly parallel to path *de*. The final volume depends on the speed of cooling, as indicated by point *g* and *h*. The material in the nearly straight low-temperature part of the curve behaves essentially as a solid and is in a glassy state. The region from departing the supercooled state path to the seemingly rigid condition is called the glass transition region or glass transformation range. This transition does not take place at one critical temperature, but is smeared throughout the entire range. The intersection between the interpolated glass path and the supercooled path is termed fictive temperature (T_f). At this temperature, the structure of the supercooled liquid is frozen into the glass.

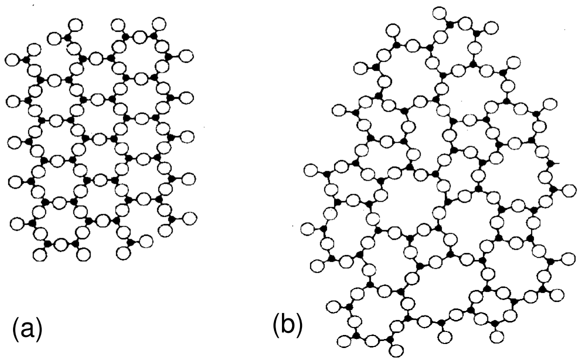

Figure 1.5.: Atomic structural representation of a hypothetical $A-O$ composite, where A could be, e.g., silicon. (a) A_2O_3 crystalline structure. (b) A_2O_3 glass structure. Figure taken form [206]

The structural differences of crystalline and glass structure are shown for a hypothetical composite in Figure 1.5 where (a) corresponds to a hypothetical crystalline and (b) to glass structure. On medium scale, the glassy system in (b) is disordered and not isotropic. Similar to gels, large rings and broken linkages occur, in contrary bonds are much stronger. Through these pores ions or particles diffuse but convection is impossible.

In contrast to the last section, where disorder plays an important role in the modeling of phase transitions, the effect of disorder in gels and glasses will be integrated into the transport, nucleation and growth process. In mean-field models, fluctuations around the mean diffusion speed is neglected. Such fluctuations are included in lattice-gas models introduced in Section 4.4. Furthermore, disorder in gels and glasses has a great influence on growth and nucleation processes, they are included in the lattice-gas simulation and cause fluctuations. The fluctuations are important in the description of Liesegang patterns, because they enhance or even initiate the pattern formation (Chapter 5).

1.3. Complex networks

Only recently, networks have attained interest in research. This is somehow surprising, because networks can be found in a variety of dynamical systems, as protein folding, food webs, social contacts, phone calls, collaborational networks in science and business, the world wide web (WWW), and the Internet. In a network, one typically speaks of nodes which are linked or connected through edges. For example, in social networks the nodes are humans and the edges are different types of social connections. The number of edges a node participates in, is its degree k.

Although networks can be found in very different applications, it is possible to group different networks using only few characteristic properties. A general characterization is the distribution of degrees $P(k)$. In an Erdös-Rényi graph where N nodes are connected randomly with a probability p the degree distribution is given by a Poisson distribution which peaks at $k_0 = \langle k \rangle$ [4, 67]. For a second important class of networks, so called scale-free networks, one finds $P(k) \propto k^{-\lambda}$ [104] with exponent $\lambda > 2$. These are called scale-free, because their second moment diverges, hence, no intrinsic scale can be defined. Scale-free networks can be found in natural, sociological and technological networks.

An additional network property is the average path length l. The path length $l_{i,j}$ between nodes n_i and n_j is defined as the number of nodes along the shortest path between them. Another way to define the topological size of networks is the diameter d which is the maximal distance between any pair of nodes. For Erdös-Rényi graphs the average path length l and the diameter d can be calculated analytically and are given by the logarithm of its size, $l \propto d \propto \ln N$ [4]. The average path length and the diameter of scale-free networks depend on the exponent λ. For $\lambda > 3$ one finds the same results as in the Erdös-Rényi graph case whereas for $\lambda < 3$, $d \propto \ln \ln N$ [48], and for $\lambda = 3$, $d \propto \ln N / \ln \ln N$ [26]. Since the average distance of the nodes is very small, networks are revered to as small-world objects. Moreover, scale-free networks with $\lambda < 3$ are referred to as ultra small-world objects.

Another property occurring in real networks is clustering. Especially social networks tend to contain cliques. These are circles of friends or acquaintances where every member knows every other member. Such behavior can be quantified by the clustering coefficient C. If the neighbors of a node n_i with k_i edges is grouped in a clique where everybody is connected with each other, this clique has a total of $k_i(k_i - 1)/2$ edges. The clustering coefficient can than be defined as the ratio of the actual number of edges between these nodes, T_i, and the maximum value of possible edges [212],

$$C_i = \frac{2T_i}{k_i(k_i - 1)}. \tag{1.12}$$

This equation can also be derived by calculating the numbers of triangles, T_i, passing through vertex i.

Although clustering is by definition a local topological quantity, it is possible to define a global clustering coefficient C by averaging over C_i. Such global approach can not take into account special properties of a network. For instance degree-degree correlations, also known as assortativity, can lead to equal C, although the topological structures of either network are fundamentally different [157]. Therefore, a practical ansatz is a degree dependent clustering coefficient [207, 174],

$$\bar{C}(k) = \frac{1}{N_k} \sum_{i \in \Gamma(k)} C_i, \tag{1.13}$$

where N_k is the number of vertices of degree k and $\Gamma(k)$ is the set of such vertices. There are limitations on the actual form of Equation (1.13) for scale-free networks which can be approximated by [174]

$$\bar{C}(k) = C_0(k - 1)^{-\alpha}. \tag{1.14}$$

The exponent $\alpha \in [0, 1]$ depends on the assortativity of the network; for low assortativity $\alpha \to 1$ and for high assortativity $\alpha \to 0$. Applications and further discussion of clustering will be given in Section 9.3.

Examples of networks and their properties are shown in Table 1.1. All presented real world networks are small-world objects with average path length around three. This average path length is similar to an equivalent random network. In contrary, the measured clustering coefficients are much higher than those of an equivalent random network, where nearly no cliques emerge. This occurs due to equivalent probabilities for a connection of nearest neighbors and two random nodes [4],

$$C_{\text{rand}} = p = \frac{\langle k \rangle}{N}, \tag{1.15}$$

reducing to zero for large N. Then again, Table 1.1 suggests that the clustering coefficient is independent of the size. This shows similarity to a lattice, where clustering is also size independent, depending only on the coordination number. Contrariwise, lattices do not have short path

Table 1.1.: Exemplary real world networks and their characteristic properties: network size N, average degree $\langle k \rangle$, average path length l, average path length of an equivalent random network l_{rand}, clustering coefficient C and clustering coefficient of an equivalent random network C_{rand}. Data taken from [4] and references therein.

Network	N	$\langle k \rangle$	l	l_{rand}	C	C_{rand}
WWW, site level, undir.	153,127	35.21	3.1	3.35	0.1078	0.00023
Internet, domain level	3015-6209	3.52-4.11	3.7-3.76	6.36-6.18	0.18-0.3	0.001
Movie actor	225,226	61	3.65	2.99	0.79	0.00027
SPIRES co-authorship	56,627	173	4.0	2.12	0.726	0.003
E. coli, reaction graph	315	28.3	2.62	1.98	0.59	0.09
Silwood Park food web	154	4.75	3.40	3.23	0.15	0.03
Words, co-occurrence	460,902	70.13	2.67	3.03	0.437	0.0001
Power grid	4941	2.67	18.7	12.4	0.08	0.005

lengths. For a d-dimensional hypercubic lattice the average node-node distance scales as $N^{1/d}$, i.e., it increases much faster with N compared with the logarithmic increase observed for random and real world networks.

The simplest way to create networks with high clustering but small l was proposed by Watts and Strogatz in 1998 [212]. In this model one starts with an ordered ring lattice where each node n_i is connected to the K nodes closest to it (Figure. 1.6(a)). For this kind of lattice, the clustering coefficient is

$$C = \frac{3(K-2)}{4(K-1)}, \tag{1.16}$$

converging to $3/4$ in the limit of large K. As a second step, the edges will be rewired with a probability p_r without allowing self-connections and duplicate edges. Therefore, $p_r NK/2$ long-range edges are introduced, connecting to other neighborhoods. Using this model, it is possible to numerically calculate the dependence of clustering $C(p_r)$ and average path length $l(p_r)$ on the rewiring probability p_r. Figure 1.6(b) shows, that the transition to a small-world object is rather fast, with nearly constant clustering coefficient. As a result, the small-world phenomena is almost undetectable at the local level. Like in real world networks, a coexistence of small-world characteristics and high clustering is possible.

In the pioneering work of Barabási and Albert [16] it is argued that real networks have two generic mechanisms missing in random graphs. Firstly, real networks grow from a small number of nodes by including new nodes and edges, e.g. the WWW is growing exponentially by new links and additional pages, and co-authorship connections in scientific publications are growing steadily by new publications. Secondly, nodes are not connected independent of their degree, i.e., nodes with high degree are more probable to be linked with new nodes. For example well known web pages, having large amounts of links, will be rather linked than unknown ones. Just as well, papers with large amount of citations are rather cited again. This phenomena is known as preferential attachment in network science. Both ingredients, growth and preferential attachment, lead to a model which dynamically reproduces scale-free degree distribution [16].

For practical reasons in investigations on scale-free networks, as in Chapters 8 and 9, the networks are not grown dynamically. Algorithms are used, generating networks with predefined degree distributions. An algorithm which produces networks with predefined degree distribution and clustering is presented in [174].

Similar to lattices, percolation can be defined on networks. The occupation probability p is

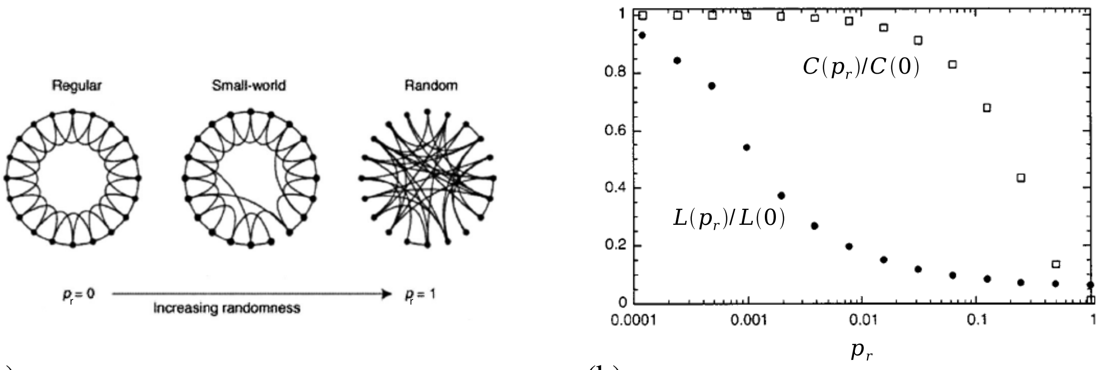

(a) (b)

Figure 1.6.: (a) Evolution of Watts-Strogatz model which interpolates between a regular ring lattice and a random network, without altering the number of nodes or edges. Left one begins with $N = 20$ nodes which are fully connected to the four nearest neighbors. The edges are rewired with a probability p_r. For higher p_r the network becomes more and more disordered until for $p_r = 1$ it is totally randomly connected. (b) Average path length $l(p_r)$ and clustering coefficient $C(p_r)$ of a Watts-Strogatz model dependent on the rewiring probability p_r. The scales for p_r are logarithmic to resolve the fast drop in $l(p_r)$. Figures after [212].

equivalent to the probability to connect an edge or introduce a node. The critical occupation probability p_c of a network depends on its degree distribution. A randomly connected network with arbitrary degree distribution has an infinite cluster if [149, 47]

$$\frac{\langle k^2 \rangle}{\langle k \rangle} > 2. \tag{1.17}$$

Random removal of nodes and edges with probability $q = 1 - p$ changes the degree distribution, reducing $\langle k^2 \rangle / \langle k \rangle$. The critical probability p_c is reached when $\langle k^2 \rangle / \langle k \rangle = 2$. Scale-free networks resemble an interesting case. It is nearly impossible to break the network, i.e., $p_c > 0.99$, for exponents $2 < \lambda < 3$ [46, 47].

Equation (1.17) is only true for uncorrelated networks with zero clustering. The influence of degree-degree correlations on the stability of networks is not much investigated. For uncorrelated networks with clustering coefficient C_0, defined in Equation (1.14), an infinite cluster exists if [177]

$$\frac{\langle k^2 \rangle}{\langle k \rangle} > 2 + C_0. \tag{1.18}$$

Therefore, clustering shifts the percolation threshold, such that the network breaks for lower p_c. Surprisingly, it is also possible to break the network for $2 < \langle k^2 \rangle / \langle k \rangle < 3$ by a mere change of clustering without tampering with the degree distribution, i.e., without removing nodes or bonds.

2. Dynamics of disordered systems

The aim of physics is not only to study static properties of matter but also dynamical quantities as transport and reaction. The transport properties of electrons in disordered systems are investigated in Section 2.1 in the context of the tight-binding model. Similarities between quantum and classical waves are the topic of Section 2.2. In Section 2.3 reaction-diffusion dynamics will be introduced.

2.1. Electronic dynamics

The dynamics shown in this chapter concern the wave functions and energy spectra of non-interacting quantum mechanical objects. The Hamiltonian describing a non-interacting electron moving in a potential V of N equal atoms, sitting at lattice points $\mathbf{R}_j$ with lattice constant $a = |\mathbf{R}_j - \mathbf{R}_{j+1}|$, is [52, 114]

$$H(\mathbf{r}) = \frac{p^2}{2m} + \sum_{j=1}^{N} V(\mathbf{r} - \mathbf{R}_j). \tag{2.1}$$

Obviously, the potential $V(\mathbf{r})$ is invariant under a translation $\mathbf{R} = a\mathbf{e}_r$,

$$V(\mathbf{r}) = V(\mathbf{r} + \mathbf{R}), \tag{2.2}$$

with $\mathbf{e}_r = (\mathbf{R}_j - \mathbf{R}_{j+1})/a$ an identity vector parallel to one of the symmetry axises, e.g. for a cubic lattice $\mathbf{e}_r \in \{\mathbf{e}_x, \mathbf{e}_y, \mathbf{e}_z\}$. More electrons are added by summation over several one-particle Hamiltonians (2.1). For example for M electrons the full Hamiltonian is $\tilde{H} = \sum_{i=1}^{M} H_i$ with H_i as Equation (2.1), but $\mathbf{r} \to \mathbf{r}_i$ and $p \to p_i$.

The electronic wave function $\Psi(\mathbf{r})$ and the corresponding energies E are solutions of the continuous time independent Schrödinger equation

$$H\Psi(\mathbf{r}) = E\Psi(\mathbf{r}). \tag{2.3}$$

In the one-particle picture, the wave function describing several electrons is the antisymmetric product of the single one-particle eigenfunctions $\Psi(\mathbf{r})$. Due to the translational symmetry of the potential the Hamiltonian permutes with the translational operator, having the same eigenfunction Ψ. This leads to the solution

$$\Psi(\mathbf{r} + \mathbf{R}) = \exp(\imath\mathbf{k}\mathbf{R})\Psi(\mathbf{r}). \tag{2.4}$$

The periodicities of eigenfunction and lattice are equal up to a phase shift and can be constructed from an elementary function $u_{\mathbf{k}}(\mathbf{r}) = u_{\mathbf{k}}(\mathbf{r} + \mathbf{R})$, known as Bloch factors,

$$\Psi_{\mathbf{k}}(\mathbf{r}) \propto \exp(\imath\mathbf{k}\mathbf{r})u_{\mathbf{k}}(\mathbf{r}), \tag{2.5}$$

with quantized $\mathbf{k}$ vectors. Therefore, the problem is reducible to solutions of the Bloch factors. Equation (2.5) is known as the Bloch theorem.

Although the Bloch theorem is an important description of band structures in solid state physics, it is not suitable to describe disordered media. For disordered solids the solution of a unit cell is not sufficient due to lacking translational symmetry. Consequently, different approaches have been developed; exemplary a discussion of the tight-binding model follows. In this model the starting point is not a free electron in a periodic potential, but a tightly bound electron.

The Hamiltonian (2.1) can be split in two parts. First the Hamiltonian at position $\mathbf{R}$ of the tightly bound electron,

$$\hat{H}_{\mathbf{R}} = \frac{\mathbf{p}^2}{2m} + V(\mathbf{r} - \mathbf{R}), \tag{2.6}$$

and second, an effective potential of all the other atoms

$$\Delta V_{\mathbf{R}}(\mathbf{r}) = \sum_{\mathbf{R}' \neq \mathbf{R}} V(\mathbf{r} - \mathbf{R}'). \tag{2.7}$$

The idea of the tight-binding model is to construct Bloch functions from the localized states around the atoms. An orthonormal basis of localized states, the Wannier state, is defined as

$$w_n(\mathbf{r} - \mathbf{R}) = \frac{1}{\sqrt{N}} \sum_{\mathbf{k}} \exp(-\imath \mathbf{k}\mathbf{R}) \Psi_{n\mathbf{k}}(\mathbf{r}), \tag{2.8}$$

with n the quantum numbers of the solutions of the atomic Hamiltonian and $\Psi_{n\mathbf{k}}(\mathbf{r})$ Bloch functions. Using Equation (2.8) it is possible to calculate the dispersion relation

$$E_n(\mathbf{k}) = \epsilon_n + \sum_{\mathbf{R} \neq 0} \exp(-\imath \mathbf{k}\mathbf{R}) \Lambda(\mathbf{R}), \tag{2.9}$$

with ϵ_n the energy potential of the nth state and $\Lambda(\mathbf{R})$ corresponding to the interaction of the other atomic potentials. Both, ϵ_n and Λ, depend on the Wannier function (2.8) which itself depends on the Bloch function, the unknown solution of the problem. Clearly, Equation (2.9) is only solvable self consistently applying a linear combination of the periodic wave functions (2.5) as zeroth order approximation of the Wannier function. This ansatz is known as LCAO (Linear Combination of Atomic Orbits) method.

For the purpose of this work it is sufficient to take the matrix elements as parameters in the Wannier basis, leading to an Hamiltonian

$$H = \sum_{n,i} \epsilon_{n,i}\, a^{\dagger}_{n,i}\, a_{n,i} + \sum_{n,i \neq j} t_{n,i,j}\, a^{\dagger}_{n,i}\, a_{n,j}, \tag{2.10}$$

with $a^{\dagger}_{n,i}$ ($a_{n,i}$) a creation (annihilation) operator for a Wannier state with quantum number n at position $\mathbf{R}_i$. For example the Wannier function in spatial representation is

$$w_n(\mathbf{r} - \mathbf{R}_i) = \langle \mathbf{r} | a^{\dagger}_{n,i} | 0 \rangle. \tag{2.11}$$

For only one state per site Equation (2.10) reduces to the form introduced in Equation (1.5).

Disorder can be introduced into Equation (2.10) by parametrization of the potential landscape $\epsilon_{n,i}$ (corresponding diagonal disorder) or the hopping-matrix elements $t_{n,i,j}$ (the off-diagonal disorder). Next to diagonal disorder as the main topic of this work, off-diagonal disorder is introduced in form of a magnetic field in Chapter 7.

A common parametrization of disorder, used for the Anderson model [9], is Equation (1.7). The width W of distribution (1.7) quantifies the strength of disorder. For vanishing width the ordered lattice is recovered. In this case the energy eigenvalues form energy bands of finite width and the eigenfunctions correspond to periodic Bloch functions spreading throughout the entire system. Electrons in such extended states are highly mobile and contribute to charge transport. For high disorder (large W) strong fluctuations of the potential energy lead to backscattering and interference effects, and the wave function localizes. It decays exponentially in space, therefore electrons are bound at the impurities and can not contribute to transport.

Starting from an ordered lattice the density of states broadens for higher disorder and localized states appear near the band edges, separated from the extended states in the band center at a critical energy $\pm E_c$, called mobility edges [119]. At a critical disorder W_c the mobility edges merge at the band center. At this point a quantum phase transition occurs, known as the metal-insulator transition (MIT). For a one dimensional system $W_c = 0$ can be calculated analytically [119]. For higher dimensions no analytical approaches are feasible and W_c needs to be extracted numerically. As a result, properties of two dimensional systems are discussed controversially, yet it is a general believe that no extended state exists. In three dimensional (3d) systems a phase transition from extended to localized states is observed for $W_c \approx 16.5$. Recent values are listed and discussed in Section 3.2.

In quantum percolation the disorder is induced by the geometrical structure and measured by the connection or occupation probability p (see Section 1.1). For $p < p_c$ all clusters are finite, therefore the eigenfunctions are always localized. The same is true at p_c due to the fractal structure of the cluster, resembling a highly disordered system. For $p > p_c$ the infinite cluster becomes more and more dense, until it is an ordered lattice for $p = 1$ with extended plain waves as eigenfunctions of the tight-binding Hamiltonian. Therefore, a critical connection or occupation probability p_q has to exist, with $p_c < p_q \leq 1$, where for the first time extended states are observed in the eigenvalue spectrum $p_q = \min_E p_q(E)$.

A magnetic field shifts the critical disorder [112]. This is not surprising, since the field can be regarded as a special kind of off-diagonal disorder (see Equation 1.10). In quantum mechanics a magnetic field is introduced by substituting $\mathbf{p} \rightarrow \mathbf{p} - e\mathbf{A}$ [89] in the Schrödinger Hamiltonian (2.1), with e the elementary electrical charge. In classical electrodynamics the vector potential was introduced as a convenient mathematical aid, but all fundamental equations are expressible in terms of fields. This is no longer true in quantum mechanics, where the vector potential is necessary to introduce the magnetic field in the canonical formalism. For quantum mechanical objects the vector potential is relevant, even though the magnetic field $\mathbf{B} = \nabla \times \mathbf{A} = 0$. For example, in the case shown in Figure 2.1 electrons move through a field free zone, but interference effects are detected at the screen, induced by a non-zero vector potential $\mathbf{A}$ which leads to a phase shift of the wave function [3].

The vector potential is gauge invariant, therefore, Landau gauge is chosen, $\mathbf{A} = B(0, x, 0)$, to simplify the problem. The hopping matrix elements from the tight-binding Hamiltonian (2.10) with $\mathbf{R}_j = \mathbf{R}_i + \mathbf{\Delta}_R$ and $\mathbf{\Delta}_R = \pm \mathbf{e}_y$ will read $t_{i,j} = t \exp(\pm 2\pi\imath\phi_{i,j} m)$ where $m = \mathbf{R}_i \cdot \mathbf{e}_x$, and $\phi_{i,j} = \varphi_{i,j}/\varphi_0$ is the ratio of flux $\varphi_{i,j} = a^2 B_{i,j}$ through a lattice cell with size a^2 to one flux quantum $\varphi_0 = h/e$. For $\mathbf{\Delta}_R \in \{\pm\mathbf{e}_x, \pm\mathbf{e}_z\}$ the non-diagonal matrix elements are $t_{i,j} = t$. The results for $\phi_{i,j} = \delta$ and $\phi_{i,j} = 1/4 + \delta$ are invariant under the shift $\delta \rightarrow -\delta$. Thus the range $\phi_{i,j} = 0$ to $\phi_{i,j} = 1/4$ represents the full flux spectrum from the flux free case to the largest possible flux.

A constant magnetic field is described by a constant magnetic flux $\phi_{i,j} = \phi$ through each plaquete. If $\phi_{i,j}$ is a random number, derived form an interval $[-\phi/2, \phi/2]$ with a uniform probability density $p(\phi_{i,j}) = 1/\phi$, a spatially random magnetic flux is modeled. The relation between flux per plaquete ϕ and magnetic field $\mathbf{B}$ depends on the lattice constant a, $B = \phi h/a^2 e$. Therefore, if the lattice spacing is a real crystal on the order of, e.g., several Å, a value of $\phi = 1/4$ implies

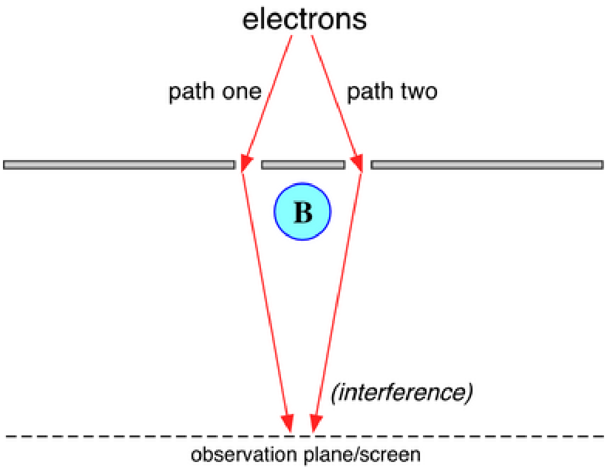

Figure 2.1.: Schematic experiment to demonstrate the interference effect of a time-independent vector potential. The gray circle is a solenoid, the magnetic field $\mathbf{B}$ is confined within. The vector potential, $\mathbf{A}$, is different from zero everywhere outside the solenoid, because the total flux through every circuit containing the origin is equal to a constant $\varphi = \int \mathbf{A} d\mathbf{x}$. The phase difference ΔS of the two electron beams at the screen will be $\Delta S \propto \int \mathbf{A} d\mathbf{x} \propto \varphi$ [3]. Hence, interference between two electron beams is induced by the vector potential $\mathbf{A}$. No magnetic force is applied to the electrons.

an enormous magnetic field at the order of a several thousand Tesla. An alternative ansatz would be to introduce a size depending flux $t_{i,j} = t\exp(-2\pi\imath\phi_{AB}a/L)$, known as the Aharonov-Bohm flux, with L as the size of the system. Recent values of critical disorder W_c for different fluxes ϕ are listed and discussed in Section 3.2.

2.2. Classical wave dynamics

In a disordered system electrons scatter at impurities, and localization of the wave function occurs due to backscattering and interference effects. Surprisingly, the Schrödinger equation (2.3) has similarities to the scalar wave equation,

$$\frac{\partial^2}{\partial t^2}\Psi - v^2\nabla^2\Psi = 0, \tag{2.12}$$

with v the speed of the wave inside a uniform medium. The scalar wave equation differs from electromagnetic and elastic wave equations, because classical waves have vector character, i.e. different polarization. Electromagnetic waves have two polarized states transverse to the wave vector $\mathbf{k}$, and elastic waves have a further longitudinal polarization parallel to $\mathbf{k}$. In uniform and isotropic media it is possible to decouple polarized states and describe each, using Equation (2.12). In disordered media decoupling is an approximation, because scattering leads to interconversion of different polarized states. Nonetheless Equation (2.12) is sufficient to describe localization effects.

Inserting the wave amplitude function

$$\Psi(\mathbf{r}, t) = \exp[-\imath(\omega t - \mathbf{k}\cdot\mathbf{r})] \tag{2.13}$$

of a plane wave with frequency ω into Equation (2.12) leads to an alternative form of the classical wave equation

$$\nabla^2\Psi + \kappa^2\Psi = 0 \tag{2.14}$$

with

$$\kappa^2 = \frac{\omega^2}{v^2}. \tag{2.15}$$

Equation (2.14) is equivalent to the Schrödinger equation (2.3) with

$$\kappa^2 = \frac{2m(E-V)}{\hbar^2}. \tag{2.16}$$

For the quantum case κ^2 is only positive for $E > V$, whereas it is always positive for classical waves. Spatial dependencies are introduced in the quantum mechanical case by a spatially varying potential $V(\mathbf{r}) = V + \delta V(\mathbf{r})$ or for classical waves by fluctuating dielectric constants $\epsilon(\mathbf{r}) = 1 + \delta(\mathbf{r})$ with $v^2 = c^2/\epsilon(\mathbf{r})$. The quantity κ^2 is separable in constant κ_0^2 and spatially varying $\sigma(\mathbf{r})$ values

$$\kappa^2 = \kappa_0^2 - \sigma(\mathbf{r}), \tag{2.17}$$

with

$$\kappa_0^2 = \frac{2m}{\hbar^2}(E-V) \quad \text{and} \quad \kappa_0^2 = \frac{\omega^2}{c^2}, \tag{2.18}$$

for quantum and classical waves, respectively. Both are, up to a constant term, equivalent. While κ_0^2 is linear in energy for the quantum case, it is quadratic in the classical case due to the different order of the time derivative in the fundamental equations of motion.

The terms depending on $\mathbf{r}$ are

$$\sigma(\mathbf{r}) = \frac{2m\delta V(\mathbf{r})}{\hbar^2} \quad \text{and} \quad \sigma(\mathbf{r}) = -\delta\epsilon(\mathbf{r})\frac{\omega^2}{c^2}, \tag{2.19}$$

for the quantum coefficient and classical coefficient, respectively. A striking difference between quantum mechanical and classical case is the frequency dependence of the latter. The consequence is a frequency dependent disorder strength, where $\sigma(\mathbf{r})$ vanishes for $\omega \to 0$ in the case of classical waves.

Keeping the differences in mind, it is possible to derive a tight-binding model of classical waves on a lattice [180] in analogy to Section 2.1. Diagonal disorder is introduced by a fluctuating dielectric constant, not by a potential as in the case of quantum waves. Therefore, an optical network with fibers and cavities as edges and beam splitters as nodes can be described by the tight-binding Hamiltonian (1.5), where ϵ_i is disorder introduced by beam splitters and $t_{i,j}$ is the phase accumulation of the classical wave by traveling through cavities or fibers. The frequency dependence of ϵ_i can be neglected for monochromatic light. In Chapters 8 and 9 results for localization properties of complex optical networks are presented.

2.3. Reaction and diffusion dynamics

Interference is the dominant effect of quantum objects and classical waves in disordered media, leading to unexpected phenomena, for instance localization of the wave function. The momentum of microscopical particles diffusing in a gel or glass is large enough, such that interference effects can be neglected[1]. Statistical and chemical properties described by diffusion and reaction are the dominant effects.

Diffusion is a typical transport phenomena found in amorphous solids or liquids. In a continuum description the interesting quantity for measuring particle transport is the diffusive flux **j**, describing the number of particles crossing an unit area per second. The measurable static quantity is usually the concentration of particles c, i.e., the number of particles per unit volume. When no external forces are applied they can be equalized,

$$\mathbf{j} = -D\nabla c, \tag{2.20}$$

with D the diffusion constant. Equation (2.20) is called Fick's law.

If the medium is anisotropic, D is a symmetric tensor of rank two. Therefore, three principal diffusivities are needed to describe the total flux of the system. For isotropic media all three principal diffusivities are equal and diffusion is described by one diffusion constant.

In a reaction free case the particle number is conserved and the particle flux gradient is described by a balance equation

$$\frac{\partial c}{\partial t} + \nabla \mathbf{j} = 0. \tag{2.21}$$

Combining Equation (2.21) and Fick's law (2.20) leads to a time dependent equation

$$\frac{\partial c}{\partial t} = \nabla(D\nabla c) \tag{2.22}$$

which reduces to

$$\frac{\partial c}{\partial t} = D\nabla^2 c, \tag{2.23}$$

if the diffusivity D is independent of c. The solution $c(\mathbf{r}, t)$ for all positions $\mathbf{r}$ and times t depends on the boundary conditions of the system and initial conditions $c(\mathbf{r}, t = 0)$.

For example, consider a quasi one dimensional case of particles diffusing into a gel or a glass. The initial condition is $c(x, 0) = 0$ for $x > 0$ and the concentration of the indiffusing particle is held constant at the entering edge, $c(0, t) = c_s$, than the solution of Equation (2.23) is [50]

$$c(x, t) = c_s \operatorname{erfc}\left(\frac{x}{2\sqrt{Dt}}\right), \tag{2.24}$$

where erfc is the complimentary Gaussian error function, defined as

$$\operatorname{erfc} z = 1 - \operatorname{erf} z \quad \text{with} \quad \operatorname{erf} z = \frac{2}{\sqrt{\pi}} \int_0^z \exp\left(-\tau^2\right) d\tau. \tag{2.25}$$

Diffusion in crystalline solids occurs by a series of jumps of individual particles, thus, the diffusivity is describable in terms of physical quantities, the elementary jump processes. On an uniform lattice the probability $P(\mathbf{R}, t|\mathbf{0}, 0)$ to find a particle at lattice point $\mathbf{R}$ at time t when it has been at lattice point $\mathbf{0}$ at time 0 is the master equation

$$\frac{d}{dt} P(\mathbf{R}, t|\mathbf{0}, 0) = -\sum_{\mathbf{R}'} \Lambda_{\mathbf{R}\mathbf{R}'} P(\mathbf{R}', t|\mathbf{0}, 0), \tag{2.26}$$

---

[1] The wave length of a matter wave λ is inversely proportional to its momentum p. This relationship is known as the de Brogli wave length $\lambda = h/p$ of a particle with h Planck's constant. If the de Brogli wave length is smaller than the mean collision length, quantum mechanical effects can be neglected.

with

$$\Lambda_{\mathbf{R}\mathbf{R}'} \sim \begin{cases} z\Gamma & \mathbf{R} = \mathbf{R}' \\ -\Gamma & \mathbf{R}, \mathbf{R}' \text{ nearest neighbours} \\ 0 & \text{otherwise.} \end{cases} \tag{2.27}$$

Γ is the jump rate and z the number of nearest neighbors. Equation (2.26) consists of a gain term, describing particle jumps from nearest neighbors, and a loss term of particles jumping to nearest neighbors.

The solution of Equation (2.26) can be extracted by looking at its Fourier transform

$$P(\mathbf{k}, t) = \sum_{\mathbf{l}} \exp\left(-\imath \mathbf{k} \cdot \mathbf{R}\right) P(\mathbf{R}, t|\mathbf{0}, 0), \tag{2.28}$$

where the Fourier wave vector $\mathbf{k}$ depends on the lattice type. For a hypercubic lattice with $N = L^d$ sites, lattice constant a and periodic boundary conditions, the wave vector reads

$$\mathbf{k} = \frac{2\pi}{La} n. \tag{2.29}$$

The integer n is restricted to values between $-L/2$ and $L/2$, the first Brillouin zone. The solution of the master equation (2.26) in Fourier space is

$$P(\mathbf{k}, t) = P(\mathbf{k}, 0) \exp\left[-\Lambda(\mathbf{k})t\right], \tag{2.30}$$

with $\Lambda(\mathbf{k})$ as the Fourier transform of the transition rate matrix (2.27).

A diffusion constant describing the collective motion of particles can be defined as the proportionality factor of the mean square displacement at time t, with initial position $\mathbf{R} = \mathbf{0}$ at time $t = 0$,

$$\langle R^2 \rangle(t) = -\sum_{l=1}^{d} \frac{\partial^2}{\partial k_l \partial k_l} P(\mathbf{k}, t)|_{\mathbf{k}=0} = \sum_{l=1}^{d} \frac{\partial^2 \Lambda(\mathbf{k})}{\partial k_l \partial k_l}|_{\mathbf{k}=0} t. \tag{2.31}$$

The mean square displacement depends on the geometry of the system. For example, for a hypercubic lattice of dimension d and lattice constant a

$$\langle R^2 \rangle(t) = 2d\Gamma a^2 t, \tag{2.32}$$

and therefore $D = \Gamma a^2$. This is Einstein's description of particle diffusion [66].

Disorder is introduced into the system by an effective transition rate [110]

$$\Gamma_{ij} = \Gamma_0 \exp\left(-\frac{E_{ij}}{k_B T}\right) \tag{2.33}$$

depending on the particles initial i and final site j. E_{ij} are randomly distributed barrier energies $E_{ij} \leq 0$ or traps $E_{ij} \geq 0$. A first order approximation of the microscopical diffusion coefficient for particles in disordered media (as gels and glasses) is the average over all transition rates (2.33) [110]. Therefore, the disordered structure of the medium is parametrized in Chapters 4 and 6 by an effective jump probability.

Reaction-diffusion systems are established by inserting a coupling term R in Equation (2.23), consisting of products of all involved particle concentrations. For example, for two initially separated particles A and B with concentrations $a(x,t)$ and $b(x,t)$, the reaction process of a extinction[2], $A + B \to 0$, is modeled by coupled partial differential equations

$$\begin{aligned} \frac{\partial}{\partial t}a(x,t) &= D_A \frac{\partial^2}{\partial x^2}a(x,t) - R(a(x,t), b(x,t)), && (2.34) \\ \frac{\partial}{\partial t}b(x,t) &= D_B \frac{\partial^2}{\partial x^2}b(x,t) - R(a(x,t), b(x,t)), && (2.35) \end{aligned}$$

with initial states

$$\begin{aligned} a(x, t = 0) &= a_0 \Theta(-x), && (2.36) \\ b(x, t = 0) &= b_0 \Theta(x). && (2.37) \end{aligned}$$

The parameters D_A and D_B are the diffusion constants of A and B particles, respectively. $\Theta(x)$ is the Heaviside step function. The reaction profile $R(x,t)$ can be derived in a mean-field approximation [118] and described in Section 4.3.3.

For high particle concentrations, phase separating processes like nucleation of seeds and their growth are important dynamical properties. A simple model suitable for pattern formations investigated in Chapters 4 to 6 is a supersaturated liquid. In such liquids the nucleation and growth rate depends on the supersaturation

$$s(x,t) = \frac{c(x,t)}{K_{sp}} - 1 \qquad (2.38)$$

with $c(x,t)$ the concentration of a reaction product and K_{sp} its solubility. Using classical nucleation theory it is possible to describe the nucleation rate $n(x,t)$ in dependence on the supersaturation as

$$n(x,t) = g_n s^E(x,t) \exp(-\beta / \ln^2[s(x,t) + 1]), \quad \text{for} \quad s(x,t) > 0, \qquad (2.39)$$

with constants g_n, E, and β [55, 133]. Due to the sensible dependence of the nucleation rate $n(x,t)$ on the supersaturation $s(x,t)$, it is possible to simplify Equation (2.39) by introducing a critical supersaturation threshold $s_{\text{crit,n}}$. If the supersaturation is lower than $s_{\text{crit,n}}$, no particles nucleate whereas for larger supersaturation the nucleation rate is modeled as [133]

$$n(x,t) = g_n \left[s(x,t) - s_{\text{crit,n}}\right]^E . \qquad (2.40)$$

In cases where E is large, a further simplification is to define $s_{\text{crit,n}}$ as a sharp threshold. For $s(x,t) > s_{\text{crit,n}}$ the particles nucleate with a constant nucleation rate n but for $s(x,t) < s_{\text{crit}}$ no particles nucleate. Particle growth can be modeled similarly, either by a linear dependence of the particle growth rate $r(x,t)$ on the supersaturation or also by using a critical threshold $s_{\text{crit,r}}$.

---

[2] This reaction is equivalent to a production of a third particle, C, which does not influence the initial ones: $A+B \to C$

3. Pattern formation and localization

The influence of disorder on pattern formation and localization of quantum and classical waves is the main topic of this work. At a first glance, both themes do not have much in common, also numerical techniques for finding solutions are different. Pattern formation deals with transport and reaction of particles while localization is an interference effect of waves. The conjunctive elements are the aggregation of particles in a finite region and the importance of disorder. In Chapter 5 it is shown that disorder enhances or even initiates pattern formation of Liesegang bands. Similarly, localization is induced by disorder. Different types of disorder are investigated, for example a small magnetic field (Chapter 7) or topological disorder through clustering in complex networks (Chapters 8 and 9), to influence critical parameters.

Due to similarities and diversities of both fields, they serve as good examples how disorder influences formation or appearance of phase separations or transitions. In Section 3.1 pattern formation of Liesegang bands will be introduced as a summary of a detailed review on Liesegang band formation in Chapter 4. Section 3.2 will be devoted to a theoretical background on localization of wave functions and the Anderson model.

3.1. Pattern formation

Patterns can emerge dynamically without external interference. In a self-organized system patterns dissolve when the organizing mechanism is switched off. This can be observed when fish swarms build complex groups when predators are near and dissolve afterwards. In a self-assembled system preexisting complex components evolve to higher ordered systems. This process is reversible and controllable by proper design of the components [214]. Pattern formations are stable aggregations of particles, i.e. permanent for at least a larger time scale, in an irreversible process.

Patterns form in different settings. Examples can be found in geology due to sedimentation or weather processes, on animal skins induced by biological mechanism, or in chemical reactions due to phase separation. They appear in different forms, e.g., as waves, branches and spirals [51, 15, 93]. This thesis concentrates on patterns in reaction-diffusion systems and especially on Liesegang band formation.

Although, Liesegang pattern formation [134] is one of the oldest discoveries of regular pattern structure in reaction-diffusion systems and has a long history of experimental and theoretical investigation, it is not a commonly discussed process. More convenient pattern formations for textbook examples are those describable solely by reaction and diffusion, e.g., Turing patterns [205, 36, 51, 141, 128] or Belousov-Zhabotinsky systems [15, 93]. Liesegang bands additionally require a fast precipitation and growth process.

Liesegang bands emerge in reaction-diffusion processes of two initially separated agents. The first agent, B, is homogeneously distributed in a sample (e.g., glass or gel). The second agent, A, is injected either from one end of the sample or from the center. In the first case bands form (Figure 3.1(a)), in the second case, concentric rings around the center emerge (Figure. 3.1(b)). Liesegang bands were first observed by Raphael Eduard Liesegang in 1896 [134], when he in-

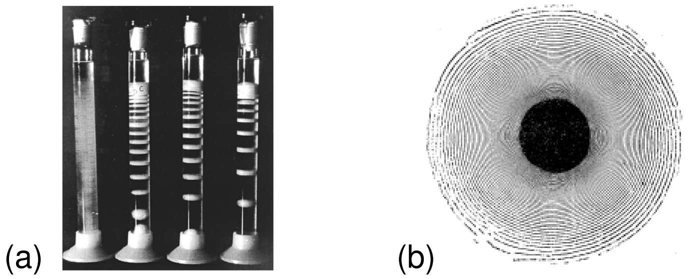

Figure 3.1.: Experimental examples of Liesegang patterns. (a) Agent A is injected from the top of the test tube and diffuses into a gel containing agent B dissolved in the gel, yielding a linear geometry [164]. (b) Same, but agent A is injected from the center [152].

jected a few drops of silver nitrate into a glass plate with a layer of gelatin, impregnated with potassium chromate. In such scenario, series of concentric rings of precipitated silver chromate emerge. The bands or rings form successively where the $(n+1)$th band forms at time $t_{n+1} > t_n$, at position $x_{n+1} > x_n$ and with width $w_{n+1} > w_n$.

A few years later, Morse and Pierce [152] observed diffusional dynamics of the band formation, $x_n \propto \sqrt{t_n}$, in a similar experimental setup as Liesegang [134]. This rule, known as the *time law*, has been validated by a large number of measurements using different types of inner and outer agents such as lead ionide systems [103, 154, 133, 155, 76], magnesium hydroxide systems [154], cobalt hydroxide systems (where band dissolution is observed) [199] and other ionic complexes [75, 76]. The time law is a simple consequence of the diffusional process. The position $x_f(t)$ of the reaction front of the inner and outer agents moves proportional to $\sqrt{t}$ (Section 4.3.3). Because the band formation usually occurs at the reaction front, the time law emerges naturally.

Twenty years later Jablczynski [97] successfully described the spatial positions of bands by a geometrical series. The ratio of two consecutive band positions converges to a constant p, the spacing factor

$$x_{n+1}/x_n \to 1+p \quad \text{for} \quad n \to \infty. \tag{3.1}$$

This observation is known as the *spacing law* and typical empirical values for p reported in literature range from 0.015 [156] to 0.7 [154] with a large variation of different results in macroscopic length scales of millimeters or centimeters [143, 154, 75, 76, 156] and microscopic in the nanometer [148] or micrometer regime [23].

Compared to the time law, it is much harder to find an explanation for the spacing law. In principle, typical model scenarios are reactions of the type

$$A + B \to \cdots C \cdots \to D, \tag{3.2}$$

where most of the differences are found on how the intermediate step, $\cdots C \cdots$, is realized. D is the precipitation product.

The first models had no intermediate reaction [160, 210, 163, 221, 133, 28, 130, 131]. The same is true for the first qualitative description of Liesegang band formation suggested by Ostwald [160] based on supersaturating liquids. He predicted spontaneous precipitation of reaction products as a reason for pattern formation. When the product concentration AB of the inner and outer agent exceeds a critical concentration K_{sp}, nucleation seeds precipitate. These seeds grow at the expense of the reaction product until AB falls bellow a second concentration K_p. This model is known as the *ion product saturation model*.

Early analytical descriptions using the above ansatz [210, 163, 221] could reproduce the spacing law, but in a slightly different form than Equation (3.1),

$$x_{n+1}/x_n = 1 + p. \tag{3.3}$$

In Chapter 4 the contradicting observation (3.1) and prediction (3.3) of the spacing law is reconciled.

Later it became clear that the analysis of Liesegang bands is simplified by introduction of an intermediate particle C [111], because the full process separates into two stages. A well understood reaction-diffusion process $A + B \to C$ [118] succeeded by precipitation $C \to D$.

As introduced in Section 4.3.3, the first process can be solved for special sets of initial and boundary conditions. The pattern forming precipitation can be analyzed separately as nucleation and growth of immobile particles. Therefore, this model is known as the *nucleation and growth model* and is the basis for simulations presented in Chapters 4 to 6. More complicated models are suitable for detailed descriptions of experiments, without revealing more details on the basic Liesegang pattern formation process.

The spacing factor p depends on the initial concentration of the inner and outer agents b_0 and a_0, respectively. This dependence is known as the *Matalon-Packter law*, named after two scientists who found

$$p = F(b_0) + G(b_0)\frac{b_0}{a_0} \tag{3.4}$$

by comparing different types of experiments [143, 161]. F and G are dimensionless monotonously decreasing functions of b_0. It follows that p is linearly dependent on $1/a_0$ for constant b_0.

A first analytical description of the Matalon-Packter law was performed by Antal *et al.* [13]. They derived a more general law, with the Matalon-Packter law as a special case. In case of the nucleation and growth model it states

$$p = \frac{D_C}{D_f}\left[\frac{c_0}{K_{sp}} - 1 - \frac{D_C}{2D_f}\right]^{-1}, \tag{3.5}$$

with c_0 the mean concentration of C particles without precipitation. D_C and D_f are the diffusion coefficients of the intermediate particle C and the reaction front, respectively. As in Ostwalds model, K_{sp} is a nucleation threshold. Nucleation occurs, if the concentration of the intermediate particles $c > K_{sp}$. The Matalon-Packter law can be derived for $b_0 \ll a_0$ (see Section 4.3.3). In [13] the growth of precipitants is neglected. Basically, Equation (3.5) describes patterns of zero width. In Chapter 5 Equation (3.5) is extended to include non-zero widths and fluctuations. This extended Matalon-Packter law is used successfully to control equidistant pattern formation in Chapter 6.

The analytical derivation of Equation (3.5) is described in detail in [13], thus a more qualitative description follows. To understand the band formation in the nucleation and growth model only parameters describing C particles and their nucleation are relevant. Band widths are neglected in Equation (3.5), and hence parameters controlling band growth are not needed. The basic parameters for C particles are their diffusion constant D_C, their mean concentration c_0, and the effective diffusion constant of the reaction zone D_f where these particles are created. The spacing factor p is a dimensionless parameter. As a result, it depends on ratios of these basic parameters, i.e. $p(D_C/D_f, c_0/K_{sp})$. Bands form, if the nucleation threshold is $K_{sp} < c_0$. This is controlled by the denominator of Equation (3.5). For $D_C > D_f$ particles diffuse away from the reaction zone, causing a reduction of the local concentration of C particles at the reaction zone. This has two consequences. First, the denominator needs to be corrected by the term $D_C/2D_f$ and second, the distances between the bands are higher, p is larger, because it takes longer for the concentration c to reach the threshold K_{sp}.

Only recently a fourth law has come into focus, the *width law*. It states that the width w_n of the nth band is proportional to a power-law of the position $w_n \propto x_n^\alpha$ [44, 164, 60, 78, 76]. Alternatively, a linear dependence is proposed and also observed, $w_n = \mu_1 x_n + \mu_2$ [103, 55, 156]. One aim of the results in Chapter 4 is to reconcile both theories.

Theoretically, it is possible to derive the width law using particle conservation [164] leading to

$$w_n = p\frac{c_0}{d_n}x_n, \tag{3.6}$$

with d_n as the density of the nth band (see Section 4.3.3).

Numerical simulations became feasible in the eighties [55, 133] using similar types of reaction-diffusion processes as described in Section 2.3 and nucleation and growth descriptions similar to Equations (2.39) and (2.40). These functions have to be sensible in respect to changes in the supersaturation for Liesegang patterns to emerge [133, 28]. As already suggested in Section 2.3, threshold concentrations for modeling nucleation and growth are therefore reasonable approximations [28, 60, 69, 23].

Besides these reaction-diffusion models, a novel ansatz was introduced in 1999 [164, 12] based on spinodal decomposition (see Section 4.3.5). The first non mean-field model was introduced in 1994 [44, 45]. Instead of solving differential equations the authors succeeded to simulate Liesegang pattern formation in a lattice-gas approach, based on the nucleation and growth model (see Section 4.4). The simulations performed in Chapters 4 to 6 are based on this lattice-gas simulation.

Beyond a detailed theoretical description of Liesegang pattern formation, recent publications concentrate on manipulation of pattern formation to design patterns arbitrarily [21, 142] or achieve equidistant bands [150]. In the first, the pattern forming process is controlled by an external oscillatory electric field [21, 142]. Without electric fields the properties of the reaction front is equivalent to the case discussed in Section 4.3.3. If an electrical field is imposed, the properties of the front change [20]. Interestingly, for a wide range of electrical field intensities neither the locality, nor the diffusive nature of the front is altered. However, the electrical field has an important effect on the production of C particles. The ionic agents are driven toward each other for one polarity and as a result, the concentration of C particles increases in the direction of the front motion. If the opposite polarity is imposed, the concentration of produced C particles reduces until the complete extinction of the reaction. A quasi-periodic current exists for which bands are generated at prescribed band positions. The authors proofed numerically and experimentally the feasibility of this approach. The second publication achieves equidistant banding by an exponential reduction of the nucleation threshold K_{sp} [150]. This is derived by equalizing the nucleation threshold K_{sp} to the concentration of C particles at a desired position. The calculation of K_{sp} is done numerically while the simulation runs. No analytical derivation of the exponential decrease is presented. In Chapter 6 a complimentary ansatz to design patterns is proposed and simulation results of equidistant bands are presented.

3.2. Localization

The main effect of pattern formation is phase separation, meaning that particles group in spatially constraint regions. Interference effects of waves in disordered media lead to a similar effect, where the envelope of the wave function decays exponentially

$$\Psi(r) = f(r)\exp(-r/\lambda), \tag{3.7}$$

with $f(r)$ a randomly varying function and λ the localization length. For finite λ the state is localized, whereas for $\lambda \to \infty$ extended. Disorder initiates a phase transition from extended to localized state. The understanding of phase transitions is a major achievement of modern physics. In the last century it became clear that phase transitions are a general concept mainly dictated by the symmetry of the system. This is also true for the phase transition from extended to localized states, also known as the metal-insulator transition (MIT).

3.2.1. Metal-insulator transition

A practicable method to distinguish an extended from a localized state is the inverse participation number, defined as the second moment of the probability density,

$$P^{-1} = \sum_r |\Psi(r)|^4 \qquad \|\Psi\| = 1. \tag{3.8}$$

It is a measure for the portion of space where the amplitude of the wave function differs markedly from zero. For an extended state with constant amplitude, $|\Psi(r)|^2 = 1/N$, the participation ratio P equals the number of sites N. Thus, $P = N \propto L^d$, with L being the linear size of the system and d its dimension. It diverges in the thermodynamic limit, for $L \to \infty$. For extended states a fractal dimension $d^* \leq d$ [119] is defined as

$$\lim_{L\to\infty} P = L^{d^*}. \tag{3.9}$$

The state is multifractal, if the fractal dimensions are not integer multiples of d^* for higher moments of the probability density [119]. For localized states, P is proportional to the volume where the state has a non-vanishing amplitude. Thus, in the thermodynamic limit $L \to \infty$ the participation ratio P is a constant and the fractal dimensionality vanishes.

An alternative approach, initially considered by Anderson [9], investigates the return probabilities of particles. If a state is extended, the probability of return for large times reaches zero, whereas it remains finite for localized states. Anderson called it *absence of diffusion*.

A general ansatz to describe phase transitions are finite-size scalings of the order parameters. In an early work Thoules [202] states that the conductance G of a system with size $(2L)^d$ only depends on the conductance G_L of the 2^d blocks of size L. Therefore, the dimensionless conductance g, more precisely its arithmetic mean $\langle g\rangle$, only depends on the size of the system and a scaling parameter b,

$$g(bL) = f(g(L), b). \tag{3.10}$$

In a first approximation the logarithmic derivative of g is [1]

$$\frac{d\ln g}{d\ln L} = \beta(\ln g), \tag{3.11}$$

with solution

$$g = g(L/\xi). \tag{3.12}$$

A single length scale ξ is introduced as the constant of integration including all information about scattering rates, energy etc. For very strong disorder, $g \ll 1$, exponential localization is expected with $g \propto \exp(-2L/\lambda)$ and

$$\beta(\ln g) \propto \ln g. \tag{3.13}$$

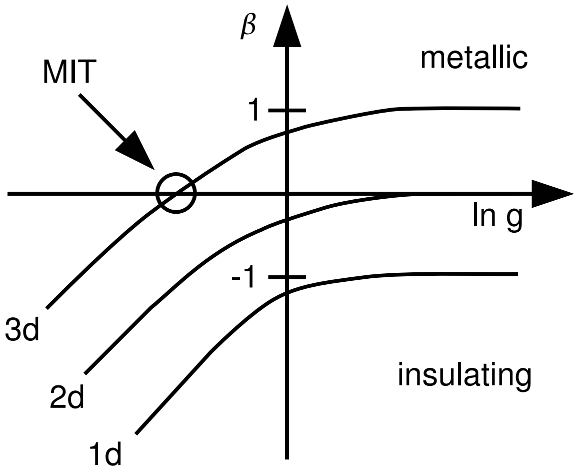

Figure 3.2.: Plot of β against $\ln g$ for one to three dimensional systems and zero temperature. The conductance $g(L)$ increases with increasing L if $\beta > 0$, but it decreases for $\beta < 0$. A crossing at $\beta = 0$ is a critical point corresponding to the metal-insulator transition of the Anderson model and is observed for $d > 2$.

Comparing these expectations with Equation (3.12), the length scale ξ is identified as the localization length λ. If disorder is weak, the system behaves classically with Ohmic conductivity σ, therefore, $g \propto \sigma L^{d-2}$ and

$$\beta(\ln g) \propto d - 2. \tag{3.14}$$

The length scale ξ is related to the conductivity σ as $\xi \propto \sigma^{-1/(d-2)}$ and is interpretable as the correlation length of the system. The β-function, introduced in Equation (3.12), can be sketched (Figure 3.2) by interpolating between Equation (3.13) for negative $\ln g$ and Equation (3.14) for positive $\ln g$. For $\beta < 0$ the conductivity decreases with increasing sample size driving the system towards the localized regime. For $\beta > 0$ the opposite is true, because g rises with L. For $d = 3$ one finds a fix point $\beta = 0$ at which conductivity is independent of system size. This critical point separates the metallic from the insulating region and, thus, corresponds to the metal-insulator transition. For one dimension β is negative, and therefore, the system is always localized. Two dimensions represent the marginal case, it is believed that no crossover exists. Numerical results for the Anderson model on fractal lattices with dimensions $2 < d < 3$ support the assumption that indeed $d = 2$ is the lower critical dimension beyond which a disorder driven metal-insulator transition exists [170].

The conductivity σ of extended states near the critical point W_c is $\sigma \propto |W - W_c|^s$, whereas the localization length $\lambda \propto |W - W_c|^{-\nu}$ [1]. Both exponents can be set into relationship as $s = (d-2)\nu$ [119] and are, therefore, equal in three dimensions. These exponents are understood to be universal in the sense that they are not sensitive to the specific details of the system depending only on general symmetries. Common symmetries are orthogonal, unitary, and symplectic transformations of the Hamiltonian. The first case describes a spin-less electron, the second an electron in a magnetic field, and for the third spin-orbit coupling is considered. Other critical parameters, like the critical disorder W_c, depend on the topology of the system.

In modern approaches the localization length is not derived from the eigenstates Ψ of the dynamic equation (2.10). The most accurate way to calculate the localization length λ for a given energy E without computing the eigenstates explicitly is the transfer-matrix method (TMM)

[119, 88]. TMM plays its strength in the investigation of wave functions of an Anderson model with nearest neighbor interactions. Consequently, TMM is not suitable for non-lattice topologies as complex networks. A geometrically independent method is eigenvalue statistics. Eigenvalue statistics, also known as level statistics, has been established in the late eighties as a method to calculate critical parameters of metal-insulator transitions. Localization properties are deduced from statistical properties of the eigenvalue spectra instead from the eigenfunctions Ψ. The advantage is a reduced numerical effort; the price to pay is the lacking possibility to differentiate the states in an analyzed spectral range.

3.2.2. Level statistics

Level statistics was first used in nuclear physics [218] to understand complex excitation spectra of heavy nuclei. It is not feasible to calculate the energy spectra distribution using elementary quantum physics, but a qualitative description using random matrix theory [62] succeeded.

In the eighties random matrix theory was introduced in solid state physics to understand the chaotic eigenvalue spectra of disordered solid systems [64, 6]. The connections to metal-insulator transitions were realized a few years later and level statistical methods were used for numerical investigations of critical disorder [7, 183, 90, 91]. Review articles concerning random matrix theory and eigenvalue statistics are [145, 83, 146].

In random matrix theory [145] the objects of investigation are 2×2 matrices A, with independent random numbers as matrix elements $A_{n,m}$. In the case of Gaussian orthogonal ensembles (GOE) the matrix elements $A_{1,1}$,$A_{1,2} = A_{2,1}$ and $A_{2,2}$ can be transformed by orthogonal transformations. Using infinitesimal transformation techniques, the distributions of the matrix elements $A_{n,m}$ is determinable as a Gaussian. The mean E_0 and standard deviation σ are free parameters of the distribution. By investigating eigenvalues E_α and E_β instead of matrix elements, it is possible to reduce the number of free parameters, if the matrix is characterized by the eigenvalue distances $s \equiv |E_\alpha - E_\beta|$. Normalization ($\langle s \rangle = 1$) of the corresponding distribution reduces a further parameter. The normalized level spacing distribution is a parameter free Wigner distribution

$$P_{\mathrm{GOE}}(s) = \frac{\pi s}{2} \exp\left[-\frac{\pi}{4} s^2\right]. \tag{3.15}$$

Because $P_{\mathrm{GOE}}(s) \to 0$ for $s \to 0$, the probability of degenerated or similar eigenvalues is zero or suppressed. This is known as eigenvalue repulsion. For large level spacings the Wigner distribution has a Gaussian tail.

The matrix elements of a hermitian matrix with random complex numbers and invariance under unitary transformations represents a Gaussian unitary ensemble (GUE). The eigenvalue spacing distribution of a Hamiltonian with broken time reversal symmetry is an example for this ensemble. The Wigner distribution of the level spacings is similar to Equation (3.15)

$$P_{\mathrm{GUE}}(s) = \frac{32}{\pi^2} s^2 \exp\left[-4\frac{s^2}{\pi}\right]. \tag{3.16}$$

If rotational symmetry is broken, the random quaternion matrix elements of a symplectic matrix form a Gaussian symplectic ensemble (GSE). The distribution $P_{\mathrm{GSE}}(s)$ is similar to the Wigner distribution for the GOE case (Equation (3.15)), but for small level distances s it does not scale linearly but $P_{\mathrm{GSE}}(s) \propto s^4$.

P_{GOE}, P_{GUE}, and P_{GSE} are a good approximations for level spacing distributions of large matrices with corresponding symmetry, as numerical investigation showed, even for sparsely filled matrices. Consequently, the eigenvalue spacing distributions of the tight-binding Hamiltonian (2.10) can be described by random matrix theory results, if some requirements are fulfilled. There are two cases for which the Wigner distributions are not correct: (i) The matrices are not disordered. The eigenvalue of ordered or nearly ordered systems are nearly equidistant and some are degenerated. Therefore, they can not be repulsive and are independent of each other. (ii) The eigenstates are localized. If the eigenstates are localized, they do not overlap and are therefore independent.

The level spacings of independent eigenstates are described by the Poisson distribution

$$P_{\mathrm{P}}(s) = \exp[-s]. \tag{3.17}$$

In this case, the levels do not repel each other, the contrary is true; degeneration is probable, $P_{\mathrm{P}}(0) = 1$. The tail of the Poisson distribution is not Gaussian, but a simple exponential decreasing, slower than the Wigner distributions (3.15) and (3.16).

Therefore, level spacing distributions of tight-binding Hamiltonians are adequate for investing metal-insulator transitions. The corresponding distributions $P_{\mathrm{P}}(s)$ for localized states and $P_{\mathrm{GOE}}(s)$ or $P_{\mathrm{GUE}}(s)$ for extended states are only true for infinite system sizes. For finite systems, the level spacing distributions are somehow in between, reaching the limiting distributions for increasing system sizes. Therefore, if $P(s)$ is changing towards a Poisson distribution, the state is localized. If it changes toward a Wigner distribution, it is extended. At the critical disorder the level spacing distribution is system size independent as predicted by scaling theories.

If a magnetic field is imposed, the level spacing distribution of extended states is described by P_{GUE}. Examples of level spacing distributions for different disorder strengths W in the Anderson model are presented in Figure 3.3 for (a) without and (b) with small magnetic field.

For practicability reasons, $P(s)$ is not investigated directly, but finite-size scalings of derived values $\Gamma(L, W)$. The level spacing distributions for the metallic and insulating regime differs [183], therefore, a quantity $\Gamma(L, W)$ describing the metal-insulator phase transition is singular at the critical point in respect to W for $L = \infty$. Three different constants are needed for each of the three different regimes, $\tilde{\Gamma}_m$ for the metallic, $\tilde{\Gamma}_c$ for the critical, and $\tilde{\Gamma}_i$ for the insulating case [91],

$$\Gamma(L, W) \xrightarrow{L\to\infty} \begin{cases} \tilde{\Gamma}_m & \forall W < W_c \\ \tilde{\Gamma}_c & W = W_c \\ \tilde{\Gamma}_i & \forall W > W_c \end{cases} . \tag{3.18}$$

Describing the same second order phase transition with characteristic length scale ξ, Γ has an equal finite-size scaling behavior as the conductance in Equation (3.12), i.e.,

$$\Gamma(L, W) = F(L/\xi(W)). \tag{3.19}$$

Although $\Gamma(L, W)$ is singular for $L = \infty$, it is analytical for finite sizes and, thus, F is expandable around the critical point, $F(x) =_{x\to 0} a + bx^{1/\nu} + cx^{2/\nu} + \dots$, leading to

$$\Gamma(L, W) \simeq \Gamma(L, W_c) + C|W - W_c|L^{1/\nu}. \tag{3.20}$$

This is correct for all quantities fulfilling condition (3.18) and obeying scaling relation (3.19).

In Equation (3.20) irrelevant scaling variables Ξ, decaying with the system size, are not considered. Although always present, they are important to take into account for hard boundary conditions [186, 187]. The scaling formula Equation (3.19) has to be extended to include relevant Υ and irrelevant Ξ scaling variables,

$$\Gamma = F(\Upsilon L^{1/\nu}, \Xi L^{y}). \tag{3.21}$$

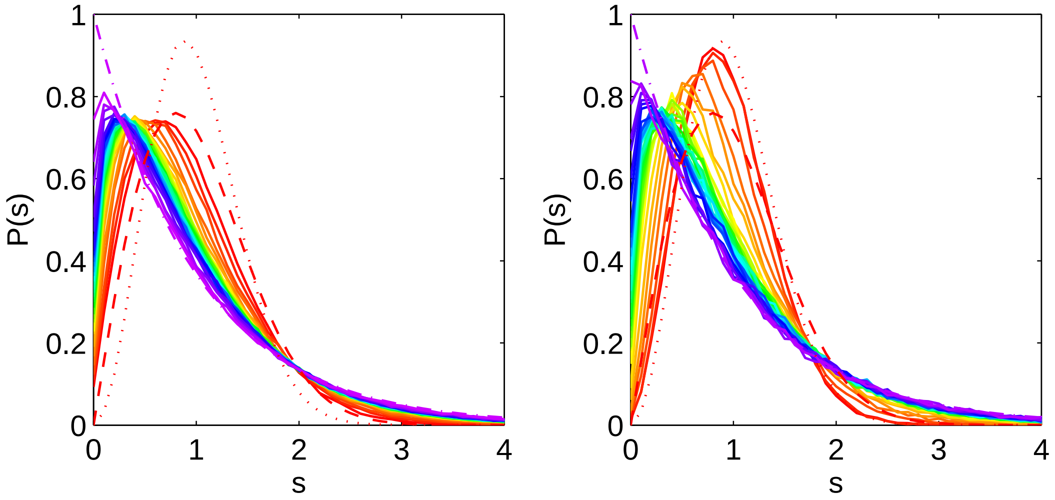

Figure 3.3.: Level spacing distributions P(s). The Poisson distribution is the dash-dotted purple curve. The GOE (GUE) distribution is the dashed (dotted) red curve. The lines are level spacing distributions of a 3d Anderson model using the tight-binding Hamiltonian (1.5). Disorder strength W is increased from red lines to blue lines. (a) System size $L = 20$. A clear transition from GOE (dashed red curve) to Poisson (dash-dotted purple curve) behavior is observed. The disorder is increased from $W = 10$ (continuous red curve) to $W = 23$ (continuous purple curve). (b) A magnetic flux per plaquete $\phi = 10^{-3}$ is imposed on a lattice with system size $L = 40$. A clear transition from GUE to Poisson behavior is observed as the disorder strength increases from $W = 8$ (continuous red curve) to $W = 23$ (continuous blue curve).

If irrelevant scaling variables do not introduce discontinuities, F is expandable not only around the relevant scaling variable Υ

$$\Gamma = \sum_{n=0}^{n_R} \Upsilon^n L^{n/\nu} F_n(\Xi L^y), \tag{3.22}$$

up to order n_R, but also around the irrelevant Ξ

$$F_n(\Xi L^y) = \sum_{m=0}^{n_I} \Xi^m L^{my} F_{nm}, \tag{3.23}$$

up to order n_I. The scaling variables are analytical functions of the dimensionless disorder $w = (W_c - W)/W_c$ and therefore equally expandable ,

$$\Upsilon(w) = \sum_{n=1}^{m_R} b_n w^n \quad \text{and} \quad \Xi(w) = \sum_{n=0}^{m_I} c_n w^n, \tag{3.24}$$

up to order m_R for the relevant and m_I for the irrelevant variables, respectively. The relevant scaling variable vanishes at criticality, thus, $b_0 = 0$, whereas c_0 is finite, introducing a size dependent error. A size independent Γ_{corr} at criticality is reestablished by subtracting the terms including irrelevant variables. The absolute scale of the arguments are undefined, but fixable by choosing, e.g., $F_{01} = F_{10} = 1$ in (3.23). The total number of fitting parameters is $N_p = (n_I + 1)(n_R + 1) + m_R + m_I + 2$.

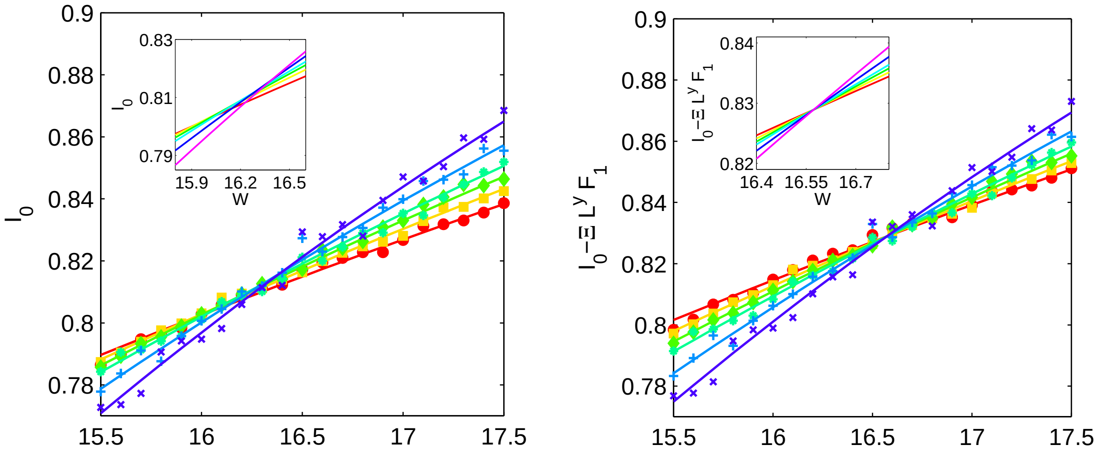

(a) (b)

Figure 3.4.: The localization parameter $I_0 = \langle s^2 \rangle / 2$ versus disorder W for system sizes $L/a = 14$ (red circles), $L/a = 17$ (yellow squares), $L/a = 20$ (green diamonds), $L/a = 23$ (light blue stars), $L/a = 30$ (blue pluses), and $L/a = 40$ (pink crosses). The lines correspond to fits of Equation (3.27). (a) The symbols correspond to I_0. A transition from extended states for small W to localized ones for large W is seen for all sample sizes. Nevertheless, the critical crossing point cannot be observed directly due to finite size effects. Inset: the region around $W = 16.1$ zoomed in; there is no single crosspoint. (b) Corrected values of I_0 where the influence of the irrelevant variables is subtracted. A clear transition can be seen at $W_c \approx 16.57$; all lines cross at one distinct critical disorder.

Two common scaling quantities, used in Chapters 7 to 9, are the second moment of level spacing

$$I_0(L) \equiv \frac{1}{2}\langle s^2 \rangle \equiv \frac{1}{2}\int_0^\infty s^2 P(s) ds, \tag{3.25}$$

and

$$\gamma(L) = \frac{\int_2^\infty P(s)ds - \int_2^\infty P_{\mathrm{W}}(s)ds}{\int_2^\infty P_{\mathrm{P}}(s)ds - \int_2^\infty P_{\mathrm{W}}(s)ds}, \tag{3.26}$$

where P_{W} is the Wigner distribution being P_{GOE} when no magnetic field is imposed and P_{GUE} else. The second moments of Poisson, GOE, or GUE distributions are $I_{0,\mathrm{P}} = 1$, $I_{0,\mathrm{GOE}} = 0.637$ and $I_{0,\mathrm{GUE}} = 0.589$. The scaling quantity $\gamma \to 0$ for extended states and $\gamma \to 1$ for localized states if $N \to \infty$. In contrast to I_0, the calculation of γ depends on the assumed symmetry of the system.

In Figure 3.4 an example case is depicted of a 3d Anderson model on a cubic lattice with diagonal disorder and hard boundary conditions. I_0 is expanded up to orders $n_I = 1$, $n_R = 3$, $m_R = 1$ and $m_I = 0$ such that

$$I_0(W, L) = F_0(\Upsilon L^{1/\nu}) + \Xi L^y F_1(\Upsilon L^{1/\nu}). \tag{3.27}$$

In (a) I_0 is shown without any corrections. In the inset the crossing region is enlarged, no well definable crossing point exists, i.e at criticality I_0 is size dependent. In (b) the correction $I_0 - \Xi L^y F_1$ is shown. The lines cross at one well defined point as seen in the inset. The critical disorder is given by $W_c = 16.57 \pm 0.13$ (see Chapter 7) which is in agreement with the newest numerical result $W_c \approx 16.54$ [187]. For periodic boundary conditions, the effect of the irrelevant scaling variables is negligible [187].

3.2.3. Results for the Anderson transition

Since the eighties it is known that a phase transition in a 3d Anderson model exists [138] which is equivalent to a metal-insulator transition [132, 94]. The typical value for the critical disorder $W_c \approx 16.5$ for a boxed potential distribution has been confirmed numerically [139, 169, 91, 86, 186, 187]. Applying a Gaussian potential distribution, the critical disorder is $W_c \approx 21.29$ [186] and in the Lloyd model $W_c \approx 4.27$ [186]. For smaller disorder W the electronic eigenstates are extended, the localization length λ is infinite. Furthermore, the wave amplitudes do not decay exponentially. Above the critical point, $W > W_c$, the states are localized. For the Anderson model with non-diagonal disorder the states are only localized near the band edges [32]. Non-diagonal disorder is, therefore, weaker than diagonal disorder.

It needs higher accuracy and a large numerical effort to determine the values of the critical exponent ν. Therefore, the values changed in the same time accuracy improved. The values are $\nu = 1.2 \pm 0.3$ [119], $\nu = 1.34 \pm 0.1$ [91], $\nu = 1.41 \pm 0.11$ [86], $\nu = 1.57 \pm 0.02$ [186], and $\nu = 1.56 \pm 0.02$ [187].

For the case of a four dimensional $(4d)$ Anderson model the critical disorder rises to $W_c \approx 35$ and $\nu \approx 1$ [170]. For higher dimensions an extrapolation $W_c \approx 16.5(d-2)$ and $\nu \approx 0.8/(d-2) + 0.5$ was proposed [170].

For quantum percolation on a quadratic lattice it is believed, but not undisputed [144, 117], that all eigenfunctions are localized ($p_q = 1$) [200, 190, 151, 54] as predicted from the scaling theory analysis presented above [1]. For quantum percolation on a cubic lattice the critical occupation probability $p_q \approx 0.44$ [117, 191, 192, 123] for site percolation, and critical connection probability $p_q^b \approx 0.34$ [144, 191, 38, 24] for bond percolation are found. These values are definitely lower than 1 and higher than the critical classical values p_c (see Section 1.1), thus a true quantum phase transition is observable.

The values for the critical exponent ν_q are similar to the Anderson transition: $\nu_q = 1.6 \pm 0.2$ [192], $\nu_q = 1.35 \pm 0.1$ [24], and $\nu_q = 1.46 \pm 0.09$ [105]. Similar critical exponents are expected, because the Anderson model and quantum percolation are in the same universality class.

Networks are infinitely dimensional objects. As shown in Section 2.2 quantum and classical waves can be described using the same formalism concerning the localization properties in disordered systems. Therefore, it is not important whether the network is a large molecule or an optical network with beam splitters as nodes and fibers or cavities as the edges. Since optical fibers have a very low loss rate, there is no essential difference between connecting neighboring nodes of the network and far away ones. As a result, also the physical distance of the nodes has no importance, in contrast to the scenario of a large molecule.

For Cayley trees [166] and different types of networks [167] $\nu = 0.5 \pm 0.15$, as expected for an infinite dimensional object [170]. In Chapter 9 a more detailed introduction and review is given. The critical disorder W_c depends on the type of topology, especially the mean number of neighbors (Chapter 9) and other topological quantities as e.g. clustering (Chapter 8). It is even possible to generate phase transitions with zero diagonal disorder by a mere change of clustering (Chapter 8).

A large number of experiments are devoted to understand the Anderson model. The 3d localization transition is studied on doped semiconductors, being a typical example of disordered media. Such systems are usually Si:P, Si:B, Si:As and Ge:Sb. Acceptors and donors are combined to allow variation of disorder and electron concentration independently. Most of the results reveal a conductivity exponent $s \approx 1$ [201, 220, 70, 87]. This is in contradiction to the above numerical results. One has to keep in mind that the numerical results are calculated for non-interacting electrons. Coulomb interaction affects the critical exponent [19], therefore, the results are not directly comparable.

To avoid these complications, experiments are also performed using classical waves. In the case of Anderson localization of light, experimental efforts turned out to be challenging. The difficulty arises due to similar characteristic signatures of photon absorption and wave localization, for both the transmission decreases exponentially. Therefore experimental results using powder of micrometer scaled GaAs particles [215], in which exponential decreases of transmission is observed, is not undisputed [168, 216]. In [197] results of transmission measurements of light through strongly scattering samples of TiO_2 particles is presented. Deviation from diffusion was measured unexplainable by absorption, sample geometry or reduction of transport velocity. Furthermore, the deviation increases for decreasing mean free path of the particles.

A new promising research direction are measurements of Anderson localization of light in disordered photonic lattices. In these systems the light waves can be described by Schrödinger like equations. Disorder is either induced by variation of sample widths [127] or some optical disorder [172]. The transmission light intensities are compared with numerical solutions of the underlying theory which gives signatures for extended and localized states.

In all above experiments, the localized wave function can not be observed directly. Localization is derived from transmission or conductance properties. In very recent experiments with Bose-Einstein condensates it is possible to measure the shape of the wave function by measuring the atomic density of the Bose-Einstein condensate [25, 165]. Thereby, exponential decay of the wave function and the transition to extended states can be observed.

3.2.4. Effect of magnetic fields

The effect of a weak magnetic field on the critical disorder W_c was derived in the eighties by Khmel'nitskii and Larkin [112]. They predicted that the shift of critical disorder can be described by a power-law

$$W_c(\phi) - W_c(0) = C\phi^{1/2\nu}. \tag{3.28}$$

The critical disorder changes, because the magnetic field introduces a new length scale $L_B = \sqrt{\hbar/eB}$ and thus $L_B/a = 1/\sqrt{2\pi\phi}$ (see Section 2.1). Therefore, the conductivity at $T = 0$ can be written by a power of the ratios ξ/L_B with $\xi = [(W - W_c)/W_c]^{-\nu} a$ the correlation length. So the conductivity is

$$\sigma(B, W) \propto f(\xi/L_B) \propto \Phi\left[\frac{W - W_c}{W_c}\left(\frac{\hbar}{eBa^2}\right)^{1/2\nu}\right], \tag{3.29}$$

and it vanishes at the critical disorder $W_c(B)$ for which both length scales are nearly equal $\xi/L_B \sim 1$, i.e.,

$$W_c(B) - W_c(0) \propto \left[\frac{eBa^2}{\hbar}\right]^{1/2\nu} \propto \phi^{1/2\nu}. \tag{3.30}$$

This phenomenological derivation is only true for small magnetic fields. The numerical verification of Equation (3.30) is the topic of Chapter 7.

Besides Chapter 7 there are no detailed investigations of critical parameters for small magnetic fluxes but numerical values for higher fluxes exist and are presented in Table 3.1. The critical disorder rises with higher fluxes up to the symmetry axes at $\phi = 1/4$[1]. A higher shift is achieved by introducing a random flux. In the case of the size dependent Ahoronov-Bohm flux, no shift of the critical disorder is observed [17].

---

[1] The critical parameters are equivalent for $\phi = 1/4 + \delta$ and $\phi = 1/4 - \delta$. See Section 2.1 for details.

Table 3.1.: Best fit estimates of critical disorder W_c and critical exponents for different fluxes in the Anderson model.

flux ϕ	W_c	ν	Ref.
1/20	17.67 ± 0.14	1.28 ± 0.15	[86]
1/10	17.81 ± 0.12	1.33 ± 0.18	[86]
0.15 ($\hat{=}$ 0.4)[1]	17.93 ± 0.15	1.38 ± 0.17	[86]
1/6 ($\hat{=}$ 1/3)[1]	18.32 ± 0.016	1.43 ± 0.04	[185]
1/5	18.06 ± 0.13	1.36 ± 0.15	[86]
1/4	18.376 ± 0.017	1.43 ± 0.06	[185]
1/4	18.35 ± 0.11	–	[58]
random	18.80 ± 0.04	1.45 ± 0.09	[108]
Ahoronov-Bohm	16.4	1.66	[17]

If at least a full flux quantum penetrates the system time reversal symmetry is fully broken and P_{GUE} is the correct level spacing distribution function of the extended state. An example of a transition from a Poisson distribution P_{P} to P_{GUE} is shown in Figure 3.3. The critical exponent ν in such a case corresponds to the GUE symmetry class. Comparing the values of the newest results for ν with magnetic fields with the newest values for ν without a magnetic field [187] the critical exponents of the two universality classes GOE and GUE are distinguishable.

A shift of the critical disorder is also seen in quantum bond percolation where the critical occupation probability shifts to $p_q = 0.308$ [105]. The critical exponent reduces and is similar to the cases of the Anderson model with magnetic field: $\nu_q = 1.24 \pm 0.08$ [105].

Part II.

Summary and discussion

Influencing pattern formation

Liesegang pattern formation is well described by several mean-field models. These state of art models are reviewed and discussed in Section 4.3. Investigations beyond mean-field predictions are rare and the few published ones are insufficient for understanding the role of disorder or even controlling Liesegang patterns by means of disorder [44, 45, 11]. Exactly this knowledge is desirable. One thus needs a model including fluctuations and disorder, and furthermore, a profound understanding of these effects. As a consequence, Section 4.4 introduces a lattice-gas model laying ground for further investigations. In Chapter 5 these lattice-gas simulations are used to investigate the influence of disorder on the pattern forming mechanism. The achieved understanding is utilized successfully in Chapter 6 to generate equidistant bands by variation of structural disorder.

The lattice-gas model is a further development of a nucleation and growth based model [44, 45]. The advancement is, besides an extension to three dimensions (3d), a more efficient treatment of the first stage, i.e. the reaction-diffusion process (see Section 3.1). Instead of explicitly simulating the production of C particles, they are inserted with a probability, approximated by an analytically available reaction rate. Using such approximation, simulations with high concentrations of C particles become feasible. These high concentrations are needed to drive the system closer to the mean-field limit, essential for the systematic investigation of fluctuations in Chapter 5.

In lattice-gas models fluctuations are naturally present, induced by the random walk of particles on a lattice. The implementation of disorder is straightforward. Besides that, lattice-gas simulations serve well as computational experiments, being in-between experiments and mean-field approaches. The processing of the results is similar to experiments with a wider range of possibilities to modify the system. As a result, apparent contradictions between analytical and experimental observations are reconciled successfully in Chapter 4. The same advantage is also beneficial for the designing of equidistant and more complex patterns in Chapter 6.

Experimental observations and analytical calculations lead to contradicting results for the ratio of the positions of two successive Liesegang bands, x_{n+1}/x_n. In the experimental case the ratio converges for larger n to $1+p$, with p the spacing factor (Equation (3.1)), whereas in the analytical case the ratio is equal to $1+p$ (Equation (3.3)). Lattice-gas simulation results follow the experimentally observed behavior. It is possible to reconcile both results by introducing an offset ξ, assuming the experimentally observed band positions x'_n are shifted, $x'_n = x_n - \xi$, due to an undefined first band. This shift is sufficient to explain the experimental observations. Knowing the source of the problem, a more convenient way to extract p is proposed. The spacing factor p and offset ξ are obtained as coefficients of a linear fit of the measured positions. Using linear regression methods, error estimates are well defined. It remains an open question how ξ can be derived from the basic constants. Because ξ can be extracted robustly, further investigations are feasible.

Similarly, competing empirical definitions exist for the spatial broadening of the Liesegang band widths. This width law is defined either as a linear function of width and position, or alternatively, as a power-law. Both definitions lead to equally good fitting results, due to the small value of the width compared to the position of the band. The theoretical description (Equation (3.6)) proposes a power-law behavior. The width w_n of the nth bands is not only proportional to its position, but it is also inverse proportional to the density of the band. The width law turns into a power-law, because the densities of the bands are in general not constant, but also a power-law. To compare this theoretical prediction with data of lattice-gas simulations the positions have to be shifted by ξ, leading to a mixture of linear and power-law. Especially for constant band densities, the width law is described best by a linear function of the positions. Because the mass of the bands has to be a linear function of the band position, it is possible to test the theoretical predictions, using the measured positions of lattice-gas simulations. Simulation results only lead to a linear mass dependence, if the offset ξ is incorporated. This strongly indicates that ξ is essential for a correct data analysis. A recent experiment [156] is re-analyzed, confirming these results. Also, when bands are designed (Chapter 6) the offset ξ is important for avoiding biases.

The importance of Chapter 4 for the next publications is twofold. Firstly, a fast lattice-gas simulation model is developed, tested and presented. Secondly, the important parameters are discussed and correct data processing and analyzing methods are proposed. These methods are essential for further investigations. Due to the solid groundwork of Chapter 4, the role of fluctuations is successfully tackled in Chapter 5. The motivation is derived from the fact that in the last decades experiments were performed with micrometer [82, 23, 78, 204] and even nanometer [148] sized widths of Liesegang bands. On such length scales thermal fluctuations of particle motion and defects in the structure are no longer negligible. The fact that Liesegang bands are scalable over several magnitudes of system sizes indicates that fluctuations do not necessarily destroy the pattern forming mechanism. Furthermore, it indicates that band formation is well described by mean-field approximations, including some effective constants.

The lattice-gas simulations in Chapters 4 to 6 are performed on 3d lattices. Consequently, fluctuations induced by C particle production can be neglected. The only source of fluctuations left is thermal motion of particles, i.e. their random walk, leading to fluctuations of local concentrations of C particles. A parameter sensible to small changes in particle concentration is the spacing factor p. The spacing factor depends critically on the equilibrium concentration c_0, due to the threshold character of nucleation. Since one or few nucleations are sufficient to grow a band, the fluctuations of concentrations of C particles are effectively increasing nucleation probabilities, and thus effect the value of p. Increasing fluctuations reduces p and enhances pattern formation, because more patterns emerge in a given volume. Furthermore, it is possible to achieve pattern formation in parameter ranges, where no patterns would occur in mean-field approximations, i.e. for $c_0 < K_{sp}$ where K_{sp} denotes the nucleation threshold. For larger concentrations of C particles the effect of fluctuations reduces, and the mean-field values are reestablished.

Further sources of fluctuations are introduced by structural disorder. A way to simulate such disorder is heterogeneous nucleation, i.e., a non-constant nucleation threshold K_{sp}. For simplicity a normal distribution with mean K_{sp}^{het} and standard deviation σ is assumed. If σ is large, nucleation occurs already when the mean concentration of C particles is much smaller than K_{sp}^{het}. Therefore, K_{sp} is effectively reduced and as a result p also reduces. If σ is large enough, patterns are observed in parameter regimes where no mean-field solution exists, and thermal fluctuations are negligible. To sum up, patterns emerge when defects, impurities, or fluctuations are increased in a sample, and fluctuations and disorder act as ordering mechanisms. This seems counter intuitive, but is nevertheless the cause why the length scales of Liesegang pattern experiments are scalable over several orders of magnitudes. The drawback is an increased instability in the reproducibility of experiments, due to difficulties in preparing identically disordered samples. The main reason for the ordering effect of fluctuations and disorder is the existence of a threshold. A similar effect can be found in stochastic resonance, where an undetectable signal is made detectable by addition of noise [217, 74, 101]. The reason for undetectability is usually a threshold within the signal processing device. Noise leads to fluctuations, hence, the signal overcomes the threshold and detection becomes feasible.

For large concentrations the effect of thermal fluctuations can be neglected and heterogeneous nucleation is the only relevant effect of disorder remaining. In that case it is possible to extract the mean nucleation threshold K_{sp}^{het}, a quantity difficult to measure, by a geometrical analysis.

Therefore, the ansatz presented in this thesis can lead to a better understanding of nucleation.

Besides the interesting results on fluctuations, the analytical description of the spacing factor p (Equation (3.5)) is extended in Chapter 5 to include fluctuations and disorder. The empirically extended formula is an important tool for the designing of patterns in Chapter 6. Designing special kinds of patterns is an active research topic. In nature one finds reaction-diffusion processes controlling and building structures from molecular to macroscopic length scales. Reaction-diffusion systems have been on target for years to be utilized in the designing of devices in a *bottom-up* approach [82]. In this approach devices are build using pattern formation and self-organization processes, rather than an active manipulation of the substrates. One example is lithography, where the precision is limited by the employed tools. In bottom-up approaches, on the other hand, the precision is limited only by the length scale of the basic interactions, in an ideal environment. A further advantage of material design using reaction-diffusion processes is the possibility to access the third dimension. Patterns can form in the direction perpendicular to the surface, and are not limited to the surface. A combination of bottom-up and traditional techniques is therefore interesting, where 3d structures are relevant, e.g., for optical lattices. The main challenge for bottom-up approaches is to control the pattern formation such that predefined bands form. One of the most promising bottom-up approaches is Liesegang pattern formation, especially for devices where periodic bands or rings are of interest, e.g., in optical filters. One of the possibilities discussed in Chapter 6 is equidistant banding. There are two possible definitions for equidistant bands. Consecutive bands can be defined as equidistant, if either the distance of their band borders, or the distance of their centers is constant. Both definitions are only equivalent if the band widths are constant. The center oriented approach is more convenient, and therefore used in Chapter 6.

To influence the distance of the patterns, the spacing factor p has to be varied. There are several ways how p can be influenced. Obvious possibilities are: temperature gradients, boundary condition variations, and tweaking of the reaction process. A further possibility is the spatial modification of the substrate, e.g., introducing a fractal material in which the fractal dimension changes spatially. The path chosen in Chapter 6 is a large-scale modification of the nucleation conditions either directly or by introduction of impurities and defects. To control p, it is crucial to know its dependence on the basic parameters as described in Chapter 5.

The result for the homogeneous case is a spatially decreasing K_{sp}, hence, the number of possible equidistant bands is limited. To optimize the number of bands the parameter has to be tuned such that K_{sp} decreases slowly. It is possible to achieve inter-band distances in the heterogeneous case by increasing the disorder in the substrate, e.g., by creation of nucleation seeds by intense laser irradiation [113]. This shows that influencing pattern formation by controlling disorder in a medium is indeed possible. The maximum number of bands that can be produced using this method is limited. When the distribution is too broad, basically near the value of the mean, nucleation will become random and no structures evolve. Therefore, fine tuning of the parameters is necessary.

There are in total three (four) unknown parameters in case of homogeneous (heterogeneous) nucleation, needed to model width and fluctuations on one side, and the offset parameter ξ on the other side. Because ξ is not known a priori, equidistant bands can only be generated in an iterative experimental (or simulation) procedure. An iterative graphical scheme is suggested to extract the correct ξ, leading to unbiased equidistant band formation. In conclusion, constant inter-band distances are achieved using both methods. The only difference between the bands produced by variation of homogeneous nucleation and the ones created by variation of disorder is a larger standard deviation of inter-band distances for the latter. Although the band distances are equal, the band widths reduce spatially, whereas the masses of the bands are constant. This behavior is understood using the analytical methods introduced in Section 2.3. The iterative procedure introduced in Chapter 6 is transferable to other schemes for the band distances. Furthermore, other geometries can be implemented in the lattice-gas model. Therefore, the results of Chapters 4 to 6 are applicable for designing arbitrary patterns in arbitrary geometries. An important open question, which might have to be settled before these results can be exploited, is, how to achieve equidistant patterns with constant band widths. To accomplish this, the role of the band densities has to be investigated further.

The results presented in Chapters 4 to 6 and also recent publications [150, 21, 142] indicate the great progress in understanding Liesegang pattern formation that has been achieved in the last decade. Less than three years ago controlled equidistant band formation was unreachable. Now, with the results of [21] and Chapter 6 the feasibility is shown in complementary elegant ways. I believe that the results presented here are a motivation for further experiments, not only leading to new devices and applications, but to a deeper understanding of nucleation and growth processes in pattern formation.

Influencing localization

The influence of disorder on the transport properties of quantum and classical waves is actively investigated (see Section 3.2). The Anderson model is a common choice for a numerical approach dealing with this topic [9]. Less investigated fields are on one hand structural-topological disorders beyond quantum percolation [24], and on the other hand special forms of off-diagonal disorders such as the magnetic field.

A magnetic field shifts the metal-insulator transition at a critical disorder W_c in the Anderson model [9] due to a new length scale, the magnetic length $L_B/a = 1/\sqrt{2\pi\phi}$ (see Section 3.2.4). The transition occurs when the magnetic length and the correlation length ξ are equal, $L_B \sim \xi$. Utilizing this idea, Khmel'nitskii and Larkin **(author?)** [112] predicted the shift of W_c for small fluxes ($\phi \to 0$) to be a power-law $W_c(\phi) - W_c(0) = C\phi^{\beta/\nu}$ with $\beta = 1/2$ (see Section 3.2 and Equation (3.28)). For finite systems though, the irrelevant length scale of the system size L may play a role for $L_B > L$. Therefore, a solid numerical calculation includes system sizes larger than L_B, but small magnetic fluxes. The combination of both criteria requires large system sizes, making numerical confirmations of [112] a challenging task. As a result, nearly all numerical calculations on magnetic fields in an Anderson model are for large or random fields.

Only in one publication Khmel'nitskiis and Larkins prediction is confirmed, although with large error bars [58]. Furthermore, the values for W_c and ν are only presented graphically and Khmel'nitskiis and Larkins prediction is fitted over the full flux range, while the theory is expected to be true for small fluxes only. Therefore, investigations going beyond these results are desirable. In Chapter 7 results of extensive numerical calculations are presented for 3d lattices of linear sizes from $L/a = 14$ to $L/a = 40$. The latter is a great challenge, even for state-of-art computer resources. To prevent discontinuities of the magnetic field at the boundaries, hard boundary conditions are applied. Irrelevant scaling variables are not negligible for such boundary conditions and are taken care of in a finite-size scaling analysis. The smallest system size determines the smallest magnetic flux considered, $\phi = 0.0008$. The flux with the largest effect is $\phi = 1/4$, due to the symmetry of the problem (see Section 2.1).

A magnetic field not only shifts the critical disorder but also breaks the time reversal symmetry of the Hamiltonian. To achieve this, the total flux quantum penetrating the system has to be at least one. For such systems the Gaussian unitary ensemble (GUE) is the correct level distribution, not the Gaussian orthogonal ensemble (GOE). At the critical disorder the crossover is independent of the total flux through the sample, since at criticality the distribution does not depend on size. Therefore also for fluxes, $\phi \leq 0.004$, where the smallest system sizes are not penetrated by a full flux quantum, it is possible to confirm [112] approximately obtaining $\beta = 0.45 \pm 0.05$. Also for larger fluxes, $0.004 < \phi \leq 0.1$, where all system are penetrated by at least one flux quantum, a power law can be confirmed approximately yielding $\beta = 0.6 \pm 0.07$. Although at criticality the critical disorder has to be independent of the size it seems to be a cross over between both regimes. This cross over could be caused by a full development of the GUE symmetry upon increasing ϕ. Surprisingly, the prefactor Δ for the shift of critical disorder is larger than anticipated. Already for very small magnetic fields ($\phi < 0.1$) all of the total shift has occurred.

Supplementary results presented in Chapter 7 are the critical level distributions for different boundary conditions and fluxes. Interestingly, for hard boundary conditions the critical level spacing distributions changes only slightly when the magnetic fields are applied in contrast to a drastic shift for periodic boundary conditions.

The shift exponent β/ν depends inversely on the critical exponent ν which characterizes the behavior of the localization length at the metal-insulator transition. Introducing long-range bonds on a lattice structure reduces ν systematically, reaching $\nu = 0.5$ for an infinitely dimensional system. This approach could be utilized to further increase the shift in order to build sensible binary magnetic detectors.

Long-range interactions introduce structural-topological disorder to the system. The same type of disorder also occurs in non-lattice topologies like networks. As in the case of a magnetic field, topological disorder shifts the metal-insulator transition. In Section 9.2 earlier results regarding metal-insulator phase transitions for several types of networks are reviewed and their critical disorder W_c and critical exponent ν are reported. The network structure is fixed while only diagonal disorder is varied, similar to the Anderson model. Comparing the results for the critical disorder W_c and mean number of connection per nodes, i.e. mean degree (see Section 1.3), reveals that higher mean degree leads to higher W_c. In Chapter 8 and Section 9.3 the effects of topological disorder are investigated more systematically. Instead of changing the degree, which would correspond to percolation [47], the local structure is modified by changing the probability of triadic closure, introduced in Section 1.3 as clustering index C_i of each node i (Equation (1.12)).

Clustering has some properties similar to the connection probability p in percolation. Starting from a non-clustered network, a demand for higher clustering leads to the disintegration of small components with high clustering. At first, triangles of nodes with degree $k = 2$ disintegrate, having the highest possible mean clustering coefficient of $C = 1$, later also larger structures disintegrate. Localization is only well defined on the infinite cluster. Parameters of the full network, such as the degree distribution $P(k)$ and the clustering coefficient C, are irrelevant parameters of the metal-insulator phase transition. The relevant parameters are the degree distribution $P_g(k)$ and the clustering coefficient C_g of the infinite cluster. The interesting order parameter for the metal-insulator phase transition induced by clustering is C_g. The global clustering coefficient cannot capture adequately the local properties of clustering, therefore C_0 as introduced in Equation (1.14) is a more suitable order parameter. The relationship between C_0 and C_g is investigated in Section 9.3 and it is shown that both are linearly dependent, making C_0 and C_g interchangeable as scaling variables. These results are discussed in Section 9.3 in more detail compared with the initial letter publication in Chapter 8. Section 9.3 also contains some supplementary material concerning clustering missing in Chapter 8, although, the results on the metal-insulator transition are identical.

The context of the investigations in Section 9.3 and Chapter 8 are optical scale-free networks with sizes $N = 2000$ to $N = 20000$. The large system sizes are required for large clustering, due

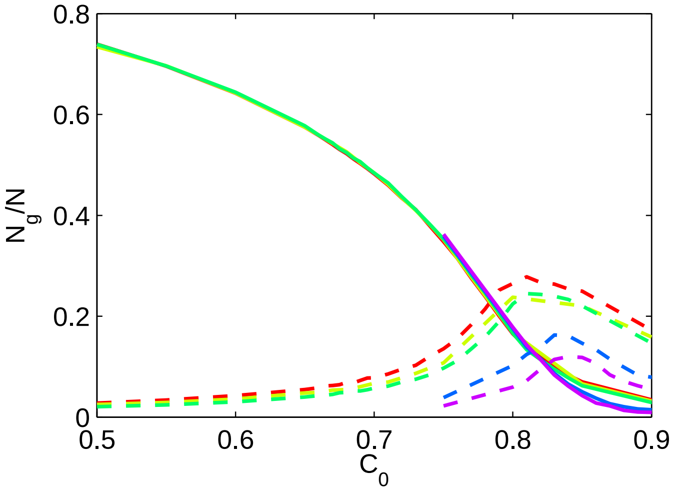

Figure II.1.: Example of clustering dependencies of the infinite cluster (solid curves) and second largest cluster (dashed curves) for a scale-free network with $\lambda = 5$. The curves are normalized by the network size. The values for the second largest cluster are additionally enlarged by a factor of 10. The color code for the system sizes are: N=10000 (red), N=15000 (light green), N=20000 (green), N=50000 (blue), N=100000 (purple).

to the shrinking of the infinite cluster. Different networks with degree exponents from $\lambda = 3$ to 6 and $C_0 = 0$ to $C_0 = 1$ are examined. For other networks, as e.g., Erdös-Rényi networks, the results of Chapter 8 also hold, but these have not been published yet. The dynamics are described by a tight-binding Hamiltonian as defined in Section 1.1 which is also correct for optical networks as derived in Section 2.2.

The energy level spectra are analyzed using level statistical methods. The result is that the level spacing distributions are similar to those in the case of the Anderson transition. A transition from near Wigner distribution for $C_0 = 0$ to near Poisson distribution for high clustering is clearly seen, for $\lambda \geq 4$ even if $W = 0$. Thus, clustering induces a transition similar to an Anderson transition even without compositional disorder.

The critical disorder W_c, as well as the critical clustering $C_{0,q}$, and the critical exponent ν are extracted, using the finite-size scaling quantity γ (Equation (3.26)) extended to include C_0 as second scaling variable. For different compositional disorders W_c and clustering C_0 the full phase diagram is presented. Higher degree exponents λ lead to reduced critical clustering $C_{0,q}$ and critical disorder W_c. These results are in agreement with those reviewed in Section 9.2, because higher degree exponents λ correspond to lower mean degrees. The results for the critical exponents ν are in agreement with mean-field calculations predicting $\nu = 1/2$.

Besides a quantum phase transition, clustering also induces a classical phase transition similar to percolation but not focused in the publication in Chapters 8 and 9. By enhancing clustering it is possible to break the network, i.e., a critical $C_{0,c}$ exists, such that above $C_{0,c}$ all clusters are finite clusters. Therefore, it is important to make sure that the quantum phase transition at $C_{0,q}$ is well separated from the classical one at $C_{0,c}$. It is possible to extract $C_{0,c}$ by examining the second largest cluster. As long as an infinite cluster exists, the second largest cluster will grow on its expense. After the infinite cluster breaks, all clusters are equal and will disintegrate into smaller and smaller clusters. Therefore, the size of the second largest cluster N_2 peaks for $C_0 = C_{0,c}$. In the additional Fig. II.1 the reduction of the largest component (solid curves) and of the second largest component (dashed curves) is shown. The colors represent different system sizes. For nearly all clusterings, the infinite clusters reduce in the same manner. This is no longer true for the second largest cluster, where a peak at around $C_0 \approx 0.85$ is clearly visible. The peak shifts to higher clusterings for larger system sizes, approximating the correct value. Therefore, $C_{0,c} > 0.85$ is clearly separable from the critical quantum transition $C_{0,q} \approx 0.69$ (see Chapter 8). The same analysis is done for several degree exponents λ (see Section 1.3 for a definition of λ). For all explored λ, classical and quantum transitions are clearly separable. For $\lambda < 4.5$, no classical transitions are found and for $\lambda < 4$ no quantum transitions with $W = 0$ are observed. Therefore, a regime $4 < \lambda < 4.5$ exists, where only quantum transitions occur.

Chapter 8 and Section 9.3 show that clustering induces a transition similar to the Anderson transition even without compositional disorder. Therefore, clustering represents a new degree of freedom that can be used to induce and study phase transitions. The similarities between clustering and percolation are obvious. In both cases one finds a quantum transition before a classical one. These similarities call for further explorations leading to a better understanding of the interplay between topological structures and metal-insulator transitions. Clustering is only one of several local properties of a network. The results of Chapters 8 and 9 can be extended to further properties as, e.g., degree-degree correlations. Such investigations additionally feature an interesting approach to understand the local properties of localization effects. I believe, the results presented in this thesis will open new doors to deeper understanding of localization effects in disordered systems.

Part III.

Publications

4. Comparison of models and lattice-gas simulations for Liesegang patterns

Journal: European Physical Journal Special-Topics **161**, 121-141 (2008)

Authors: Lukas Jahnke and Jan W. Kantelhardt
Institute: Institute of Physics, Theory group, Martin-Luther-Universität Halle-Wittenberg, 06099 Halle, Germany

Abstract: For more than a century Liesegang patterns – self-organized, quasi-periodic structures occurring in diffusion-limited chemical reactions with two components – have been attracting scientists. The pattern formation can be described by four basic empirical laws. In addition to many experiments, several models have been devised to understand the formation of the bands and rings. Here we review the most important models and complement them with detailed three-dimensional lattice-gas simulations. We show how the mean-field predictions can be reconciled with experimental data by a redefinition of the distances suggested by our lattice-gas simulations.

4.1. Introduction

In recent years the general interest in self-organized structures is growing, triggered by the idea of cheap and fast production of nano-scaled devices. One of the promising effects for obtaining such devices is Liesegang pattern formation, based on a reaction-diffusion process. Experimental evidences for Liesegang patterns in solid materials on the nano-scale have already been obtained, see, e. g., [148, 23, 82]. For example, periodic patterns of silver nano particles in glass were observed by electron microscopy [148]. If it became possible to control the growth of such patterns with experimentally tunable parameters, self-organized optical devices could be made. In addition, the Liesegang phenomenon is an interesting research topic on its own due to the simple patterns arising out of complicated reaction and diffusion processes.

Since the first description of Liesegang rings in gels by the German chemist Raphael Eduard Liesegang in 1896 [134], many experiments and several models have been devised to understand the formation of the bands and rings. Although the basic problems are solved and four universal empirical laws have been found common to all experimentally observed Liesegang phenomena, there are still open questions. In literature misunderstandings regarding the exact definition of the measured quantities cause some discrepancies between the experimental results and the predictions of theoretical (mean-field) models. In this paper, we review the most important models for Liesegang pattern formation and complement them with extensive lattice-gas simulations of the reaction-diffusion processes. Based on our three-dimensional (3d) simulation results, we find a way to reconcile most experimental observations with the results obtained in mean-field models. In addition, we obtain evidence that fluctuations in 3d reaction-diffusion processes may play an important role in Liesegang pattern formation on the nano-scale.

The paper is structured as follows. Section 4.2 describes the main experimental findings, which

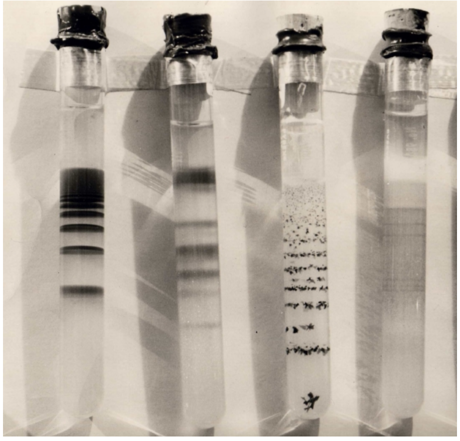

Figure 4.1.: (Colour online) experimental examples of Liesegang patterns in test tubes. Agent A is injected from the open end (top) of the tube, which contains agent B dissolved in a gel, yielding a linear geometry (Figure by D. B. Siano, `http://commons.wikimedia.org/wiki/Image:Liesegangrings.jpg`).

can be summed up in four empirical universal laws describing the Liesegang patterns. Section 4.3 reviews previous work on models reproducing these laws. After an overview including a discussion of recent trends, we focus first on reaction-diffusion models with thresholds, and describe afterwards the spinodal decomposition model and a kinetic Ising model. Section 4.4 is devoted to our studies based on lattice-gas simulations, presenting both the numerical method, the main findings, and a suggestion for reconciling the mean-field predictions with both, the experimental data and our 3d simulation results by a redefinition of the distances. Section 4.5 summarizes our findings and gives an outlook on further work on Liesegang pattern formation.

4.2. Experimental findings and empirical universal laws

In his original experiment, Liesegang covered a glass plate with a layer of gelatin impregnated with potassium chromate [134]. Then he added a small drop of silver nitrate in the centre. As a result, silver chromate was precipitated in the form of a series of concentric rings with regularly varying spacings. These rings became famous as Liesegang rings or more generally Liesegang patterns. Shortly after the first experiments, Wilhelm Ostwald presented an explanation for the occurrence of the rings [160], which is still the basis for most of the models today. The next important experimental findings followed several years later. In 1903, Morse and Pierce [152] investigated the formation time of the bands, observing diffusional dynamics, i. e., the time law. Jablczynski [97] showed twenty years later that Liesegang patterns follow a geometric series, i. e., the spacing law. Based on this observation Matalon and Packter [143, 161] investigated the functional dependence of the positions of the bands on the concentrations of the reacting agents in 1955.

The geometry of the pattern depends on the initial conditions for the reacting agents. Usually one agent (the inner electrolyte), represented by the B particles in the models, is initially homogeneously distributed in the sample or gel. The second agent (the outer electrolyte), represented by the A particles, is injected. If A is injected in the centre, precipitation rings are formed. If B is homogeneously distributed in a cylindrical tube and A is injected from one end of the tube, bands form perpendicular to the motion of the reaction front, see Fig. 4.1. The second experimental

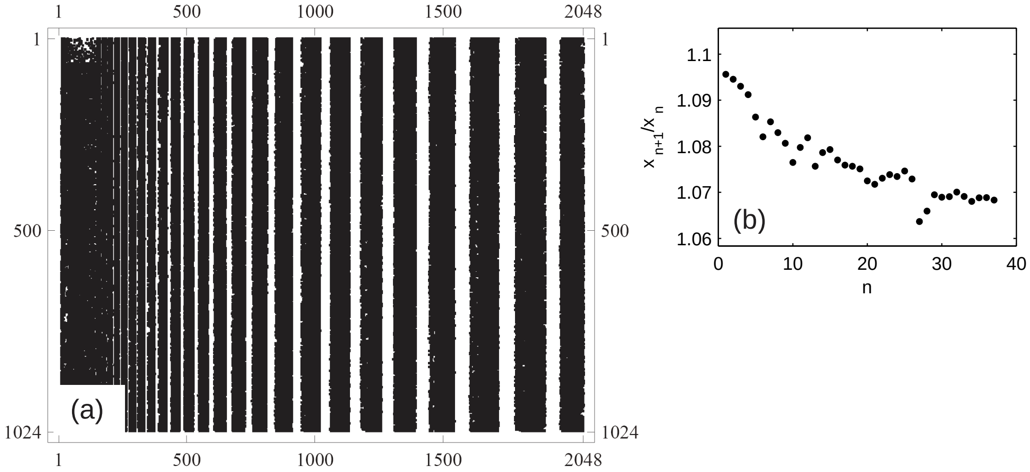

Figure 4.2.: Results of a 3d lattice-gas simulation of Liesegang band formation. (a) Injecting A from the left, Liesegang bands (black) with increasing distance form in the simulated lattice of $32 \times 32 \times 2048$ sites. To obtain the projection, all 32 two-dimensional slices were placed next to each other vertically. (b) The ratio x_{n+1}/x_n of the positions of the $(n+1)$st and nth band is plotted versus n. See Fig. 4.6 in Sect. 4.4.3 for the parameters of the simulation.

setup is more appropriate for a theoretical description because it is effectively one dimensional (1d) [85]. Most of the theoretical and experimental work was done using this linear configuration; here we also focus on the 'band' setup. Although Liesegang rings are basically a projection of the bands onto polar coordinates, spiral patterns have been observed in the ring configuration exclusively. They have no equivalent in the linear configuration.

To define the basic observables, we assume that the nth band forms at time t_n at distance x_n from the side where A is injected. The width of the nth band is denoted by w_n. Firstly, the position x_n is empirically found to be proportional to the square-root of the time t_n,

$$x_n \propto \sqrt{t_n}. \tag{4.1}$$

This rule called *time law* in literature has been confirmed experimentally many times [152, 182, 103, 154, 133, 199, 75, 155, 76].

Figure 4.2 shows that the position x_n of the nth band follows approximately a geometric series converging to the *spacing law* [97]

$$x_n \propto (1+p)^n \Leftrightarrow x_{n+1}/x_n \to 1+p \quad \text{for large } n \tag{4.2}$$

with $p > 0$ the spacing factor. Typical empirical values for p reported in literature range from 0.05 to 0.4 [148, 23, 154, 75, 76, 156].

A first systematic experimental analysis of the functional dependence of p on the concentrations of agents A and B was done by Matalon and Packter [143, 161]. They gathered experimental results on p and found a functional dependence on the concentrations of both agents, a_0 and b_0, respectively. This dependency is known as the *Matalon-Packter law* and takes the form

$$p = F(b_0) + G(b_0)\frac{b_0}{a_0}, \tag{4.3}$$

with F and G as dimensionless monotonously decreasing functions of b_0 [1]. F and G are not dependent on a_0 making p linearly dependent on $1/a_0$ for constant b_0. This can serve as a test for the validity of the Matalon-Packter law. In Sect. 4.3.3 we will show that Eq. (4.3) is just an approximation of a more general law in the limit of reaction fronts much faster than the diffusion of the B particles. This limit holds for most of the experiments, because a_0 is usually much larger then b_0 while both electrolytes diffuse equally fast. An exception seems to be the experiment with nanoscale silver particles in glass [148] where the diffusion of silver ions, the inner electrolyte, might be one magnitude faster than the diffusion of the outer electrolyte, hydrogen. This leads to a slower motion of the reaction front compared to the diffusion of the silver ions.

---

[1] In the original work, the Matalon-Packter law was introduced as $p = F(b_0) + G(b_0)/a_0$. The disadvantage of this equivalent definition is that $G(b_0)$ gets the dimension of b_0.

As can be seen in Fig. 4.2(a) the Liesegang bands are getting broader for larger n. It is possible to set up an empirical law describing the width w_n of the nth band as function of the position x_n. Experimentalists use two competing versions of the *width law*,

$$w_n = \mu_1 x_n + \mu_2 \qquad \text{and} \qquad w_n \propto x_n^\alpha \tag{4.4}$$

see, e. g., [103, 156, 55] and [76, 44, 164, 60], respectively. We are not aware of any papers comparing the two versions. In addition, different values of the exponent α in the second version have been published. The experiment with nanoscale silver particles in glass can be fitted by $\alpha \approx 0.7$ [148] (using the second version of Eq. (4.4)), but the results can be equally well fitted by the first version. Most other papers report larger values of α, e. g., $0.9 < \alpha < 1$ [60]. Publications of early reactive lattice-gas simulations, where the second version was first introduced, fit best with values of $\alpha \approx 0.5 - 0.6$ [44, 45], but no comparison with the first version of Eq. (4.4) was done. It is difficult to distinguish between both versions of the width law because the number of bands is limited and the widths w_n of the bands are small compared to their positions x_n. Theoretical works prefer the second version with $\alpha = 1$ [76, 164, 60]. In Sect. 4.4.5 the different versions will be tested on our results of lattice-gas simulations. We will also propose an alternative, theoretically well grounded approach unifying both versions there.

The time law (4.1) is a simple consequence of a diffusion process. The position $x_f(t)$ of the reaction front between A and B moves proportional to $\sqrt{t}$ with a prefactor that depends on a_0 and b_0 [50]. The other three laws cannot be explained so easily; one needs models describing nucleation and growth of the bands. These models can be categorized into two types. The first type is based on diffusion and reaction dynamics plus some thresholds which account for nucleation and growth. There exists a wide range of modifications. The second type of models uses well established phase separation techniques to explain the pattern formation based on spinodal decompositions [12] or a kinetic Ising model [11]. All of these models will be reviewed in the next section.

4.3. Models

4.3.1. Overview and recent trends

Reaction-diffusion models with thresholds are the oldest models describing Liesegang pattern formation. Only a few month after the first experiments by Liesegang, Ostwald gave a possible explanation of the pattern formation process on the basis of supersaturating liquids [160]. He suggested that the precipitation is not a result of a balanced reaction but must happen spontaneously when the concentration product K of the reactive partners reaches a critical concentration K_{sp}. The precipitation grows until K falls under a second concentration K_p. Both thresholds set the stage for several models differing in the detailed description of the reaction process. In principle they all follow a reaction scenario

$$A + B \to \cdots C \cdots \to D, \tag{4.5}$$

and differ in the way the intermediate stage $\cdots C \cdots$ and the precipitation $\to D$ are described. For the concentrations of the different chemical agents $A, B, \ldots$ the symbols $a, b, \ldots$ will be used in the following.

The empirical laws described in the previous section became the basis for the theoretical work which started in the fifties. First analytical descriptions [210, 163, 221] showed that the patterns can be explained by diffusion and reaction processes with a moving reaction front. When numerical simulation became feasible about 90 years after the first experiments it was possible to reproduce patterns dynamically by studying the reaction-diffusion equations [133, 55]. The fact that a novel approach was introduced in 1999 [164, 12] shows that the Liesegang pattern phenomena are still an active research field in both, experiment and theory.

Apart from the novel simulation approach the trends in the literature follow two general lines. The first line works on an analytical description of the basic laws [60, 13, 130, 131] or even looks for more general laws [96]. The second line varies the initial conditions and the geometrical configurations of the setup to understand the phenomena better and to find ways for applying the pattern formation in interesting engineering problems. Alternative geometries [95] and complex 3d boundary conditions [23, 82, 189] have been studied experimentally. Variation of the reaction terms [43] and the nucleation thresholds [150], additional terms for a dissolution of the bands [199, 153], as well as open systems [125] and, last but not least, systems with an additional electric field [199, 124, 184, 22, 21] have been studied to vary the patterns. In recent work the motion of the reaction front is even detached from the phase separation, which might be initiated, e. g., by a temperature gradient [10]. One hopes to understand and control the pattern formation process such that bands with constant distance [150] or even arbitrary patterns can be designed [21].

Most of the theoretical work is based on an analytical study or numerical solution of differential equations. Since such equations are always based on the concentrations $a, b, \ldots$ of the reacting agents, they generally yield mean-field solutions. Although such mean-field solutions can reproduce the basic laws listed in the previous section they have two disadvantages. Firstly, they cannot account for the statistical character of the reactions. Hence, the influence of particle number fluctuations and thus the stability of the patterns cannot be investigated adequately. Although there are some ideas to include fluctuation by an additional noise term in mean-field models [23, 124], we think that models with intrinsically statistical character are more adequate. This is particularly true for mesoscopic and nanoscopic systems, where fluctuations become more important. First experiments on microscopic scales indicate that fluctuations might play an important role [148, 23, 82]. Secondly, the differential equations may not describe the microscopical structure of the bands. Chopard *et al.* [44, 45] proposed an alternative approach by taking the basic principles of the mean-field description and implementing them in a reactive lattice-gas simulation. Such simulations can be very helpful in reconciling mean-field predictions with experimental data, as we will see in Sect. 4.4. A similar approach seems also possible using Ising models [11].

In the following sections, the mentioned quantitative models and simulations will be reviewed, except for the lattice-gas simulations to be presented in Sect. 4.4.

4.3.2. Ion product saturation models

In the first and easiest quantitative models for Liesegang pattern formation, the ion product models, the precipitation takes place without an intermediate stage; i. e., there is no C stage in (4.5) [210, 163, 221]. Like in the Ostwald model, nucleation $A + B \rightarrow D$ occurs when the local product concentration $K = ab$ reaches the threshold K_{sp}. The precipitates of D will grow and deplete their surrounding of A and B. As the reaction front proceeds, the product concentration around the immobile precipitate decays until growth becomes impossible. Wagner [210], Prager [163] and Zeldovich *et al.* [221] could show that these ingredients yield patterns which obey the time law (4.1) and spacing law (4.2). The diffusion profiles of a and b are described by a system of coupled integro-differential equations with given boundary conditions. These equations can be rewritten in a more convenient way, if local coordinates are introduced in the form $\lambda_n = x_n/(2\sqrt{Dt_n})$ and $\gamma_n = x_n/x_{n-1}$. Taking $n \rightarrow \infty$ and $x_0 \rightarrow 0$ renders the equations mathematically solvable. The local coordinates $\lambda_n \rightarrow \lambda$ and $\gamma_n \rightarrow \gamma$ yield the time law and the spacing law, respectively. However, since these laws were the result of a continuous limit, the dynamics of the process was lost. Furthermore, the formation of the Liesegang bands was taken for granted and not proved by solving reaction-diffusion equations.

The first dynamical version of the ion product model proposed by Ross *et al.* [133] was deduced from the elementary chemical reaction $A + B \rightarrow D$ and solved numerically. Besides the typical diffusion terms for A and B,

$$\begin{aligned} \partial_t a &= D_A \partial_x^2 a - R \quad \text{and} &\quad (4.6)\\ \partial_t b &= D_B \partial_x^2 b - R &\quad (4.7) \end{aligned}$$

with diffusivities D_A and D_B, respectively, the equations include a reaction rate R constructed for a specific experimental configuration. In principle, R mimics an auto-catalytic growth process with a growth rate proportional to an increasing function of the supersaturation $S = (ab/K_{sp}) - 1$. The authors tested different power laws and exponential functions and observed pattern formation for a very quickly growing function $R(S)$ only. Beside the confirmation of the time law no quantitative observations of the other laws were reported.

Later Zrinyi *et al.* [28] pointed out that no detailed description of the agent transport is needed, since precipitation takes place on a faster time scale. It is thus possible to model the growth process by a given critical threshold K_p. The corresponding source term for additional D can be written as a Heaviside step function, $c_1(a, b, d)\, \Theta(ab - K_p)$. The growth starts when the product concentration exceeds a second threshold $K_{sp} > K_p$, where the rate is independent of d. The partial differential equation for the precipitate concentration d can thus be written as [28] [2],

$$R = \partial_t d = c_1(a, b, d)\, \Theta(ab - K_p) + c_2 \Theta(ab - K_{sp}), \quad (4.8)$$

where c_1 and c_2 are model-dependent functions of the parameters (initial concentrations and diffusion coefficients), and c_1 also depends on a, b and d. Liesegang patterns observed in a wide range of systems can be modelled this way. In particular, it was possible to show that the time law and the spacing law hold for a large set of parameters [28]. The Matalon-Packter law was confirmed only if the initial concentration of the outer electrolyte a_0 is sufficiently large. However, p was shown to stay a monotonously decreasing function of a_0 even if a_0 is small. Furthermore, p increases monotonously with K_{sp} in a non-linear way, and it is anti-proportional to the diffusivity D_A of the outer electrolyte. The results for a specific p do not depend on the individual parameters but on ratios of parameters with equal dimension – a simple consequence of the mean-field character of Eqs. (4.6) to (4.8). The findings are consistent with an experimental categorisation of the patterns by the product and the difference of the initial concentrations [154]. The width law, however, was not investigated.

---

[2] In the original paper the second term was not introduced as a formula but described in the text.

In closely related approaches, growth was modelled proportional to the concentration of the precipitate, corresponding to $K_p = 0$ and $c_1 \propto d$ in Eq. (4.8) [13, 130, 131]. Focusing on the Matalon-Packter law (4.3), Antal *et al.* found that F is constant and $G \propto \sqrt{D_B/D_A}\, K_{sp}/b_0^2$ [13]. This result was achieved analytically based on the assumption $b_0 \ll a_0$; hence the failure of the Matalon-Packter law for low a_0 could not be observed. This result is inconsistent with $p \propto 1/D_A$ in [28], due to different assumptions for c_1 and c_2. Lebedeva *et al.* searched for a criterion for the pattern formation [130, 131], finding $\Phi = K_{sp}k_2D_B/u^2(t) > 2 + \sqrt{5}$, with k_2 the growth rate and $u(t)$ the velocity of the front (decreasing with time). Patterns are thus formed when the nucleation threshold K_{sp} is high and the growth rate k_2 is large. The time dependence of $u(t)$ explains why patterns do not start at $x_0 = 0$ but an empty ("plug") zone exists at the edge. The first two results match with those of Ross *et al.* [133] and Zrinyi *et al.* [28], who did not study the velocity of the reaction front.

4.3.3. Nucleation and growth models

The next models with slightly increased complexity separate the reaction-diffusion process $A + B \to C$ from the nucleation and growth process $C \to D$, introducing an intermediate state C, see Eq. (4.5). This, however, considerably simplifies the analysis. In the literature such models are often called nucleation and growth models because the formation of D depends on the nucleation and accumulation of C rather than on the product concentration of A and B.

This model was first introduced by Keller *et al.* [111] who analysed reaction-diffusion equations and confirmed the time law (4.1) and the spacing law (4.2). In contrast to Wagner and Prager [210, 163] they could calculate the positions x_n of the bands without a priori assuming band formation and stopping of the band growth. The first numerical solutions for a nucleation and growth model were presented by Dee [55]. He used a similar technique as Ross *et al.* [133] (see previous section) and determined the nucleation and growth criterion by classical nucleation theory. A detailed work concerning the nucleation and growth of silver particles similar to Dee was presented recently [102]. Since the reaction-diffusion process can be separated from the precipitation process, we will discuss the two stages separately.

First process: reaction-diffusion $A + B \to C$

The simple reaction-diffusion process $A + B \to C$ is important independently of Liesegang patterns since it is a basic process in many chemical reactions. To apply the results to the Liesegang pattern phenomena we will focus on a quasi-1d geometry where the reacting particles are separated at time $t_0 = 0$ with initial concentration a_0 and b_0. The concentration profiles $a(x,t)$ and $b(x,t)$ for $x \geq 0$ and $t > 0$ are determined by the reaction-diffusion equations (4.6) and (4.7) with the initial conditions $a(x,0) = a_0\Theta(-x)$, $b(x,0) = b_0\Theta(x)$ [3]. The reaction term R is again assumed to be proportional to the concentration product $K = ab$. Under these assumptions it is possible to calculate $a(x,t)$ and $b(x,t)$ as well as the reaction rate $R(x,t) \propto ab$ asymptotically

---

[3] For our problem we will need the additional boundary condition $a(0,t) = a_0$. The changes needed to achieve this will be introduced in Sect. 4.4.1

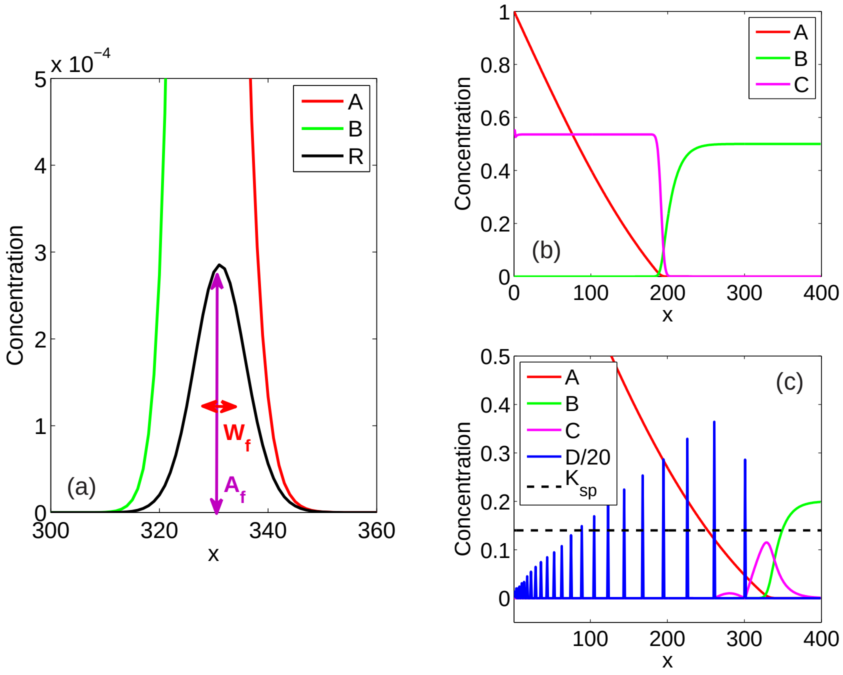

Figure 4.3.: (Colour online) illustration of the concentration profiles obtained in the reaction-diffusion process $A + B \to C$ without (a,b) and with (c) precipitation $C \to D$. The concentrations $a(x,t)$ (red) and $b(x,t)$ (green) are shown for fixed time t together with (a) the reaction rate $R(x,t) \propto ab$ (black) following Eq. (4.9), (b) the accumulated concentration $c(x,t)$ (magenta), and (c) the rescaled concentration of the precipitate D (blue). Note the constant value of $c(x,t) = c_0$ behind the reaction front in (b) according to Eq. (4.11). The dashed line in (c) indicates the threshold K_{sp}; the next band is started when $c(x,t)$ reaches K_{sp}.

for large times t [73],

$$R(x,t) \sim A_f \; S_R \left[\frac{x - x_f(t)}{w_f(t)} \right], \tag{4.9}$$

where S_R is approximately a Gaussian [12, 129]. The result is illustrated in Fig. 4.3(a). $R(x,t)$ describes the reaction front and reaches its maximum value at x_f which scales as $x_f(t) \sim \sqrt{t}$. The width of the front scales as $w_f(t) \sim t^\gamma$ with $\gamma = 1/6$. The production rate A_f of C at $x = x_f$ is proportional to $t^{-\zeta}$ with $\zeta = 2/3$. A scaling analysis regarding the impact of fluctuations [49] leads to the conclusion that the critical dimension, above which fluctuations become unimportant, is $d_c = 2$. In 2d logarithmic corrections apply and in 1d the whole dynamics change dramatically [49].

It is possible to approximate the effective diffusion coefficient D_f for the reaction front, i. e., the prefactor in $x_f = \sqrt{2D_f t}$ as well as the concentration c_0 of C behind the reaction front. This requires a few assumptions [118] which will be usually fulfilled in typical experimental setups. The reaction front $R(x,t)$ has to be confined in a region (reaction zone) $x_f(t) - w_f(t)/2 < x < x_f(t) + w_f(t)/2$ for all times t, disregarding all reactions outside this region. Then the concentration profile of each agent can be written as a solution of a diffusion equation [50]. Furthermore, Eqs. (4.6) and (4.7) must be approximated by a quasi-stationary solution in the region $-(D_A t)^{1/2} \ll x \ll (D_B t)^{1/2}$. Under these conditions the effective diffusion coefficient

D_f is given by an analytic implicit equation [118],

$$H\left(-\sqrt{\frac{D_f}{2D_A}}\right) = \frac{a_0\sqrt{D_A}}{b_0\sqrt{D_B}}\, H\left(\sqrt{\frac{D_f}{2D_B}}\right) \tag{4.10}$$

with $H(x) = [1-\mathrm{erf}(x)]\exp(x^2)$. Here, $\mathrm{erf}(x)$ is the Gaussian error function defined as $\mathrm{erf}(x) = \frac{2}{\sqrt{\pi}}\int_0^x \exp\left(-z^2\right) dz$. Evidently, the velocity of the reaction front does not depend on each of the initial concentrations, but on their ratio a_0/b_0, and it scales in the same way as D_A and D_B, since no characteristic time and length scales exist. The same approximation also yields that the concentration of C behind the reaction front is constant (see Fig. 4.3(b)), given by [13]

$$c_0 = \frac{b_0}{\pi}\sqrt{\frac{2D_B}{D_f}}\, H^{-1}\left(\sqrt{\frac{D_f}{2D_B}}\right). \tag{4.11}$$

The interesting point of these results, for the Liesegang pattern phenomena, is that only c_0 and D_f are essential parameters. Since both depend only on the initial concentrations and the diffusion coefficients, the band formation is independent of the reaction rate which is hard to measure. This does not imply, however, that the width of the bands or the specific concentration profiles are independent of the reaction rate.

Second process: Precipitation $C \to D$

Describing the $A + B \to C$ process exclusively by c_0, D_f, and the Gaussian reaction front (4.9), we now focus on the precipitation step. Like Ross *et al.* [133] (see Sect. 4.3.2), Dee [55] modelled the precipitation process using the classical droplet theory. Droz *et al.* [60] showed that Dee's approach can be simplified into

$$\partial_t d(x,t) = c_1 N[c(x,t), d(x,t)] + c_2\Theta[c(x,t) - K_{sp}] \qquad \text{with} \quad N(c,d) \propto d(x,t), \tag{4.12}$$

corresponding to Eq. (4.8) with $K_p = 0$ and c_1 and c_2 constants or proportional to c. A typical result of such a simulation is shwon in Fig. 4.3(c). Using this model, Dee confirmed the spacing law (4.2) and found the linear form of the width law (4.4). Due to limited computational resources he was restricted to one example with only six bands and obtained no information on the Matalon-Packter law (4.3).

In Eq. (4.12) the growth of the precipitates is restricted to the points of the nucleated particles, see also Fig. 4.3(c). To obtain bands with a macroscopic width w_n one would need nucleation at every point in w_n since no non-local term exist. Although no macroscopic width is reproduced in this model one sees that the hight of the bands, which can be interpreted as their mass or integrated particle number, seems to grow linearly. This is in agreement with a theoretical prediction which will be introduced in Sect. 4.4.5.

Alternatively it would be possible to allow non-local growth such that C can become D in a broader surrounding of an initial nucleation centre. A popular version of the non-local term is [23, 69]

$$N(c,d) = \Theta\left[\int_{x-dx}^{x+dx} d(x',t)\,dx'\right]\Theta[c(x,t) - K_p]. \tag{4.13}$$

In this case, a second threshold K_p is needed to stop the growth. This threshold is not needed in Eq. (4.12) because local growth stops if nucleation stops.

Quantitative mean-field predictions for p and the Matalon-Packter law

It is possible to calculate the functional dependence of p in the nucleation and growth model described above [13],

$$p = \frac{D_C}{D_f}\left[\frac{c_0}{K_{sp}} - 1 - \frac{D_C}{2D_f}\right]^{-1}. \tag{4.14}$$

This surprisingly simple analytical solution determines p from the basic parameters D_f and c_0 (from $A + B \to C$), D_C (for the diffusion of C), and the nucleation threshold K_{sp}. As expected for a mean-field solution, Eq. (4.14) depends only on dimensionless ratios of the parameters. The first term characterizes the velocity of C versus the velocity of the reaction front, representing a measure of how fast c_0 could be reached. If $D_f \ll D_C$, C will quickly leave the reaction front and diffuse away. In this case it takes longer to reach the desired threshold K_{sp}, and p becomes larger. The second term makes sure that no precipitation occurs if $K_{sp} > c_0$. If K_{sp} is close to c_0 it takes longer to reach K_{sp} and p is also large.

The structure of Eq. (4.14) will be similar if nucleation and growth is modelled somewhat differently. All mean-field solutions must scale, and patterns emerge only if $K_{sp} \leq c_0$. For this reason Eq. (4.14) can serve as reference to test further properties of Liesegang pattern formation. One of these properties is the Matalon-Packter law, which is clearly inconsistent with Eq. (4.14), since it does not scale linearly with $1/a_0$. However, Antal *et al.* [13] could show that the Matalon-Packter law is a special case of Eq. (4.14), if $b_0 \ll a_0$. Then $D_B \ll D_f$ and the Gaussian error function can be approximated by $\mathrm{erf}(x) \approx 1 - \exp(-x^2)\left(1 - \frac{1}{2x^2} - \ldots\right)/\sqrt{\pi x}$ [2]. Applying this to Eq. (4.11) we obtain $c_0 \approx b_0\,(1 + \frac{D_B}{D_f}) = b_0\,(1 + \frac{D_B}{D_A}\frac{D_A}{D_f})$. In the range $0.05 \leq b_0/a_0 \leq 0.1$ interesting for experiments, Antal *et al.* showed numerically that D_A/D_f is linear in a_0/b_0. This leads to $D_A/D_f \approx \nu_1 + \nu_2 b_0/a_0$, yielding an approximation for c_0,

$$c_0 = b_0\left(1 + \nu_1\frac{D_B}{D_A} + \nu_2\frac{D_B}{D_A}\frac{b_0}{a_0}\right), \tag{4.15}$$

with $1 + \nu_1\frac{D_B}{D_A}$ and $\nu_2\frac{D_B}{D_A}$ numbers of order one. Since $b_0/a_0 \ll 1$ it is possible to neglect the last term in Eq. (4.15). It is not possible to argue this way already in the linear approximation of D_A/D_f because the νs do not have the same magnitude. Inserting the approximation back into Eq. (4.14) we obtain

$$p = \frac{D_C K_{sp}\nu_1}{D_A(\sigma_1 b_0 - K_{sp})} + \frac{D_C K_{sp}\nu_2 b_0}{D_A(\sigma_1 - K_{sp})}\frac{b_0}{a_0} = F(b_0) + G(b_0)\frac{b_0}{a_0}, \tag{4.16}$$

which is in the form of Eq. (4.3). The assumptions needed to derive Eq. (4.16) will be correct for most macroscopic experiments. An important exception might be given by an experiment of nanoscale particles in glasses [148]. In that case a_0 and b_0 have the same magnitude, but D_B seems to be one order of magnitude larger than D_A. This leads to $c_0 \gg b_0$ in contradiction with Eq. (4.15). However, since only one experiment was carried out yet, we cannot see whether Eq. (4.14) holds.

The width law

The width law has been neglected in the discussion of Liesegang pattern formation for a long time because of difficulties in defining and measuring the width w_n of the bands consistently. To obtain a finite width in microscopical models one needs to introduce a non-local growth term and a second threshold as $N(c, d)$ from Eq. (4.13). On the other hand it is also possible to generate a width using Eq. (4.12) for macroscopic models, e. g. [55].

The first theoretical step in the direction of clarifying the law was done by Droz *et al.* [60] using a model based on Eq. (4.12). They showed that the total mass m_n of D material in the nth band is proportional to x_n. The concentration profile $d(x, t)$ for $t \gg t_{n+1}$ will be stationary and has a scaling function of the form, $d_n(x, t) = A_n d[(x - x_n)/w_n]$ for $x_n \leq x \leq x_n + w_n$, where the amplitude A_n could depend on n. It is thus possible to relate m_n with d_n by integration, $m_n = A_n \int_{x_n}^{x_n+w_n} d[(x - x_n)/w_n]\, dx = \gamma A_n w_n \propto x_n$, where γ is the substituted integral over d_n. Using the first version of Eq. (4.4), $w_n \sim x_n^{\alpha}$, this yields $A_n \sim x_n^{\beta}$ with $\alpha + \beta = 1$ [60]. The authors also discussed experiments, fitting the results with $0.9 < \alpha < 1$.

A more direct treatment was proposed by Racz [164]. Because the $A + B \to C$ process is independent of the $C \to D$ process the number of C particles produced in the first process is the same as the number of D particles ending up in the bands. The number of C particles can than be calculated using the assumption that the constant concentration c_0 behind the front is really reached. Later, C precipitates into bands of D with a high concentration d_h while the low concentration c_l of C remains between the bands. The particle conservation law yields $(x_{n+1} - x_n)c_0 = (x_{n+1} - x_n - w_n)c_l + w_n d_h$ leading to the width law in the form

$$w_n = p\frac{c_0 - c_l}{d_h - c_l}x_n \approx p\frac{c_0}{d_h}x_n, \tag{4.17}$$

since c_l is usually very small. If d_h varies with the band position as $d_h \sim x_n^{\beta}$ the width law takes again the form $w_n \sim x_n^{\alpha}$ with $\alpha + \beta = 1$.

4.3.4. Further reaction-diffusion models and comparison

For charged C particles it is possible to extend the nucleation and growth model such that nucleation only occurs if the concentration of the outer electrolyte A exceeds a third threshold K_a. Such models are known as induced sol coagulation models [182, 39, 53]. The additional threshold is motivated by the fact that the repulsive electrostatic interaction between the C ions can be screened by A particles. The model yields band formation significantly behind the reaction front as observed in some experiments [103]. The functional form of p deviates from Eq. (4.14) [13],

$$p = 2\frac{D_C}{D_f}\left\{\left[\frac{c_0}{K_{sp}}\left(1 - K_a/a_0\right)\right]^2 - \frac{D_C}{D_f}\right\}^{-1}. \tag{4.18}$$

A fourth category of models is called competitive growth models [75, 71, 68, 208, 40, 37, 121]. In these models, the precipitates D can dissolve with a probability decreasing with increasing size of the precipitates. In special cases it is possible that the bands move [223], dissolve and reprecipitate [199], such that the total number of bands leads to a chaotic time series.

It is possible to compare the F and G functions of the Matalon-Packter law (4.3) for the supersaturation models with thresholds discussed in Sects. 4.3.2 to 4.3.3 and Eq. (4.18). As already mentioned, the law is valid only for $b_0/a_0 \ll 1$ and $D_B/D_f \leq 1$. The ion product supersaturation model (see Sect. 4.3.2) predicts $F(b_0) \sim const$ and $G(b_0) \sim K_{sp}/b_0^2$, which is in contradiction to experimental results yielding monotonously decreasing functions of b_0 for F and G [143]. The nucleation and growth model predicts $F(b_0) \sim G(b_0) \sim K_{sp}/(\sigma b_0 - K_{sp}) \approx K_{sp}/b_0$ if $K_{sp} \ll b_0$. The induced sol coagulation model predicts $F(b_0) \sim K_{sp}^2/b_0^2$ and $G(b_0) \sim (\alpha/b_0^3 + \beta/b_0^2)$. In addition, Antal *et al.* [13] remark that a refined version of the sol coagulation model will converge to the nucleation and growth model in the limit $K_a/a_0 \to 0$. With such a model it should be possible to vary the functional dependence of F such that $F(b_0) \sim b_0^{-\gamma}$ with $1 \leq \gamma \leq 2$, corresponding to $0.2 \leq \gamma \leq 2.7$ observed in experiments, see [13] and references therein. Such refinement is only possible if the C particle are charged. For uncharged C particles the nucleation and growth model still yields the best predictions.

Comparing all four supersaturation models one can conclude that the nucleation and growth model serves best as a reference model. It is the easiest model yielding the Matalon-Packter law. Although it needs an intermediate state C, the model is actually most suitable for analytical and numerical studies. The sol coagulation model and the competitive growth models, on the other hand, can explain details observed in specific experimental setups, but they are not needed to explain the basic universal laws discussed in Sect. 4.2. The variety of models yielding these laws is remarkable. The same is true for the variety of physical, chemical and even geological systems showing the phenomenon. This fact suggests that a very general mechanism governs the pattern formation. Such a mechanism will be described in the next section.

4.3.5. The spinodal decomposition model with Cahn-Hilliard dynamics

Although the supersaturation models described in the previous sections account for most of the Liesegang phenomena, there are drawbacks. Firstly, the threshold parameters controlling the growth of the bands are difficult to grasp theoretically and not easy to control experimentally. Secondly, it is difficult to derive how the band formation could be manipulated in a desired way, since the structure of the models is too complicated. Furthermore, the specific models might seem insufficiently universal. Hence, a new approach free of thresholds and reaction-diffusion equations was recently suggested by Antal *et al.* [12]. They studied only the second process $C \to D$ of Eq. (4.5) applying the spinodal decomposition theory for phase separating processes [84, 56] to describe the phase separation into bands. We note that the distinction between C and D is actually not necessary here, since the bands correspond to areas with high concentration $c = d_h$, while there is little C between the bands, $c = c_l$ (see also Sect. 4.3.3). Although the model was introduced to describe $C \to D$ processes it is equally valid for processes where the C particles arrange in bands of high and low concentrations. Then the phase separation is assumed to take place at a very low effective temperature leading to stable bands after long times.

As we have seen in the Sect. 4.3.3 the production of C particles in the $A + B \to C$ reaction is well understood. The reaction front – an approximately Gaussian shaped region where C is produced at the rate $R(x,t)$ given by Eq. (4.9) – moves diffusively with its centre at $x_f(t) = \sqrt{2D_f t}$ and its width increasing as $w_f(t) \sim t^{1/6}$. Hence, the spinodal decomposition model can start with the C particles. Their dynamics are described by a simple phase separating equation taking particle conservation into account. The specific dynamics were introduced by Cahn and Hilliard [31, 30]. We note that an equivalent approach is the so-called model B in critical dynamics [92].

In the Cahn-Hilliard equation the concentration of C, c, is represented by the so-called 'magnetization'

$$m = c - (c_l + d_h)/2. \tag{4.19}$$

Then a Ginzburg-Landau-type free energy is defined in the simplest possible way required for obtaining two minima. This free energy, illustrated in Fig. 4.4, is finally inserted into the Cahn-Hilliard equation [164],

$$\partial_t m = -\lambda \partial_x^2 \left[\epsilon m - \gamma m^3 + \sigma \partial_x^2 m \right] + R(x,t), \tag{4.20}$$

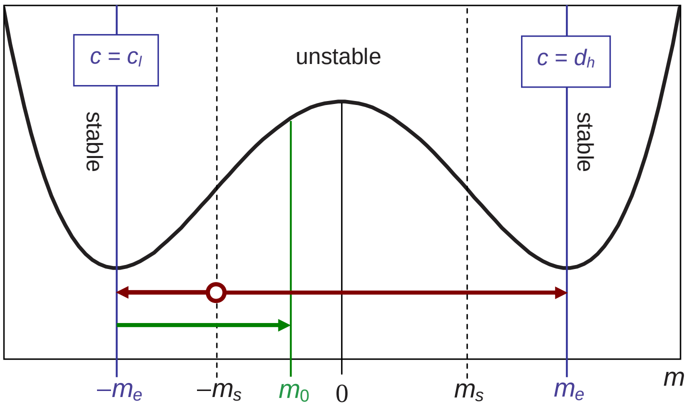

Figure 4.4.: (Colour online) illustration of the spinodal decomposition model. The homogeneous part of the free energy F is shown as a function of the 'magnetization' $m = c - (c_l + d_h)/2$. See text for detailed explanation.

Here, $R(x,t)$ is the source term introducing new C particles into the system via the $A + B \to C$ reaction. The parameters ϵ and γ have to satisfy $\sqrt{\epsilon/\gamma} = (d_h - c_l)/2$, while σ must be positive to eliminate short-wavelength instabilities. λ and σ can be used to set the time-scale and length-scale of the system, which leaves ϵ as the only free parameter. Since ϵ measures the negative deviation of the temperature T from the critical temperature T_c, $\epsilon > 0$ is needed for $T < T_c$. No phase separation occurs for $T > T_c$.

The model can be understood most easily by looking at the free energy sketched in Fig. 4.4. The source term $R(x,t)$ moves the system form $m = -m_e$ (for $c = c_l \approx 0$) over the spinodal point $-m_s$ to $m = m_0$ which corresponds to $c = c_0$. Choosing m_0 such that it is located in the unstable regime, the system will move to the second stable regime at $m = m_e$ corresponding to the high concentration $c = d_h$, i. e., band formation. The band becomes a sink for C, and its width grows until the front moves away so that m can decay below m_s, and the unstable regime is reached again, moving the system back to $m = -m_e$. Using this model it is possible to produce Liesegang patterns satisfying the spacing law (4.2) in agreement with the Matalon-Packter law (4.3) [164, 12, 59]. Due to the conservation of C particles the arguments regarding the width law presented in Sect. 4.3.3 also apply here. Actually, the derivation of the width law in Eq. (4.17) was introduced in the context of the spinodal decomposition model.

A special feature not observed in the threshold models is the low density phase with non-zero c, which has been reported in many experiments. The spinodal decomposition model can also be implemented for sophisticated conditions. For example, the effect of an additional electric field was discussed recently this way [22]. However, this can be done similarly using a threshold model [20].

4.3.6. The kinetic Ising model with Glauber and Kawasaki dynamics

An alternative way to model the phase separating dynamics was recently proposed by Magnin *et al.* [11] along the lines of the kinetic Ising model for ferromagnets. The main advantage is that this model fully describes the fluctuations, going beyond the mean-field approximations. Like in the spinodal decomposition model (see previous section), the concentration of C (and D) particles is represented as a magnetization. The particles are identified as spin-up sites in a cubic lattice, while spin-down sites represent vacancies. Then the formation of precipitates is modelled by a combination of spin-flip and spin-exchange dynamics [61]. The Hamiltonian is the usual nearest neighbour Ising Hamiltonian with ferromagnetic coupling $J > 0$ between the spins $\sigma_{\mathbf{r}}$ at site $\mathbf{r}$, modelling the attraction of the C particles,

$$H = -J \sum_{\text{neighbours } \mathbf{r},\mathbf{r}'} \sigma_{\mathbf{r}} \sigma_{\mathbf{r}'}. \tag{4.21}$$

Specifically, Glauber dynamics [80] are used to add the C particles in an initial state, in which all spins are down. The spin-flip rate $w_{\mathbf{r}}$ at site $\mathbf{r}$ is given by $w_r = R(\mathbf{r}, t)(1 - \sigma_{\mathbf{r}})/2$, with R the source term discussed in Sect. 4.3.3 (see Eq. (4.9)). Since the width $w_f(t) \sim t^{1/6}$ of the reaction front is not changing much, a constant width leaving behind a constant concentration c_0 of C particles was chosen [11]. The diffusion and interaction of the spin-up sites, i. e., of the particles, is modelled by a spin-exchange process with Kawasaki dynamics [109], $w_{\mathbf{r}\to\mathbf{r}'} = \left[1 + \exp\left(\delta E/(k_B T)\right)\right]^{-1} / \tau_e$. This exchange rate satisfies a detailed balance at temperature T. The flip frequency τ_e sets the time scale, T is the temperature, k_B the Boltzmann constant, and δE the energy change.

2d and 3d simulations have been reported for this model [11]. In 2d no pattern formation could be found for a wide range of parameters, in contradiction with previous work using lattice-gas simulations [44, 45]. In 3d patterns emerge in a restricted parameter range. Due to limited computational power no quantitative results for Liesegang patterns have been published yet and fluctuations have not been analysed, indicating that the model needs further investigation.

In the next section, we will thoroughly discuss lattice-gas simulations for Liesegang pattern formation, since these studies have already yielded quantitative results and fully include fluctuations.

4.4. Lattice-gas simulations

In the previous section, we have seen that several mean-field models can reproduce the basic laws of Liesegang pattern formation. However, there are problems not solved by mean-field models.

1. *Is the spacing law valid for all distances or only asymptotically?*
   While simple mean-field theories yield $x_n \propto (1+p)^n$ or equivalently $x_{n+1} = (1+p)x_n$, see Sect. 4.3.2, experimental works usually report an asymptotic behaviour $x_{n+1} \to (1+p)x_n$ for large n (Eq. (4.2)).

2. *Which version of the width law is the true one?*
   While the mean-field theories generally yield $w_n \propto x_n^\alpha$ (see Eq. (4.17)), experiments have been fitted successfully by both version of Eq. (4.4).

3. *Which deviations from the Matalon-Packter law (4.3) or its more general mean-field form (4.14) are relevant?*
   Although most experimental findings are consistent with the Matalon-Packter law (4.3), one can expect deviations if D_B is large or if fluctuations become important.

4. *How stable are Liesegang patterns forming under different conditions and in nanoscale systems?*
   Simple mean-field models assume the existance of quasi-periodic Liesegang patterns and thus cannot be used to study the stability of the pattern formation process. In general, mean-field quantities like concentrations are not well suited for studying nano-sized systems,

since the number of atoms of one agent in a given small volume may fluctuate significantly. These fluctuations can increase or decrease the stability of the Liesegang patterns.

5. *What Liesegang patterns can be expected under special, restricted (e. g., dimensionally reduced), or designed geometries?*
   This question is particularly important if self-organization of Liesegang patterns shall be applied to design nanoscale devices. However, mean-field models usually assume a quasi-1d geometry.

In this section we will address problems 1 to 3 by means of lattice-gas simulations. Problems 4 and 5 will be studied in later publications; we just briefly comment on them here.

Problem 4 can be addressed only by models that include the fluctuations of the particle numbers and thus go beyond the mean-field limit. Two major approaches in this direction have been published so far: the kinetic Ising spin simulation reviewed in Sect. 4.3.6 [11], and lattice-gas simulations on the basis of the nucleation and growth model by Chopard *et al.* [44, 45]. Since the Ising model approach is still not so far advanced, we chose the second approach here. An additional advantage is the existence of a corresponding mean-field model (see Sect. 4.3.3), that the results can be compared with to find out deviations in the universal laws and effects of fluctuations. Equations (4.14) and (4.17) represent the mean-field solutions for the spacing law and width law, respectively.

Problem 5 has already been addressed by Liesegang himself since the first experiments were in polar geometry. However, most theoretical work was done in quasi-1d geometry, and nobody investigated how geometry affects the pattern formation and the empirical laws. A first step towards new geometries was done in [23] using mean-field models plus a stochastic term. However, this ansatz seems to be hard to control for some special geometries. Therefore we think that the lattice-gas model can serve as a good candidate to test also new geometries and their influence on the pattern formation.

Lattice-gas simulations can serve as a computational experiment to test how the mean-field solutions can be applied to 'experimental' data and furthermore how fluctuations might cause deviations from these solutions. As suggested by the separation of the two processes in the nucleation and growth model, the lattice-gas simulation consists of two stages. In a first stage the C particles are generated (cf. Sect. 4.3.3). The second stage simulates the precipitation of the C particles by rules comparable with cellular automata (cf. Sect. 4.3.3).

4.4.1. First process: reaction-diffusion $A + B \to C$

In the simulation, we consider a simple cubic lattice of size $M \times M \times L$ with $L \gg M$, see Fig. 2(a). Each lattice site represents one cubicle (cell) of the system. Initially, the lattice is homogeneously filled with B particles, i. e., there are on average b_0 independent B particles on each site. The A particles are placed on the left plane of the lattice with a_0 particles on each of the $M \times M$ sites. The parameters a_0 and b_0 can thus be interpreted as concentrations per lattice site. Typically, b_0 is in between 10 and 200, while a_0 is about twice as large. The mean-field limit can be reached if either the considered cells are enlarged or the number of particles per cell is increased. Thus, increasing both a_0 and b_0 but keeping their ratio constant, drives the simulation to the mean-field limit.

The dynamics is modelled as follows. To simulate diffusion, both, A and B particles perform independent random walks on the lattice. The diffusities D_A and D_B are defined as the probabilities that a motion in either of the six possible directions takes place in a given time step [41, 115],

i. e., D_A and D_B are proportional to the physical diffusivities. After each time step, the left plane of the lattice is re-filled with A particles with the initial condition. A reaction $A + B \to C$ takes place with probability κ ($\kappa = 1$ in our simulations), if at least one A and one B particle is found on the same site [49, 42]. Afterwards, all C particles also diffuse independently on the lattice with diffusity D_C. It was previously shown that the mean-field predictions regarding the reaction rate $R(x, t)$ (reviewed in Sect. 4.3.3) are in agreement with the simulations in 3d [49], while logarithmic corrections occur in 2d [42].

Here, we use for the first time 3d lattice-gas simulations for Liesegang patterns in contrast to the 2d setup employed by Chopard *et al.* [44, 45]. For an alternative 3d simulation see Sect. 4.3.6 [11]. To confirm that the mean-field limit is reached for large concentrations, we ran simulations with different b_0 (keeping a_0/b_0 constant) and found that c_0/b_0 becomes constant in agreement with Eqs. (4.10) and (4.11). Figure 4.5(a) shows the simulated deviations from the mean-field limit, which decay below one percent for $b_0 \gg 2$. We focus on $b_0 > 10$, where the deviations are below 10^{-4}. In a 2d (or 1d) simulation, fluctuations would alter c_0 such that c_0/b_0 does not converge to the mean-field limit even for large b_0 and a_0 [42].

Since the mean-field solutions are valid for a 3d setup, it is possible to insert the C particles directly. This ansatz was first used in a kinetic Ising scenario [11] (see Sect. 4.3.6). We employ this idea to speed up our numerical calculations, since fully simulating the reaction-diffusion process $A + B \to C$ reduces the computational speed by at least one order of magnitude. Otherwise we could not work with concentrations $b_0 > 10$ in sensible time. However, this approximation reduces the fluctuations of C particle production, in particular for small concentrations.

The probability to insert C particles into the lattice is given by the reaction rate $R(x, t)$ (see Eq. (4.9)), with a centre position $x_f(t)$ moving as $x_f(t) = \sqrt{2D_f t}$ to the right. Usually, D_f is calculated via Eq. (4.10), assuming that the A particles are distributed homogeneously for $x \to -\infty$, i. e., $a(-\infty, t) = a_{-\infty}$. In this case the A particle concentration outside the quasi-stationary region (see Sect. 4.3.3) can be approximated by $a(x,t) = a_{-\infty} - a_f \left[\operatorname{erf}\left(\frac{x}{2\sqrt{D_A t}}\right) + 1\right]$ with a constant a_f. However, in our configuration, Eq. (4.10) needs to be modified, since the concentration of A particles is held constant for all times on the left plane, i. e., for $x = 0$: $a(0, t) = a_{-\infty} - a_f = a_0$. A straightforward derivation similar to the derivation of Eq. (4.10) in [118] leads to the solution

$$\operatorname{erf}\left(\sqrt{\frac{D_f}{2D_A}}\right) \exp\left(\frac{D_f}{2D_A}\right) = \frac{a_0\sqrt{D_A}}{b_0\sqrt{D_B}}\, H\left[\sqrt{\frac{D_f}{2D_B}}\right]. \tag{4.22}$$

Following [11] we approximate the nearly Gaussian-shaped reaction rate term $R(x, t)$ by

$$\tilde{R}(x,t) = \frac{\tilde{A}_f}{\sqrt{t}}\Theta(x - x_f + \Delta)\Theta(x_f + \Delta - x), \tag{4.23}$$

with constant width 2Δ of the front. These simplifications are justified since the band forming process does not depend on the exact form of the reaction zone [12] and the width of the front increases very slowly in time (as $t^{1/6}$, see Eq. (4.9)). The most important feature of the reaction front is that it leaves behind a constant concentration c_0 of C particles. Therefore, $\tilde{A}_f$ in Eq. (4.23) is chosen to be

$$\tilde{A}_f = \frac{\sqrt{2D_f}}{4\Delta} c_0. \tag{4.24}$$

Figure 4.5(b) compares the simulated c_0^{LG} with the c_0 value inserted into the simulation via Eq. (4.24). In contrast to a full simulation of the $A + B \to C$ reaction (see Fig. 4.5(a)), c_0^{LG}

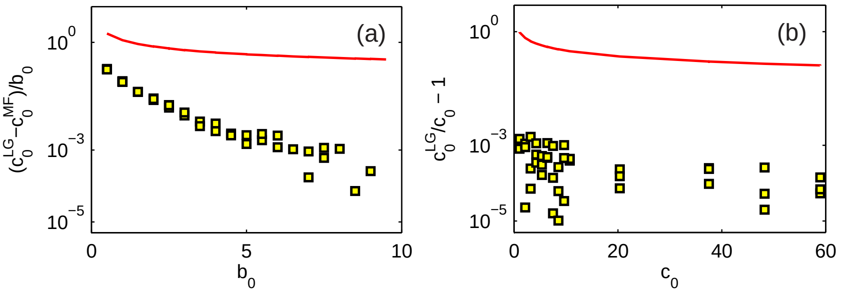

Figure 4.5.: (Colour online) (a) Deviations of the 3d lattice-gas simulations from the mean-field limit. The values of simulated ratios c_0^{LG}/b_0 have been calculated from the plateau of $c(x,t)$ observed behind the diffusion front (see Fig. 4.3(b)). The corresponding mean-field value c_0^{MF}/b_0 was calculated from Eq. (4.11). The red curve marks the (scaled) standard deviations of the particle numbers per lattice cell from their means c_0^{LG} indicating the fluctuations in the production of the C particles. The simulation parameters are $a_0/b_0 = 2$, $D_A = 1$, $D_B = 0.1$. (b) Results of our lattice-gas simulations with C particles inserted in an approximated reaction zone according to Eqs. (4.23) and (4.24). The values of simulated ratios c_0^{LG}/c_0 have been calculated as in (a). They are in good agreement with the inserted c_0 for all concentrations. Red curve same as for (a). The parameters are $D_f = 1.22$ (calculated from Eq. (4.22)) and $\Delta = 3$.

reaches the mean-field value already for small concentrations since the fluctuations induced by the motion of the A and B particles are eliminated. Only the standard deviation (red curve) of the number of particles per cell is similar as in Fig. 4.5(a), since the reaction front in (b) is an approximation of the reaction front in (a) and both cause the same fluctuations in C particle production.

4.4.2. Second process: Precipitation $C \to D$

The second part of our lattice-gas simulation is the precipitation of C particles, generating the immobile precipitate D. The nucleation of D depends only on $c(x,t)$, while the growth of D depends on both, $c(x,t)$ and $d(x,t)$, see also Sect. 4.3.3. In the particle picture of our lattice-gas simulation the density will be the number of particles divided by the considered cell volume. Here, this considered volume around a given lattice cell includes all neighbour cells, i. e., the 27 cells in a cube of $3 \times 3 \times 3$ cells. This definition sets the mean reaction distance.

Two thresholds are introduced. If the mean local concentration of C particles (in the 27 cells) exceeds a threshold K_{sp}, nucleation occurs. C particles in the vicinity of D particles precipitate already if their mean local concentration exceeds a threshold $K_p < K_{sp}$. C particles on top of D particles always precipitate, which makes the growth process fast enough to deplete a region of C particles. Without this option the growth process would not terminate, and no additional Liesegang bands could be formed. The resulting bands have distinct positions, which we will denote by x'_n in the following; their width is denoted by w_n. We calculated x'_n as the centre of the bands, i. e., the mean of the positions of the first and last D particles within each band. The corresponding widths w_n are defined as the differences between these two positions.

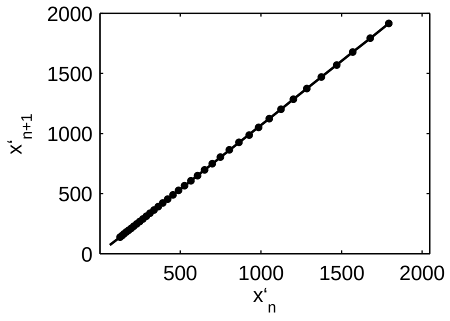

Figure 4.6.: Spacing law for simulated data depicted in a way different from Fig. 4.2(b), where x'_{n+1}/x'_n was plotted versus n to observe the asymptotical behaviour (cf. Eq. (4.26)). Here, x'_{n+1} is plotted versus x'_n to observe the linear behaviour with slope $1 + p$ and offset $p\xi$ (cf. Eq. (4.27)), yielding $p = 0.066$ and $\xi = 62$. Parameter set for the 3d lattice-gas simulation: $a_0 = 130$, $b_0 = 65$, $D_A = 1$, $D_B = 0.1$ (leading to $D_f = 1.22$ and $c_0/b_0 = 1.072$); $D_C = 0.1$, $K_{sp}/b_0 = 0.93$, and $K_p/b_0 = 0.52$.

4.4.3. Reconsideration of the spacing law

Equation (4.2), i. e., the asymptotical convergence of the ratio of the positions of neighbouring bands $x_{n+1}/x_n \to 1 + p$ for large n, was estimated from empirical findings; see Sect. 4.2. On the other hand, theoretical analyses suggest that the ratio x_{n+1}/x_n is identical with $1 + p$ [210, 163, 221, 111], as was discussed in Sects. 4.3.2 and 4.3.3. Although these two forms of the spacing law contradict each other, both are still used in parallel without much considerations. We propose a way to reconcile the experimental findings described by the empirical form of the spacing law with the theoretical mean-field prediction.

In experimental and numerical results the position of the first Liesegang band is usually blurred and thus not well defined, contrary to theoretical analyses. Thus, there is an arbitrariness in choosing the position of the first band. Therefore, it is better to use different variables x'_n for the experimentally or numerically measured band positions and x_n for the theoretical positions, since there may be an offset ξ between them,

$$x_n = x'_n + \xi, \tag{4.25}$$

due to, e. g., the blurred first band. Another possibility is that the mass of D in the first Liesegang band as well as the band's width cannot be close to zero as would be required if the linear increase observed in Fig. 4.3(c) was beginning at $x' = 0$. We will see later that usually $\xi > 0$, i. e., $x_n > x'_n$, indicating that the ideal laws are based on an 'imaginary' starting point outside the real sample. In literature, however, significant confusion is caused by the fact that both variables, x_n and x'_n, are not distinguished.

Studying measured values x'_n, and assuming both, $x'_n = x_n - \xi$ and the ideal mean-field result, $x_{n+1} = (1 + p)x_n$, one finds the asymptotic (empirical) form of the spacing law,

$$\frac{x'_{n+1}}{x'_n} = \frac{x_{n+1} - \xi}{x_n - \xi} = 1 + p\frac{x_n}{x_n - \xi} = 1 + p\frac{x'_n + \xi}{x'_n} = 1 + p + \frac{p\xi}{x'_n} \to (1 + p) \tag{4.26}$$

for large n as in Eq. (4.2). Figure 4.2(b) shows this asymptotic behaviour as observed in simulated data; note that actually the values of x'_n rather than x_n are plotted. The coefficient p is hard to determine in such plots, especially if only few bands are present. A more convenient way to

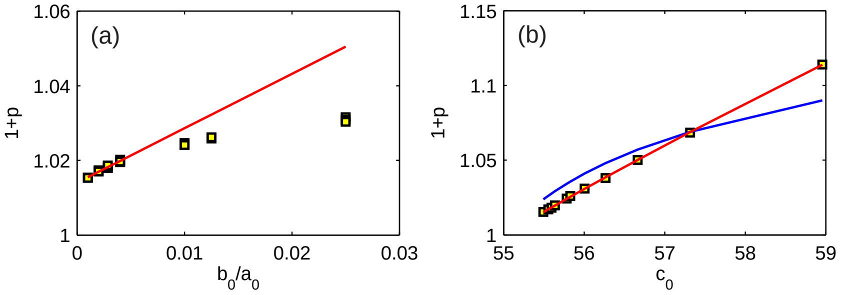

Figure 4.7.: (Colour online) reconsideration of the Matalon-Packter law based on 3d lattice-gas simulations. (a) The yellow squares indicate simulation results for the spacing law coefficient p obtained keeping b_0 constant and varying a_0. The straight line is a linear fit to the first four data points using Eq. (4.3). (b) Simulation results similar to those shown in (a). D_f and c_0 are calculated using Eqs. (4.22) and (4.11), respectively. The blue curve is a fit of Eq. (4.14), while the red curve takes fluctuations into account. Parameters: $b_0 = 55$, $D_A = 1$, $D_B = 0.1$, $D_C = 0.15$, $K_{sp}/b_0 = 0.96$, and $K_p/b_0 = 0.52$.

extract p from measured data is to fit the equation

$$x'_{n+1} = (1+p)x'_n + p\xi, \tag{4.27}$$

where $p\xi$ is the intersection with the ordinate, as shown in Fig. 4.6 for the same data. Even for a small number of bands, p and ξ can be extracted conveniently. In addition, we believe that the offset ξ is an important ingredient that should not be neglected in interpreting any experimental or simulated data. However, it remains unclear if or how the value of ξ could be predicted.

4.4.4. Reconsideration of the Matalon-Packter law

The original Matalon-Packter law (4.3) predicts a linear dependence between b_0/a_0 and p. It was shown in Sect. 4.3.3 that this empirical law holds for $b_0 \ll a_0$ only. In addition, a more general law was presented in Eq. (4.14) [13]. The deviations from Eq. (4.3) are even stronger in the results of lattice-gas simulations. An example is depicted in Fig. 4.7(a). A linear dependence is observed only for $a_0/b_0 > 250$, a criterion shown to be equivalent to $D_B/D_f \approx 1$ [13]. If a_0 is reduced for constant b_0, D_f increases, driving the system out of the regime in which Eq. (4.3) is valid [13]. Our lattice-gas simulations confirms these results, see Fig. 4.7(a).

Figure 4.7(b) compares a fit of the generalized Matalon-Packter law Eq. (4.14) (blue curve) with the results of our lattice-gas simulations. The deviations are still quite large. Only if fluctuations are taken into account by further modifying the generalized Matalon-Packter law, a nice agreement can be reached. The formula used for the red fit in Fig. 4.7(b) will be discussed and motivated in detail in a later publication.

4.4.5. Reconsideration of the width law

As discussed in Sect. 4.2 two competing empirical forms of the width law are used for fitting experimental data,

$$w_n = \mu_1 x_n + \mu_2 \qquad \text{and} \qquad w_n \propto x_n^{\alpha}. \tag{4.4}$$

Figure 4.8 shows the results of our lattice-gas simulations in both representations, because w_n is plotted versus x'_n both linearly and double logarithmically. Clearly, it is not possible to favour

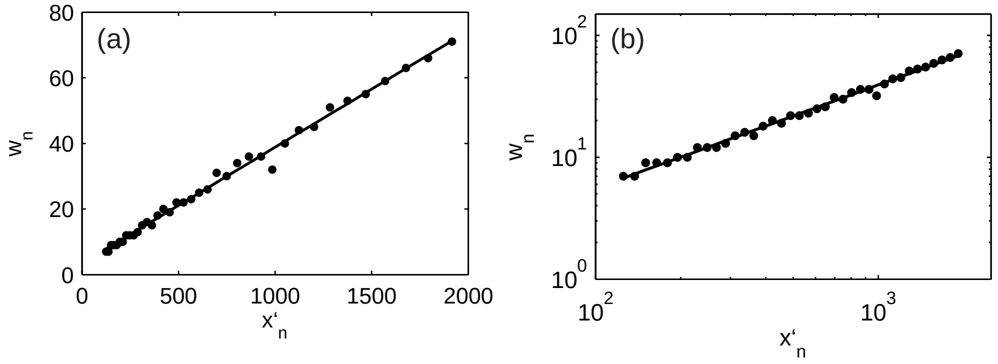

Figure 4.8.: Reconsideration of the width law based on 3d lattice-gas simulations. (a) Linear presentation of w_n versus x'_n (points) together with a fit of the first version of Eq. (4.4) with $\mu_1 = 0.035$ and $\mu_2 = 3.4$. (b) Double logarithmic presentation of the same data together with a fit of the second version of Eq. (4.4) with slope $\alpha = 0.82$. The same simulation as for Figs. 4.2 and 4.6 was used.

either of the two forms of the width law, since all widths are small compared with the size of the sample and both fits have an equivalent quality.

On the other hand, in Sect. 4.3.3 a simple and general width law was deduced theoretically (see Eq. (4.17)) using particle conservation. Assuming scaling behaviour of the band densities d_n, $d_n \propto x_n^\beta$, and setting $c_l = 0$ (since no precipitate occurs between the bands in our simulation), one obtains

$$w_n = p\frac{c_0}{d_n}x_n \propto x_n^\alpha \tag{4.28}$$

with $\alpha = 1-\beta$. This law was derived using the theoretical x_n where the ratio for two consecutive bands is constant, i. e., the exact form of the spacing law. A width law valid for experimental or numerical data of the positions x'_n of the bands can be derived introducing the offset ξ, see Eq. (4.25). The analytical form of the width law thus becomes

$$w_n = p\frac{c_0}{d_n}(x'_n + \xi) = p\frac{c_0}{d_n}x'_n + \frac{c_0}{d_n}p\xi, \tag{4.29}$$

which is in between the two competing empirical forms (4.4), since $d_n \propto (x'_n + \xi)^\beta$. Note that $p\xi$ is identical with the offset of the fit for the spacing law (4.27). Hence, the parameter ξ is also important for understanding the width law.

To test these predictions we have run simulations and fitted Eq. (4.28) to extract α from the data disregarding ξ, i. e., inserting x'_n directly for x_n. The results are shown in Fig. 4.9(a), yellow points. In a second approach we used the same data and inserted $x_n = x'_n + \xi$ into Eq. (4.28), also obtaining α as a fit parameter. The results are shown in Fig. 4.9(a), red points. Both approaches lead to different values of α indicating that the offset ξ plays a significant role.

Since the width law depends on the density of the bands d_n, it is not possible to distinguish the correct form by just looking at the width exponent α. Therefore, we have also calculated the densities d_n in the numerical simulations. Figure 4.9(b) shows the exponent β obtained by fitting $d_n \propto {x'_n}^\beta$ (yellow points) and $d_n \propto (x'_n+\xi)^\beta$ (red points). In addition, Fig. 4.9(c) depicts the sum of both exponents from parts (a) and (b), $\alpha+\beta$. The product $w_n d_n$ can be interpreted as the mass m_n of band n; it scales as $m_n = pc_0 x_n = pc_0 x'_n + pc_0\xi$ according to Eq. (4.29). Thus, according to theory, the mass exponent $\alpha+\beta$ must be one. The results shown in Fig. 4.9(c) indicate that this holds only in the case where the offset ξ is taken into account correctly (red points), confirming that ξ must not be disregarded.

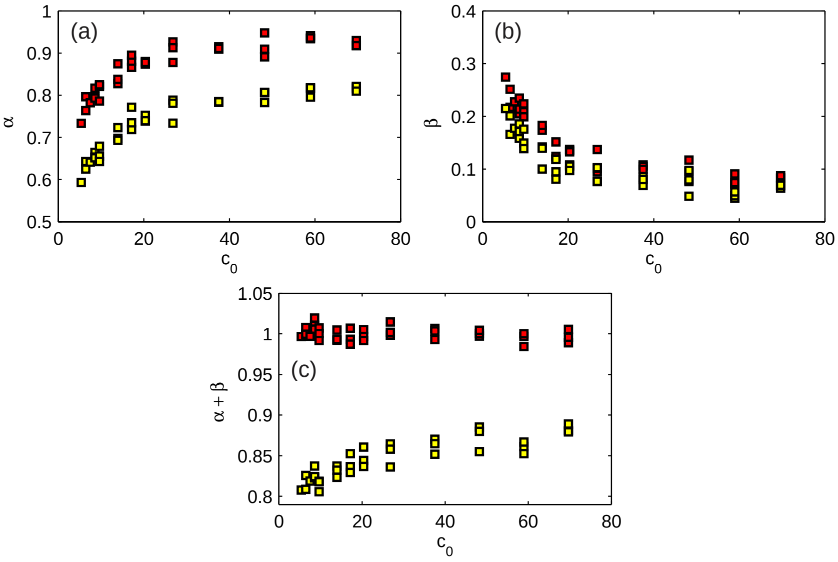

Figure 4.9.: (Colour online) fits of (a) width, (b) density, and (c) mass scaling behaviour based on our 3d lattice-gas simulations for different values of c_0. The exponents have been obtained by fitting a power-law to plots of (a) w_n, (b) d_n, and (c) $m_n = d_n w_n$ versus x'_n (yellow dots) and versus $x'_n + \xi$ (red dots). The parameters of the simulations are identical with those used for Figs. 4.2 and 4.6, except for varied c_0.

4.4.6. Application to previous experimental data

We believe that much confusion in literature could be avoided if the difference between x_n and x'_n was taken into account. In particular, the long-standing discussion about the width law could probably be solved if the analysis of experimental data included plots versus $x_n = x'_n + \xi$. We suggest that former experiments should be re-analysed using ξ and x'_n to confirm our conclusions.

An experiment which confirms the result of Eq. (4.29) was published recently [156]. The authors investigated pattern formation in a κ-Carrageenan gel. They measured x'_n and w_n for different concentration of the outer solution. First they plotted x'_{n+1} versus x'_n in a fashion similar to Fig. 4.6 and extracted p. Looking at the plot, we can clearly see offsets corresponding to $p\xi$. Secondly they plotted w_n versus x'_n in a linear fashion similar to Fig. 4.8(a), extracting the parameter $\mu_1 = pc_0/d_n$ in Eq. (4.29), assuming constant densities d_n. Looking at the plot, we also clearly see offsets corresponding to $\mu_2 = p\xi c_0/d_n$ (according to Eq. (4.29)). In addition they determined $c_0/d_n = 0.53$. This means that the offsets of the width law must be approximately half of the offsets of the spacing law. This conclusion is in quantitative agreement with the offsets we read from the plots in [156]. The experimental data thus confirm our conclusion that the offset ξ should be taken into account.

The differences of Eqs. (4.17) and (4.29) explain the different approaches used in experiment and theory. In summary, we have solved problems 1 and 2 raised in the beginning of Sect. 4.4; problem 3 was discussed in Sect. 4.4.4.

4.5. Summary and outlook

In this paper we reviewed the four empirical laws believed to govern Liesegang pattern formation and several important mean-field models reproducing these laws as well as a few Monte-Carlo-type simulations. Based on our detailed 3d lattice-gas simulations of the nucleation and growth model, we detected three major problems in reconciling the experimental reports with mean-field results. However, our simulations also helped us to find a straightforward solution.

We have shown that all basic empirical laws describing Liesegang pattern formation, i. e., the time law, the spacing law, the Matalon-Packter law, and the width law can be understood on the basis of the nucleation and growth model. A full agreement between experimental observations, simulation results, and mean-field models can be obtained only if a constant offset ξ between measured and theoretically assumed band positions is taken into account, as suggested in this work. A re-analysis of a previous experiment concerning the spacing law and the width law confirmed our suggestion. We propose that further experiments should be re-analysed to test the refined predictions.

In addition, we suggest further experiments with systematically varied concentrations of both, inner and outer electrolyte to confirm or extend the generalized Matalon-Packter law (4.14). Our current work in progress regarding the effects of fluctuations on Liesegang pattern formation indicates that additional modifications of the Matalon-Packter law are necessary in small-scale systems. Reliable experimental results for the nanoscale regime, where fluctuations are definitely important, are expected to become available soon, since experiments with nanoscale particles get feasible. A big open question will be how to manipulate the pattern formation such that interesting nanoscale devices could be designed. A deeper understanding of the dynamics is important for reaching this goal. For first promising works in this direction, see [150, 21, 10].

Acknowledgements: We thank I. Bena, M. Droz, M. Dubiel, I. L'Heureux, Y. Kaganovskii, I. Lagzi, K. Martens, and M. Rosenbluh for discussions. We would like to acknowledge support of this work from the Deutsche Forschungsgemeinschaft (DFG, project B16 in SFB 418).

5. Consequences of fluctuations in Liesegang pattern formation

Journal: EPL **84**, 48006 (2008)

Authors: L. Jahnke and J. W. Kantelhardt
Institute: Institute of Physics, Theory group, Martin-Luther-Universität Halle-Wittenberg, 06099 Halle, Germany

Abstract: Using lattice-gas simulations we show that Liesegang pattern formation in reaction-diffusion systems on small length scales can be described by a mean-field model, supplemented with three first-order corrections. We find that fluctuations due to thermal motion of the particles and due to impurities in the sample increase the number of Liesegang bands or even initiate patterns not forming without fluctuations. I.e., noise enhances or even induces ordering. Therefore, we suggest that it is possible to tune the number or distance of Liesegang bands by changing the impurities in the sample. Moreover, it might be possible to measure the nucleation threshold when changing the level of impurities in a micro- or nano-scale experimental setting.

5.1. Introduction

Pattern formation via reaction-diffusion processes can be observed in many fields of science [15] and in a wide range of length scales [82]. The dynamics is often complicated [51] but sometimes purely diffusive [107] or noise induced [181]. While some aspects can be described and understood with analytically or numerically solvable mean-field models, other phenomena require microscopic modelling approaches.

The pioneering papers on pattern formation in reaction-diffusion processes were published by Liesegang [134] and Turing [205]. Most experimental [36] and theoretical [51, 141, 128] work concentrated on the understanding of Turing patterns, which can be described by coupled reaction-diffusion equations. Liesegang patterns (i.e., bands or rings), on the other hand, emerge when diffusive motion is coupled with a fast nucleation process described by a highly nonlinear term [55, 130, 131].

For more than hundred years, Liesegang patterns have been studied experimentally [134, 143, 161, 14, 77, 85, 148, 78, 204, 82, 23, 156]. In contrast to Turing patterns one finds regular structures described by three well-defined rules concerning the spatial position x_n, the formation time t_n, and the width w_n of the nth Liesegang band (see [98] for a recent review):

- time law: $x_n \propto \sqrt{t_n}$ [152],
- spacing law: $x_{n+1} = (1+p)x_n$ [97],
- width law: $w_n \propto x_n^{\alpha}$ [103, 60, 55].

These laws have been derived in mean-field approaches based on (i) reaction-diffusion models with a threshold [55, 13, 130, 131] and (ii) phase-separating models with spinodal decomposition

[12, 164]. Here, we focus on the spacing law and study the dependence of p on parameters of the process. Since $p > 0$ in nearly all natural Liesegang patterns, the distance between neighbouring bands is increasing with depth and with band index – the picture characteristic of Liesegang patterns. Recently, however, suggestions for designing the x_n in a macroscopic system, i.e. changing the spacing law, have been obtained [10, 150, 21].

On the other hand, experiments could recently be scaled down to dimensions in the micrometer [204, 78, 23, 82] and nanometer regime [148]. On small scales the coarse grained structure of the sample and fluctuations induced by thermal motions of the particles or by impurities become important. Such effects cannot be studied in mean-field calculations. However, in none of the few microscopic simulations going beyond the mean-field limit [44, 45, 11] band formation was studied quantitatively and compared with the mean-field models. In this paper we show that lattice-gas simulation results for a nucleation and growth model with two thresholds can be fitted by mean-field predictions if the formula for the spacing-law coefficient p is supplemented with two correction terms.

The main focus of this paper is studying how fluctuations affect Liesegang pattern formation. It has already been known for years that fluctuations do not always destroy order but they can also enhance or initiate it [181]. Prominent examples are stochastic resonance [74, 217, 101] and catalysis [194]. Here we show that fluctuations in Liesegang pattern formation (i) increase the number of bands and (ii) can sometimes even initiate band formation. We find bands induced by fluctuations due to the thermal motion of the particles and by impurities, i.e. by heterogeneous nucleation. This effect could be used to control the number or distance of Liesegang bands. We propose that it is possible to measure the nucleation threshold by changing the level of impurities in a sample and fitting the spacing-law coefficient p with our extended mean-field formulas.

In the next parts of the paper we introduce the model and describe our lattice-gas simulation. Then we summarize the main results of the corresponding mean-field theory and discuss sources of fluctuations. The main parts of the paper are devoted to the discussion of the effects of fluctuations on the spacing law, studying (i) thermal motion and (ii) heterogeneous nucleation.

5.2. Nucleation and growth model for Liesegang pattern formation

Liesegang band (resp. ring) formation usually occurs when a first substance A is normally diffusing into a gel or a glassy material from a planar surface (resp. from central point). The second relevant substance B is initially homogeneously dissolved in the gel, which – contrary to a liquid – prevents flow or convection. At the diffusion front of A, where it meets B, a fast reaction $A+B \to C$ takes place, in which other (irrelevant) by-products might occur in addition to C. The final step is precipitation: C aggregates and creates immobile clusters denoted by D, which form the Liesegang bands. The details of the intermediate C stage might differ [98]. For Liesegang bands emerging in glass [148], for example, A is hydrogen, B are silver ions, C are Ag atoms or groups of 3-4 Ag atoms, and D are silver particles with sizes of several nanometers.

Most experimental and theoretical work as well as simulations focussed on the quasi-1d (one-dimensional) setup, in which A enters the sample from a planar surface, although Liesegang initially studied the polar geometry with A entering from the centre of a dish. The required parameters include the initial concentrations of A and B, denoted by a_0 and b_0, the diffusivities of all mobile agents, D_A, D_B, and D_C as well as parameters describing the reaction and the precipitation. Precipitation must involve highly non-linear terms to obtain Liesegang bands [55,

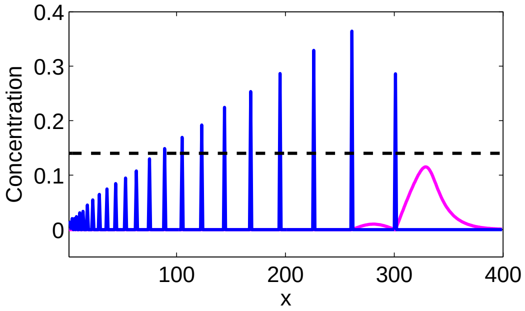

Figure 5.1.: (Colour online) Depiction of the nucleation process. The dashed black line is the nucleation threshold K_{sp}. The magenta line shows the concentration $c(x)$ of C particles generated at the reaction front (currently at $x \approx 350$, not shown). The blue lines are the bands of precipitate D, scaled down by a factor of 0.05.

130, 131]. For simplicity we focus on a model in which the reaction process ($A + B \rightarrow C$) can be separated from the nucleation and growth process ($C \rightarrow D$) [55, 13, 98].

The reaction process is controlled by diffusion and well understood (see [98] and references therein). Mean-field results with a critical dimension of two [49, 42, 118] show that the centre of the reaction front moves diffusively (position $x_f = \sqrt{2D_f t}$) into the sample with an effective diffusion coefficient D_f. The value of D_f can be calculated self-consistently from a_0, b_0, D_A, and D_B. Likewise, the asymptotic concentration of C particles behind the front, c_0, can be calculated analytically; it is approximately independent of the spatial position x [49, 42, 118, 98].

Due to the diffusion-limited character of the reaction process the precipitation will be fast compared with the diffusion time. All reactions occur instantaneously in our simulation with time steps chosen according to diffusional speed. Therefore a threshold K_{sp} for the concentration $c(x)$ of diffusing C particles is a good approximation to model the nucleation process. As depicted in fig. 5.1 nucleation occurs and a new band forms if $c(x)$ locally exceeds K_{sp}. The band will grow consuming $c(x)$ until the reaction front moved further to the right, allowing for sufficient C to be generated and a new band to be nucleated. In this simple nucleation and growth model, all band are infinitely narrow (see fig. 5.1). Bands with a finite width can be modelled by introducing an additional threshold $K_p < K_{sp}$, such that C particles in the vicinity of D particles already precipitate if their local concentration is above K_p.

5.3. Lattice-gas simulation

We have implemented a microscopic simulation of the nucleation and growth model based on a lattice-gas approach. We refer to [44, 45] for a first qualitative 2d implementation and to [98] for a more comprehensive description of our 3d implementation. Lattice-gas simulations use extended cellular automata; transport and reactions of the particles are governed by probabilistic terms. Transport is modelled by a random walk of each particle, and nucleation and growth are simulated by rules applied for each particle at each time step. Boundary conditions are implemented according to the geometry of the lattice. Alternative non mean-field approaches would be inserting a statistical term into the mean-field equations and solving these partial differential equations numerically [23] or Ising-type models [11].

Our simulations are run on a 3d simple cubic lattice of size $32 \times 32 \times 2048$. Although we cannot rule out finite-size effects (below ≈ 20 percent) in fitted spacing-law coefficients p for

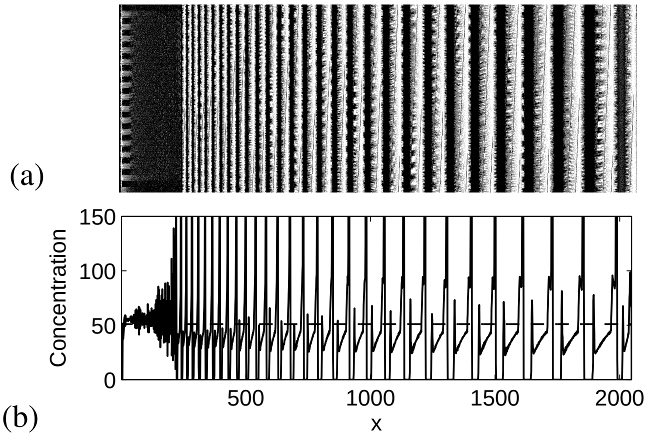

Figure 5.2.: Results of the lattice-gas simulation with $D_f = 1.22$, $c_0 = 58.96$, $D_C = 0.1$, $K_{sp} = 50.93$, and $K_p = 20.37$. (a) 2d presentation of the 3d patterns: all 32 slices (in z direction) are plotted next to each other vertically (in y direction). Grey dots represent remaining C particles and white dots represent the precipitated D particles. (b) 1d projection of the mean number of particles (in the y-z planes). The continuous line shows the concentration of D with peaks at both ends of each band due to the simulation rule of C always precipitating when reaching D. If this rule is abandoned, the peaks vanish but the simulations become much slower (since there remain many diffusing C particles). However, the patterns remain unchanged. The straight dashed line is the nucleation threshold K_{sp}.

this lattice size, we have checked that the functional dependencies of p on our parameters are not affected by them. Since the reaction $A + B \to C$ is well understood (see previous section), we simulate only the precipitation process, i.e., we start already with the C particles. The local rate of C particle generation is taken from the reaction zone profile following the mean-field solution [49, 42, 118, 11]. If the local concentration of C, averaged over the 27 lattice points in a local $3 \times 3 \times 3$ cube, exceeds the nucleation threshold K_{sp}, nucleation occurs and C becomes the immobile (not diffusing) D. This local averaging is needed since we neglect all short-distance interactions. Basically we introduce a small-scale mean-field ansatz. We anticipate that all chemical reactions occur inside a single lattice cell while all nucleation and growth reactions occur inside the extended box of 27 cells. These assumptions also set the length scales of our simulations. The clusters of D grow at the expense of C, as long as the local concentration of C plus D exceeds $K_p < K_{sp}$. In addition, C particles always turn into D when moving to a lattice point where there is already D. Using this simulation procedure we can obtain realistic Liesegang patterns with more than twenty bands, see fig. 5.2(a).

Altogether, there are five parameters in our simulation: the speed of the reaction front, D_f, and the limit concentration of C particles, c_0 (both of which can be calculated from a_0, b_0, D_A, and D_B [49, 42, 118]), the diffusivity D_C, the nucleation threshold K_{sp}, and the growth threshold K_p. A constant value of K_{sp} describes homogeneous nucleation. Later, we also consider spatially fluctuating values of K_{sp}, which models heterogeneous nucleation.

The main quantities needed to analyse Liesegang patterns are the positions x_n and the widths w_n of the bands (see fig. 5.2(b)). Then we determine the spacing-law coefficient p by a linear fit of $x_{n+1} = (1 + p)x_n + bp$ to the data; see [98] for a justification of the offset bp employed here. To check the stability of p we perform three independent simulations for each set of parameters.

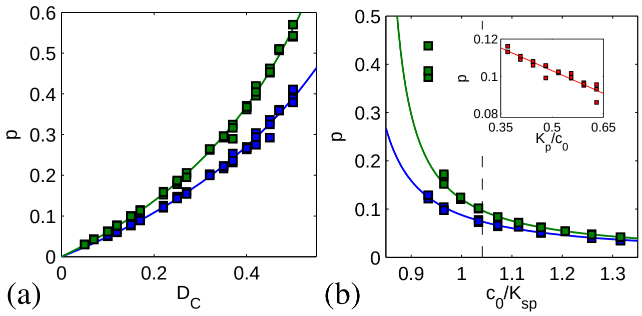

Figure 5.3.: (Colour online) Least square fits of eq. (5.1) (lines) to simulation results (squares) for the spacing-law coefficient p obtained varying D_C in (a) and K_{sp} in (b). Fixed parameters are $D_f = 1.22$, $c_0/K_p = 2.07$, and $c_0 = 26.8$ (blue points), $c_0 = 58.96$ (green points) as well as $c_0/K_{sp} = 1.16$ in (a) and $D_C = 0.1$ in (b). Fitted parameters are $F_1 = 0.32$ and $F_2 = 1.33$ (blue) and $F_1 = 0.3$ and $F_2 = 1.24$ (green). The dashed line in (b) marks $c_0/K_{sp} = 1 + D_C/2D_f$. Deviations from eq. (5.1) seem to occur for $c_0/K_{sp} < 0.95$; however, mean-field theory would not permit any pattern formation for $c_0/K_{sp} \leq 1$. Inset of (b): the red squares are simulation results for varied K_p with fixed $D_f = 1.22$, $K_{sp} = 18.52$, $c_0 = 21.44$, and $D_C = 0.2$; fitted by $F_1 = 1 - F_1' K_p/c_0$ (red line).

5.4. Corrections to the mean-field spacing law

The most common way to describe the spacing-law coefficient p is the Matalon-Packter law predicting a linear dependence of p on the ratio of the initial concentrations a_0 and b_0: $p = F(b_0) + G(b_0)b_0/a_0$ [143, 161]. However, this rule was shown to be just a special case (for $b_0 \ll a_0$ and $c_0 \approx b_0$ or $D_B \approx D_f$) of a more general law which was derived from a mean-field theory of the nucleation and growth model described above which only depends on the parameters of the nucleation and growth process [13, 98]. In the mean-field model, Liesegang bands will emerge only if the nucleation threshold K_{sp} is lower than c_0 and D_C is sufficiently small such that the value of p is positive.

In general, one can expect that p may depend on three dimension-less parameters, D_C/D_f, c_0/K_{sp}, and c_0/K_p. Since this mean-field model does not involve a growth threshold K_p, it describes bands with zero widths. Broad bands, however, have some excluded volume around their centres. The distances between them will thus be more similar with each other than for narrow bands, i.e. p is reduced. We thus suggest a first order correction with an additional dimension-less prefactor F_1 depending on c_0/K_p. In addition, we insert a second factor F_2 to take fluctuations (also disregarded in the mean-field model) into account; F_2 will be discussed in detail in the next section. With these two first-order corrections

$$p = F_1 \frac{D_C}{D_f} \left[F_2 \frac{c_0}{K_{sp}} - 1 - \frac{D_C}{2D_f} \right]^{-1} . \tag{5.1}$$

To test this corrected formula quantitatively we have run simulations varying D_C (see fig. 5.3(a)) and K_{sp} (see fig. 5.3(b)) but leaving all other parameters constant. The figures show that our data can be fitted very well by eq. (5.1) assuming constant values of F_1 and F_2. These results are the first numerical test of the $p\,(D_C/D_f, c_0/K_{sp})$ dependence by microscopic simulations. In addition, the inset in fig. 5.3(b) shows the dependence of p on K_p. We have fitted the data with $F_1 = 1 - F_1' K_p/c_0$, showing that K_p/c_0 enters linearly into the correction factor F_1 in first order approximation. Since the occurrence of F_1 is not a consequence of fluctuations we will not discuss it further here.

The dashed line in fig. 5.3(b) separates the region where mean-field solutions for pattern formation exists, $c_0/K_{sp} > 1+D_C/2D_f$, from the region without any mean-field patterns. However, due to the fluctuations in our microscopic simulation, we observe patterns also on the left hand side of the dashed line – the regime of ordered patterns is expanded. The area close to the dashed line is described very well by our first-order corrected formula (5.1) due to the correction factor F_2, but the approximation with fixed F_2 seems to fail for $c_0/K_{sp} < 0.95$. To understand the role of F_2 we now discuss in more detail the consequences of fluctuations.

5.5. Fluctuations due to thermal motion

The main focus of this paper is studying how fluctuations affect Liesegang pattern formation. The fluctuations in the production of C particles can be neglected in a 3d setting, since the critical dimension of the mean-field reaction-diffusion model is two [49, 42, 118]. We thus focus on the consequences of fluctuations in the nucleation process.

Nucleation occurs if the local concentration of C particles, c, exceeds the constant limit K_{sp}. The local value of c is defined by the number of C particles in a given lattice cell with volume V_c, divided by V_c. Since the number of particles fluctuates due to the diffusion process, c also fluctuates representing thermal noise. Without nucleation, the number of C particles in a given lattice cell is thus a binomially distributed integer variable, and its mean c_0V_c can be approximately associated with the standard deviation $\sqrt{c_0V_c}$. The mean-field limit is approached either by increasing the volume V_c of the lattice cells or by increasing the concentration c_0. In both cases, the standard deviation $\sqrt{c_0V_c}$ will eventually become negligible compared with the mean c_0V_c. We can thus check for the consequences of thermal noise by reducing c_0 and keeping both ratios c_0/K_{sp} and c_0/K_p as well as $V_c = 1$ constant in our microscopic simulations. Any deviations from a constant spacing-law coefficient p are then induced by thermal fluctuations.

Figure 5.4(a) shows that p is not constant, i.e. the mean-field result is clearly violated. In fact, this equation just describes the limit of very large concentrations c_0. For lower c_0 we observe smaller values of p, i.e. more bands with smaller and more similar spacings. In addition, fig. 5.4(b) shows that pattern formation with a specific p also occurs in the regime where there should be no pattern formation according to mean-field results. Clearly, the thermal noise leads to ordering, since the spacing-law coefficient p is reduced with decreasing c_0 and patterns occur even for $c_0 < K_{sp}$.

Next we want to fit quantitatively our data obtained studying a very wide range of c_0 values (mean numbers of C particles per lattice cell) ranging from 1 to 200 and also various parameter ratios c_0/K_{sp}, c_0/K_p, and D_C/D_f (see caption of fig. 5.4). To do this we must further elaborate the first-order corrected mean-field formula (5.1). If c_0 is reduced, keeping c_0/K_{sp} constant, the mean number of C particles in one lattice cell, c_0V_c, decreases proportional to c_0, but its fluctuations decrease proportional just to $\sqrt{c_0}$. In the case of low c_0 we can assume that – due to the thermal fluctuations – a reduced mean c_0 will already be sufficient for nucleations, since sometimes the actual concentration c will be c_0 plus some factor times $\sqrt{c_0}$. Thus, it is plausible that c_0 should be replaced by $c_0 + F_2'\sqrt{c_0}$ or, equivalently, $F_2 = 1 + F_2'/\sqrt{c_0}$ in eq. (5.1),

$$p = F_1 \frac{D_C}{D_f} \left[\left(1 + \frac{F_2'}{\sqrt{c_0}} \right) \frac{c_0}{K_{sp}} - 1 - \frac{D_C}{2D_f} \right]^{-1} . \tag{5.2}$$

The parameter F_2' indicates by how many standard deviations the nucleation threshold K_{sp} may exceed c_0 for band formation to continue happening.

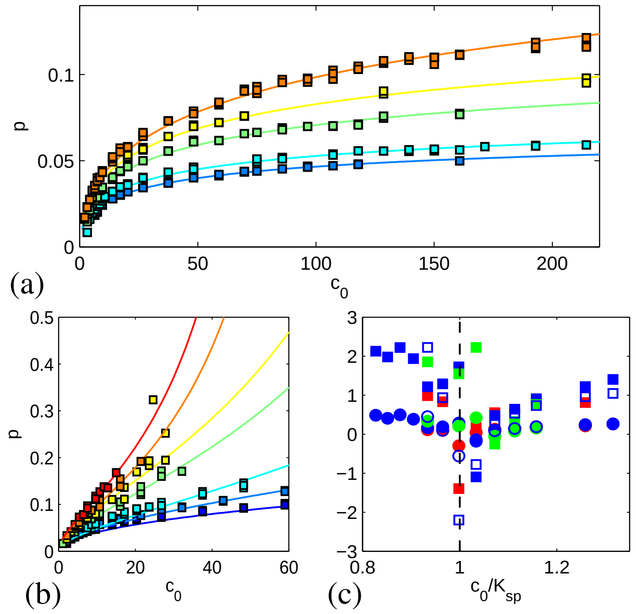

Figure 5.4.: (Colour online) Spacing-law coefficients p from simulations with constant ratios c_0/K_{sp} and c_0/K_p (symbols) fitted with eq. (5.2) (lines). (a) Regime of mean-field pattern formation, $c_0/K_{sp} > 1 + D_C/2D_f$, with (from bottom to top) $c_0/K_{sp} = 1.32$ (dark blue), 1.26 (light blue), 1.16 (green), 1.11 (yellow), and 1.07 (orange). (b) Regime of no pattern formation in mean-field, with (from bottom to top) $c_0/K_{sp} = 1.03$ (dark blue), 1 (medium blue), 0.96 (light blue), 0.90 (green), 0.88 (yellow), 0.85 (orange) 0.83 (red). Further parameters: $D_f = 1.22$, $D_C = 0.1$, $c_0/K_p = 2.07$. (c) Values of the fitting parameters F_1 (circles) and F_2' (squares) in eq. (5.2) for $c_0/K_p = 2.89$ (open symbols) and 2.07 (filled symbols), $D_f = 1.22$, and $D_C = 0.2$ (green), 0.1 (blue), and 0.05 (red) versus c_0/K_{sp}. The dashed line marks $K_{sp} = c_0$. We performed three Monte Carlo runs for each parameter set.

Equation (5.2) fits very well the data in both figs. 5.4(a) and (b). The fitted values for these and several additional simulations are summarized in fig. 5.4(c). The area to the right-hand side of the dashed line shows cases of pattern formation with a mean-field counter part, whereas the area on the left-hand side describes fluctuation induced patterns. Errors are smaller for the case $c_0 > K_{sp}$. Both F_1 and F_2' seem to have some dependence on K_{sp}, the dependence near $K_{sp} \approx c_0$ looks like a transition. However, since the region of possible K_p and K_{sp} values is limited in the simulation, it is not feasible to determine numerically the (second order) corrections to F_1 and F_2' with sufficient precision. An analytical approach beyond the scope of this paper would be needed.

5.6. Fluctuations due to heterogeneous nucleation

Up to now we have considered homogeneous samples with a constant nucleation threshold K_{sp}. However, in gels or glasses there are always defects, impurities or even free volume, and the nucleation of larger particles will probably be much easier in these locations. The consequences of such heterogeneous nucleation can be studied easily in our microscopic simulation, if the value of K_{sp} in each lattice point is considered as a fixed random variable. Here, we assume a normal distribution of K_{sp} with mean K_{sp}^{het} and standard deviation σ. This distribution of nucleation thresholds can be considered as a second source of fluctuations in the nucleation process.

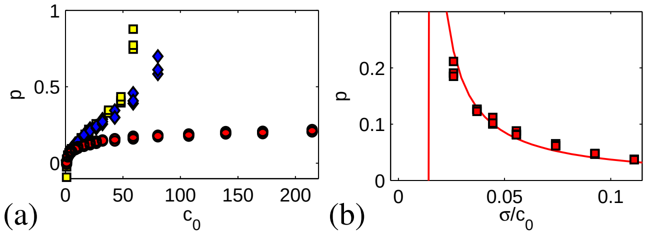

Figure 5.5.: (Colour online) Spacing-law coefficients p from simulations with heterogeneous nucleation. (a) p versus c_0 with fixed $c_0/K_{sp}^{het} = 0.93$ for homogeneous nucleation, $\sigma = 0$ (yellow squares), and for heterogeneous nucleation, $\sigma = 0.0185c_0$ (blue diamonds), and $\sigma = 0.0556c_0$ (red circles). (b) p versus σ/c_0 for $c_0 = 107.2$ fitted with eq. (5.3) (red line). Fit results: $F_1 = 1.82$, $F_2' = 1$, $F_2'' = 2.825$. There is no pattern formation for homogeneous nucleation or heterogeneous nucleation with $\sigma < 0.017c_0$ (vertical line) in this case. Further parameters: $D_f = 1.22$, $D_C = 0.1$, $c_0/K_p = 2.07$.

Figure 5.5(a) shows that heterogeneous nucleation further expands the regime of stable pattern formation. If the fluctuations σ of K_{sp} are small, Liesegang patterns occur just for small c_0, since there is no mean-field pattern formation as $c_0 < K_{sp}^{het}$. For large σ, on the other hand, we observe stable patterns up to very large c_0; i.e. the thermal noise is not needed to induce pattern formation. Clearly, fluctuations due to heterogeneous nucleation decrease the value of the spacing law coefficient p, leading to more ordered patterns, and induce pattern formation in regions where it would be impossible with mere homogeneous nucleation.

A quantitative description of the behaviour of p is possible again. Since the local nucleation criteria is $c > K_{sp}$, the consequences of heterogeneous nucleation are comparable with the consequences of fluctuations induced by thermal noise we described in eq. (5.2) taking variations of c_0 into account via $F_2 = 1 + F_2'/\sqrt{c_0}$. If σ is large, nucleation can occur already if c_0 is much smaller than K_{sp}^{het}. A second term proportional to the standard deviation divided by the mean, σ/K_{sp}^{het} (similar to the term $\sqrt{c_0 V_c}/(c_0 V_c)$ for homogeneous nucleation), must thus be added to F_2, leading to

$$p = F_1 \frac{D_C}{D_f} \left[\left(1 + \frac{F_2'}{\sqrt{c_0}} + \frac{F_2'' \sigma}{K_{sp}^{het}} \right) \frac{c_0}{K_{sp}^{het}} - 1 - \frac{D_C}{2D_f} \right]^{-1}. \tag{5.3}$$

Figure 5.5(b) confirms this formula by numerical simulations in the region $c_0 < K_{sp}^{het}$, where even thermal noise is not sufficient to induce pattern formation, if merely homogeneous nucleation occurs (at $\sigma = 0$).

If c_0 is large, the term $F_2'/\sqrt{c_0}$ in eq. (5.3) can be disregarded. Now, one can imagine an experimental setting in which the heterogeneity σ of the sample is known and can be varied, but the nucleation threshold K_{sp}^{het} is not known. By studying the patterns and the p values for different c_0, keeping σ constant, it will be possible to extract F_1 and $F_2/K_{sp}^{het} = (1 + F_2''\sigma/K_{sp}^{het})/K_{sp}^{het}$. Repeating this for different values of σ one can extract $1/K_{sp}^{het}$ as the intersection of F_2/K_{sp}^{het} with the ordinate. We think that this might be an interesting method to determine the nucleation threshold K_{sp}^{het} which is very hard to measure.

In general, fluctuations induced by heterogeneous nucleation reduce the spacing-law coefficient p and increase the number of Liesegang bands. It is thus possible to change the number or distance of bands without changing the properties or concentrations of the reactants involved in the pattern formation process. One only has to change the level of impurities or defects in a sample. In contrast to thermal fluctuations, such changes can be realized with spatial variations. We thus suggest that the spacing law can be modified by designing concentration profiles of impurities or defects in the sample. This might be realized by strong focussed laser irradiation of glass samples in an nano-scale Liesegang pattern formation experiment with silver particles [148]. This way, it might be possible to obtain equidistant band formation without interfering with the chemical reactions. Such designed Liesegang pattern formation could be used, for example, in optics, where the spacing and the widths of the bands directly affect absorption and scattering of light. It might become possible to produce different types of devices in the same chemical setting just by changing the type of glass or the levels of impurities or defects.

5.7. Summary and conclusion

We have microscopically simulated Liesegang pattern formation based on a nucleation and growth model with thresholds. The results show why experimental Liesegang patterns on very different length scales are so similar and can be described by the same fundamental rules. The reason is that fluctuations, irrespectively of their origin in either thermal motion of the particles or in impurities, defects or free volume in the sample, stabilize the pattern formation process. Contrary to intuition the patterns are not disturbed by fluctuations, but the regime of stable pattern formation is rather expanded. Consequently, the three major Liesegang rules, time law, spacing law, and width law, apply also in systems with large fluctuations, e.g. in experiments on micrometer and nanometer scales.

In addition, we have extended the mean-field formula for the spacing-law coefficient p with three first-order correction terms including the effects of (i) bands with non-zero width, (ii) fluctuations due to thermal motion of the particles on small scales, and (iii) fluctuations due to heterogeneous nucleation. We suggest that the formula can be used to fit experimental results and to confirm the consequences of fluctuations in Liesegang pattern formation. Besides, it might be used to extract the value of the nucleation threshold from experiments.

As a particularly attractive application of our results, we suggest that Liesegang pattern formation can be controlled by designing spatially varying concentrations of impurities or defects in the sample. This way the ordering effect of the fluctuations could be used to control the number or distance of Liesegang bands without interfering with the possibly delicate chemistry of the reaction and nucleation processes or with the diffusion processes. This approach seems to be complementary to recent suggestions [10, 150, 21].

Acknowledgements: We would like to acknowledge support from the Deutsche Forschungsgemeinschaft (DFG, project B16 in SFB 418).

6. Equidistant band formation of precipitation in a reaction-diffusion process

Journal: Submitted to New Journal of Physics
Authors: Lukas Jahnke and Jan W. Kantelhardt
Institute: Institute of Physics, Theory group, Martin-Luther-Universität Halle-Wittenberg, 06099 Halle, Germany
Abstract: We study precipitation patterns occurring in diffusion-limited chemical reactions, focusing on Liesegang bands. Naturally these patterns are non-equidistantly spaced and thus less useful for bottom-up material design. However, we show how a continuous large-scale modification of the inhomogeneity of the substrate and/or the nucleation threshold can be used to obtain equidistantly spaced bands on small length scales. We confirm our suggestions by lattice-gas simulations and propose an iterative experimental procedure not requiring a-priori knowledge of parameters.

Natural pattern formation can be found in many systems on various length scales [214] and with many shapes and types [15]. Besides the aesthetic appeal of the patterns, efforts are driven by the idea of designing devices in a *bottom-up* approach [82, 196, 188, 140]. One aims at understanding and controlling the pattern formation processes to design materials with patterns for special applications. Such an approach is complementary to *top-down* approaches, e. g., lithography. In particular, it allows to access the third dimension, i. e., patterns formed in the direction perpendicular to the surface, without any material deposition techniques.

One of the promising phenomena for creating well-defined structures in a bottom-up approach is Liesegang pattern formation [134, 143, 14, 85, 77, 204, 148, 78, 82, 23, 156, 126]. Liesegang rings or bands typically form if a substance diffuses from a centre or a peripheral edge into an initially homogeneous medium, where the reaction product precipitates and aggregates. The phenomenon is observed on macroscopic length scales (centimetres), typically for reaction-diffusion systems in gels [156, 126], but also in micrometer [204, 78, 23, 82] and nanometre regimes in solid materials [148].

Liesegang patterns are quantitatively described by three laws governing the creation time t_n, the distance x_n from the surface of the sample, and the width w_n of the nth band: time law $x_n \propto \sqrt{t_n}$, spacing law $x_{n+1} = (1+p)x_n$, and width law $w_n \propto x_n^\alpha$ (see [98] for a recent review). These laws have been derived in mean-field approaches based on (i) reaction-diffusion models with a threshold [55, 13, 130, 131] and (ii) phase-separating models with spinodal decomposition [12, 164].

In this paper we show that it is possible to obtain equidistantly spaced patterns by changing the coefficient p of the spacing law in a controlled fashion in space or in time. We derive a general approach, which is independent of a specific detailed reaction process and does not need a-priori knowledge of any process parameters.

We achieve equidistant patterns by either preparing a substrate with a gradient in the density of

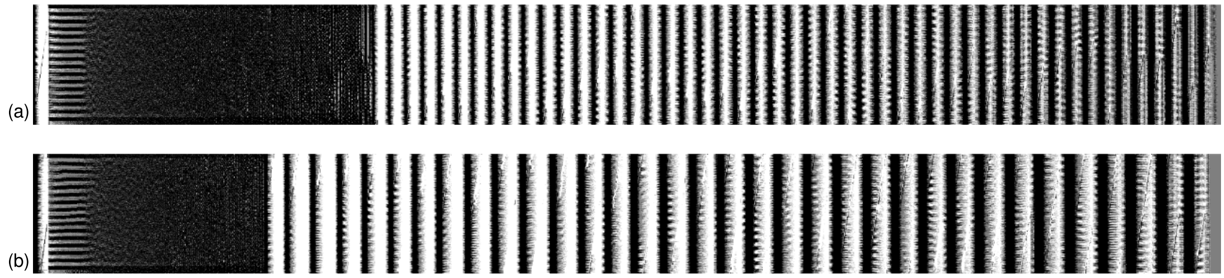

Figure 6.1.: 2d representation of the 3d Liesegang patterns with equidistant spacing obtained in lattice-gas simulations on a cubic lattice (32x32x2048). All 32 slices (in z direction) are plotted next to each other vertically (in y direction). Grey dots represent mobile C, and white dots represent precipitated D particles; A (not shown) diffused into the volume from the left. Equation (1) is fulfilled (a) by spatial variation of the nucleation threshold $K_{sp}(x)$ or (b) by spatial variation of the strength of heterogeneities. The simulation parameters are as follows: (a) $c_0 = 107.2$, $D_f = 1.22$, $D_C = 0.1$, $K_p = 19$, $F_1/\Delta_x = 0.01$, $F_2 = 1$ for equation (6.3), and (b) $c_0 = 107.2$, $D_f = 1.22$, $D_C = 0.1$, $K_{sp}^{\mathrm{het}} = 111$, $K_p = 37$, $F_1/\Delta_x = 0.005$, $F_2 = 1.1$, $F_2'' = 2.8$ for equation (6.4).

nucleation seeds or with a gradient in the strength of heterogeneities. Our approach is based on a theoretical formula for the spacing-law coefficient p originally derived in a mean-field model [13] and recently extended to include several different types of fluctuations [99]. We verify our predictions in a microscopic lattice-gas simulation [44, 45, 98, 99].

We define a pattern to be equidistantly spaced if the distance between the centres of all neighbouring bands is identical, i. e. $x_{n+1} = x_n + \Delta_x$ for all n; see figure 6.1 for illustration. Inserting the spacing law $x_{n+1} = (1+p)x_n$ yields the spatial dependence of the coefficient p,

$$p(x) = \Delta_x/x. \tag{6.1}$$

Since the Liesegang bands are created successively in space *and* time according to the time law, it is possible to transform equation (6.1) into a temporal version, i. e., $p(t)$, if the reaction profile is known.

Although equation (6.1) ensures that the spatial distances between the bands are identical, their widths w_n will not be the same. The reason is that w_n not only depends on p but also on the density d_n of the precipitated particles in the nth band. Because of particle conservation we have $w_n \propto p\,x_n/d_n$ [164, 98]. Naturally, one finds $w_n \propto x_n^{\alpha}$ with $\alpha \leq 1$ [98, 44, 45, 55]. Therefore, the density usually increases with the position of the band as $d_n \propto x_n^{1-\alpha}$. For equidistant bands, on the other hand, this implies a decrease of the band widths, since $w_n \propto \Delta_x/d_n \propto x_n^{\alpha-1}$. This is confirmed in the simulations shown in figure 6.1. However, the mass $m_n = w_n d_n$ of the bands is expected to be constant for equidistant bands. Nevertheless, the time law remains unchanged unless the diffusion process is modified in space or time.

Using equation (6.1) it is possible to obtain equidistant banding if the p dependence of one or more parameters of the reaction-diffusion process is known and if these parameters can be changed systematically in space and/or in time. It is even sufficient to know the dependencies in an empirical way. Parameters that could be varied include temperature, boundary conditions, concentrations of reacting particles, etc. An alternative approach, however, is the spatial variation of the substrate to impose the required $p(x)$. For example, a change of the dimensionality, i. e., a fractal structure would alter the diffusivity in space and time (fractal diffusion law).

Another possibility – the one we study here – is the spatial modification of the inhomogeneities

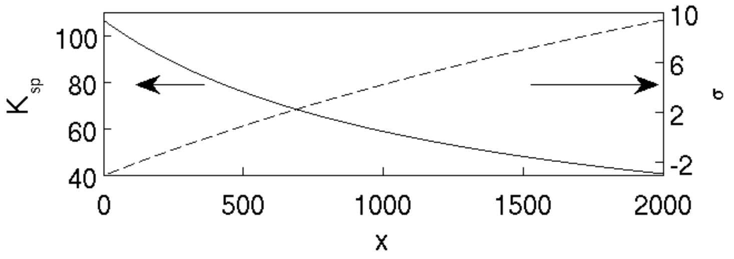

Figure 6.2.: Spatial dependence of $K_{sp}(x)$, solid line, and $\sigma(x)$, dashed line, used for obtaining equidistantly spaced Liesegang bands (same parameters as in figure 6.1).

or defects in the substrate, since nucleation and precipitation are altered by them. Experimentally this could be achieved, e. g., in glass substrates by irradiation with intense laser pulses in order to control Liesegang pattern formation of metal nano particles [148]. Since a broad (large-scale) gradient of inhomogeneities induced in the substrate before the actual reaction-diffusion process will be sufficient for equidistant banding on the micrometer scale (or below), this procedure can be regarded as real bottom-up pattern formation. It is complementary to approaches directly interfering with the detailed chemical reaction-diffusion processes in an homogeneous substrate [21].

We base our approach for equidistant patterns on a theoretical formula for the spacing-law coefficient p originally derived in a mean-field model [13] and later extended by three empirical approximations to include the effects of a growth threshold for the precipitates, thermal fluctuations of the particle densities, and random spatial fluctuations of the nucleation threshold [99]. The underlying nucleation and growth model for Liesegang pattern formation (see [98] for a review) assumes that one substance (B) is initially homogeneously distributed in the substrate and reacts with the other substance (A) diffusing into the sample from one surface. The reaction product (C) is mobile, but precipitates to form immobile particles (D) if its local concentration exceeds the nucleation threshold K_{sp}. In addition, the D particles grow at the expense of C as long as the local concentration of C remains above the growth threshold K_p. In this scenario the spacing-law coefficient is given by [99]

$$p = F_1 \frac{D_C}{D_f} \left[F_2 \frac{c_0}{K_{sp}} - 1 - \frac{D_C}{2D_f} \right]^{-1} \tag{6.2}$$

with D_f the effective diffusion coefficient of the reaction zone, c_0 the limit concentration of C (both of which can be calculated self-consistently from the initial concentrations and diffusivities of A and B), and D_C the diffusivity of C. F_1 and $F_2 = 1 + F_2'/\sqrt{c_0}$ are empirical parameters approximating influences of the band widths (controlled by K_p) as well as thermal fluctuations, respectively.

Inserting equation (6.1) into equation (6.2) it is easy to find the required spatial gradient of the nucleation threshold,

$$K_{sp}(x) = F_2 \frac{c_0 D_f}{D_C} \left[F_1 \frac{x}{\Delta_x} + \frac{D_f}{D_C} + \frac{1}{2} \right]^{-1} . \tag{6.3}$$

Figure 6.2 depicts $K_{sp}(x)$ for the parameters of the simulation shown in figure 6.1(a). Clearly, $K_{sp}(x)$ is decreasing with depth x from the substrate surface. However, the necessary decay is in general not a simple exponential as has been recently suggested for a specific detailed reaction

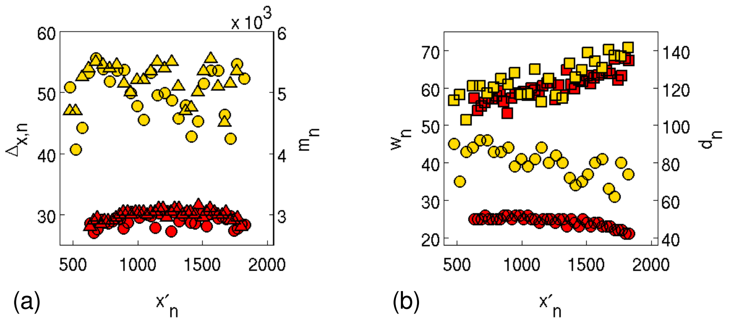

Figure 6.3.: Characterization of the bands depicted in figure 6.1, red symbols for homogeneous nucleation and yellow symbols for heterogeneous nucleation. (a) Individual inter-band distances $\Delta_{x,n}$ (triangles) and masses m_n (circles). The corresponding means and standard deviations are $\Delta_x = 30.1 \pm 0.8$ and 51.8 ± 3.0 lattice points and $m = 2919 \pm 107$ and 4957 ± 421 particles for homogeneous and heterogeneous nucleation, respectively. (b) Band widths w_n (circles) and densities d_n (squares).

process [150]. In order to optimize the number of Liesegang bands the parameters, in particular D_f/D_C, must be tuned such that $K_{sp}(x)$ decreases slowly.

Since the nucleation threshold might be difficult to modify directly in experiments, we also study – as a second alternative – inhomogeneous nucleation with K_{sp} randomly fluctuating in space. In this case it is sufficient to impose a gradient onto the width of the random fluctuations of K_{sp}, which corresponds to imposing a gradient on the inhomogeneity of the substrate. We consider a Gaussian distribution of the K_{sp} values with average K_{sp}^{het} and standard deviation σ [99]. Then an effective threshold K_{sp}^{eff} can be approximated by $K_{sp}^{\text{het}} - F_2''\sigma$ with an empirical parameter F_2''. Inserting K_{sp}^{eff} into equation (6.2) and using again equation (6.1) one obtains

$$\sigma(x) = \frac{K_{sp}^{\text{het}}}{F_2''} - \frac{F_2 c_0 D_f}{F_2'' D_C}\left[F_1 \frac{x}{\Delta_x} + \frac{D_f}{D_C} + \frac{1}{2}\right]^{-1}. \tag{6.4}$$

To achieve equidistant banding this way the constraint $0 < \sigma(x) \ll K_{sp}^{\text{het}}$ must hold, since the fluctuations cause random nucleation without banding if σ is in the order of the mean nucleation threshold K_{sp}^{het}. However, $\sigma(x)$ will eventually reach the mean nucleation threshold for large x according to equation (6.4). Therefore, the parameters determining the gradient of $\sigma(x)$ must be chosen such that $\sigma(x) \ll K_{sp}^{\text{het}}$ within the length of the sample. Figure 6.2 shows the $\sigma(x)$ used in the simulation depicted in figure 6.1(b). Because the pattern formation does not start at $x = 0$ one does not need $\sigma(x) > 0$ for small x.

Next we test our suggestions for equidistant Liesegang bands in a microscopic simulation. We impose equations (6.3) or (6.4), i. e., the gradients of $K_{sp}(x)$ or $\sigma(x)$ shown in figure 6.2, into a lattice-gas simulation of the nucleation and growth model described above. We refer to [99, 98] for a detailed description of the simulation procedure; note that K_{sp} and σ are kept constant in these previous papers. Figure 6.1(a) shows a representative result for homogeneous nucleation (spatial gradient $K_{sp}(x)$, $\sigma = 0$), while figure 6.1(b) is obtained with heterogeneous nucleation (constant K_{sp}^{het}, spatial gradient $\sigma(x)$).

Figure 6.3(a) confirms that the individual inter-band distances $\Delta_{x,n} = x_{n+1} - x_n$ and the masses $m_n = w_n d_n \approx c_0 \Delta_{x,n}$ are approximately constant. Figure 6.3(b) confirms that the widths w_n decrease with depth, while the densities d_n increase. The equidistant bands formed by homogeneous or heterogeneous nucleation are fully equivalent, the numerical differences in Δ_x and m_n being merely due to the chosen parameters. However, it is harder to achieve a low variance of $\Delta_{x,n}$ and m_n in the case of heterogeneous nucleation (see caption of figure 6.3).

The presented results of unbiased equidistant patterns have not been achieved in an ad-hoc way. We have rather obtained them following an optimization scheme which is described next. Such a scheme is necessary since the empirical parameters F_1, F_2, and F_2'' are not only unknown, but they also depend on K_{sp} [99]. To make things worse, the positions x_n of the bands are affected by an offset ξ in both experimental and simulation results, such that the theoretical positions x_n are related to the measured x'_n by $x_n = x'_n + \xi$ [98]. Equation (6.1) thus has to be rewritten as $p(x') = \Delta_x/(x' + \xi)$ with a ξ that is not know beforehand. The latter change also affects equations (6.3) and (6.4), where x must be replaced by $x' + \xi$.

Nevertheless, it is possible to achieve equidistant banding in an iterative procedure not requiring a-priori knowledge of the parameters ξ, F_1, F_2, and F_2'' (for heterogeneous nucleation only). Therefore, we are convinced that this procedure will also be applicable in experiments where the nucleation and growth model is not describing the processes exactly. Such a practical approach is consistent with bottom-up material design, since a full quantitative understanding of the process is not needed, if the desired structures can be obtained reliably.

We start the iterative procedure with arbitrary F_1/Δ_x, F_2, F_2'', and $\xi' = \xi + \delta\xi$, replacing x by $x' + \xi'$ in equations (6.1), (6.3), and (6.4). Since the error in guessing ξ is most crucial, we denote it as $\delta\xi$ here. The errors caused by incorrect F_1/Δ_x, F_2, and F_2'' can also be dealt with approximately via $\delta\xi$ as will be shown below. The bias error $\delta\xi$ causes a wrong spacing of the bands $x'_{n+1} - x'_n = x_{n+1} - x_n = p\, x_n = \Delta_x(x'_n + \xi)/(x'_n + \xi')$, i. e.,

$$(x'_{n+1} - x'_n)(x'_n + \xi') = \Delta_x(x'_n + \xi') - \Delta_x\delta\xi. \tag{6.5}$$

If the measured band positions x'_n of an experiment yield a linear plot according to this equation, both, Δ_x and $\delta\xi$ can be extracted from the linear fit, see figure 6.4(a). Then it is possible to reduce the linear trend in the inter-band spacings (due to $\delta\xi \neq 0$) by variation of ξ' in the next iteration of the experiment. On the other hand, if the plot according to figure 6.4(a) and equation (6.5) is not approximately linear, the information on the reaction process is insufficient to achieve equidistant banding.

Figure 6.4(b) shows that the bias error $\delta\xi$ can be eliminated by optimizing ξ'. Basically, one has to determine a few points in the plot and find the zero of $\delta\xi(\xi')$, which corresponds to finding the real ξ. Note that the final value of the inter-band spacing Δ_x is not known initially. Hence several runs with different F_1/Δ_x, F_2, and possibly F_2'' might be needed until a requested value of Δ_x can be obtained. This is shown in figure 6.4(c), where the Δ_x obtained for optimized equidistant spacing (optimized $\xi' = \xi$) is plotted for several values of F_1/Δ_x and three values of F_2 (homogeneous nucleation) as well as for two sets of values of F_2 and F_2'' (heterogeneous nucleation). The figure confirms that our optimization procedure can be applied for very different parameter sets. It suggests that the procedure might also work for Liesegang pattern formation in systems, where the nucleation and growth model is not the best modelling approach. In the experimental procedure, appropriate values for the parameters can be found iteratively, using plots like those in figure 6.4.

In summary, we have described an iterative procedure for obtaining equidistantly spaced Liesegang bands without a-priori knowledge of the specific process parameters. The approach is based on a continuous large-scale modification of the nucleation threshold or the heterogeneity of the substrate prior to the actual reaction-diffusion process leading to the banded precipitation. We have derived the procedure from the nucleation and growth model and confirmed it in extended Monte-Carlo lattice-gas simulations. We are convinced that the procedure can be applied experimentally

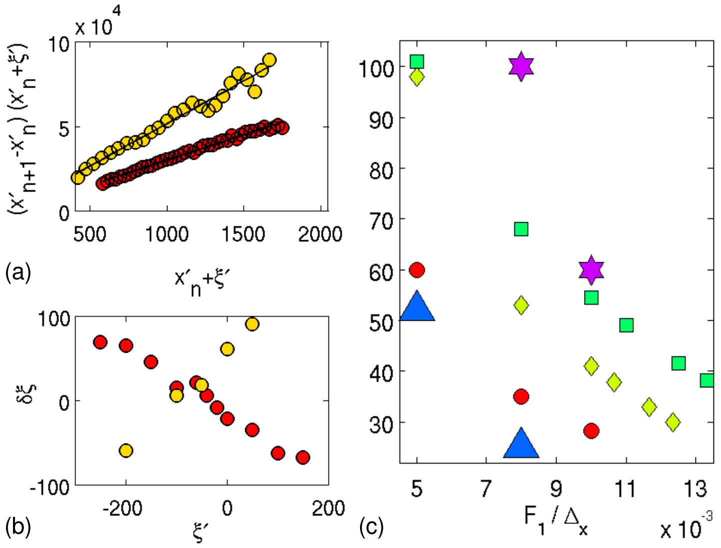

Figure 6.4.: (a and b) Analysis and optimization of the bias parameter $\delta\xi$ for obtaining equidistant bands, red symbols for homogeneous nucleation and yellow symbols for heterogeneous nucleation. (a) Fits of equation (6.5) (black lines) to the data of x_n (circles) with $\xi' = -44$ and -103 for homogeneous and heterogeneous nucleation, respectively. The fits yield $\Delta_x = 30.0$ and 50.4 with bias parameters $\delta\xi = -0.75$ and -26.85, respectively. (b) Bias parameters $\delta\xi$ versus ξ' as extracted from plots similar to the one shown in (a) and averaged over three configurations. (c) Optimized Δ_x for homogeneous nucleation (small symbols) and heterogeneous nucleation (large symbols). The parameters $c_0 = 107.2$ and $D_f = 1.22$ are identical for all results. We used $D_C = 0.1$, $K_p = 19$, and $F_2 = 0.8$ (red circles), 1 (yellow diamonds), and 1.25 (green squares) for homogeneous and $D_C = 0.05$, $K_{sp}^{\text{het}} = 111$, $K_p = 37$, $F_2'' = 2.8$, $F_2 = 1.1$ (blue triangles), and 1.5 (purple stars) for heterogeneous nucleation.

and is not limited to systems exactly described by the specific model. We suggest that it can be used in bottom-up material design for obtaining patterns in the direction vertical to a surface. The process could eventually be combined with in-plane structuring techniques such as lithography or precipitate dissolution (see, e. g., [113]) to obtain three-dimensional structures. Although we have restricted this paper to equidistantly spaced Liesegang bands, replacing equation (6.1) with an appropriately generalized ansatz and then following the same path will enable one to obtain many other patterns.

Acknowledgement We would like to thank Frank Lange for running some of the initial computer simulations. This work has been supported by the Deutsche Forschungsgemeinschaft (DFG, project B16 in SFB 418). *Acknowledgements*: We would like to thank Frank Lange for running some of the initial computer simulations. This work has been supported by the Deutsche Forschungsgemeinschaft (DFG, project B16 in SFB 418).

7. The effect of a small magnetic flux on the metal-insulator transition

Journal: Submitted to Physical Review B

Authors: Lukas Jahnke and Jan W. Kantelhardt
Institute: Institute of Physics, Theory group, Martin-Luther-Universität Halle-Wittenberg, 06099 Halle, Germany
Author: Richard Berkovits
Institute: Minerva Center and Department of Physics, Bar-Ilan University, Ramat-Gan 52900, Israel

Abstract: We numerically show that very small magnetic flux can significantly shift the metal-insulator transition point in a disordered electronic system. The shift for the 3d Anderson model obeys a power law as predicted by Larkin and Khmel'nitskii (1981). We calculate the exponent and find good agreement with the prediction. For small flux, the prefactor of the power law is larger than expected, leading to a surprisingly strong dependence of the transition point on the applied magnetic field. Furthermore, we show that the critical level-spacing distribution is hardly changed by the magnetic flux if hard-wall rather than periodic boundary conditions are applied.

7.1. Introduction

The interest in measuring small magnetic fields is driven by the possibility to build smaller magnetic storage devices with high capacity. Much progress in the understanding of the magnetic properties of condensed matter has been achieved in the last decades especially regarding thin layers [120]. Some of the results were honored by the Nobel price in physics in 2007 for the discovery of the giant magneto resistance by Fert and Grünberg.

In this paper we want to take a different path, studying the influence of a magnetic field on the metal-insulator transition (Anderson transition) in a disordered sample [9] rather than on the magnetization. Already in the eighties, Larkin and Khmel'nitskii [112] estimated the shift of the metal-insulator transition point based on a single-parameter scaling theory of the localization transition. This phenomenological theory assumes that two length scales determine the behavior of the system. The first is the correlation (or localization) length as function of the disorder parameter, $\xi(W) \propto |W - W_c|^{-\nu}$, where W_c is the critical disorder (at zero magnetic field) and ν the scaling exponent of the correlation length. The second relevant length scale is the magnetic length given by $L_B = \sqrt{\hbar/eB}$, where B is the magnetic field. Rewriting the usual single-parameter scaling theory of the conductivity with the ratio of these two length scales Larkin and Khmel'nitskii [112] obtained

$$\sigma(B, W) \propto \frac{e^2}{\hbar L_B} \Phi \left[\left(\frac{L_B}{\xi(W)} \right)^{1/\nu} \right], \tag{7.1}$$

where $\Phi[x]$ is a scaling function equal to zero when x is of order of unity. The conductivity will thus be zero for $\xi \approx L_B$, or, using the definition of the correlation length, the field-dependent critical disorder $W_c(B)$ is related to $W_c(0)$ by $W_c(B) - W_c(0) \propto L_B^{-1/\nu} \propto B^{1/2\nu}$ for small B. Replacing the magnetic field B by the magnetic flux ϕ yields

$$W_c(\phi) - W_c(0) = C\phi^{\beta/\nu} \quad \text{with } \beta = 1/2. \tag{7.2}$$

The prediction (7.2) was verified in different sophisticated analytical studies [219, 137, 35, 213, 159, 18, 179]. Numerical work, however, concentrated on the effect of large or random magnetic fluxes [185, 108, 158]. A computation of the shift of the mobility edge as function of the magnetic field was performed only once [58], with large error bars and for relatively large fluxes. However, since Eq. (7.2) should hold in particular for small fluxes a more thorough numerical analysis is needed.

Here we show that the shift of the critical disorder W_c for small magnetic fluxes generally follows the power law Eq. (7.2). We find a surprisingly large prefactor C, which leads to a very large shift even for small values of ϕ. The shift is consistent with results obtained for larger ϕ earlier [86]. However, deviations occur for very large fluxes in contrast to previously published results. Basically, half of the total shift in W_c takes place for fluxes smaller than the ones previously considered ($\phi < 0.01$). This could possibly be exploited for devices detecting small magnetic fields. Various experiments have demonstrated the possibility to reproduce properties seen in the Anderson model including effects of magnetic fields [147, 211, 203].

In addition to the shift of the critical disorder W_c induced by $\phi > 0$ a large change in the critical level-spacing distribution with magnetic field was reported [17]. These results were obtained with periodic boundary conditions. On the other hand, it is known that a change of boundary conditions also changes the critical level-spacing distribution [27, 173]. Here we show that for hard-wall boundary conditions the critical level-spacing distribution function is nearly independent of the magnetic flux. We also examine the second moment of the critical level spacing distributions and confirm its dependence on the boundary condition [27]. Furthermore, we examine its dependence on the magnetic flux for periodic and hard wall boundary conditions and find only very little changes in both cases.

The outline of the paper is as follows. In Section 7.2 we introduce the model and also describe the finite-size fitting procedures we employed to determine the critical disorders W_c. In Section 7.3 we discuss the main results presenting the phase diagram and comparing with Eq. (7.2). Section 7.4 is devoted to the effect of boundary conditions on the critical level spacing distribution and its second moment. Section 7.5 gives conclusion and outlook.

7.2. Model and finite-size scaling approach

To study metal-insulator transitions (MIT) on a 3D simple cubic lattice we consider the tight-binding Hamiltonian [9],

$$H = \sum_i \epsilon_i a_i^\dagger a_i - \sum_{(i,j)} t_{j,i} a_j^\dagger a_i, \tag{7.3}$$

where the first part represents the disordered on-site potential (homogeneous distribution $-W/2 < \epsilon_i < W/2$) and the second part describes the transfer between neighboring sites (i, j). A constant magnetic field $\mathbf{B}$ induces a phase shift through the vector potential $\mathbf{A}$ for non-diagonal matrix elements. Choosing Landau gauge, i. e. $\mathbf{A} = B(0, x, 0)$, the transfer probability is given by $t_{i,j} = \exp(2\pi\imath\phi n)$ with $n = \mathbf{r}_i \cdot \mathbf{e}_x$ for neighboring lattice points where $\mathbf{r}_i - \mathbf{r}_j = \pm\mathbf{e}_y$, and $t_{i,j} = 1$ otherwise. Here, we denote the ratio of flux φ trough a lattice cell with size a^2 to one flux quantum $\varphi_0 = h/e$ by $\phi = a^2 B/\varphi_0$. Note that the relation between the flux per plaquete and a given magnetic field depends on the lattice constant a.

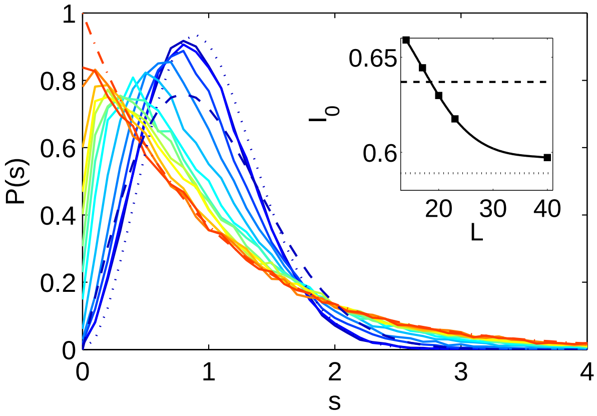

Figure 7.1.: The level spacing distribution $P(s)$ for a system of size $L/a = 40$ and magnetic flux $\phi = 10^{-3}$ per plaquete. In the metallic phase (blue curves) the level spacing follows the GUE distribution (dotted blue curve) rather than the GOE distribution (dashed blue curve). A clear transition from GUE to Poisson (dash-dotted red curve) behavior is observed as the disorder increases from $W = 8$ (continuous red curve) to $W = 23$ (continuous blue curve). Inset: System size dependence of $I_0 = \langle s^2 \rangle/2$ for $W = 10$. With increasing system size the GUE value (dotted line) is clearly reached asymptotically rather than the GOE value (dashed line).

In our numerical calculations the flux ϕ per plaquete (unit square) in the xy-plane is chosen between 8×10^{-4} and $1/4$. The lowest value is derived from the smallest system size $L/a = 14$ considered. For lower fluxes the magnetic length $L_B/a = 1/\sqrt{2\pi\phi}$ would become smaller than L, and the electrons could not accumulate a 2π phase shift. The largest flux we consider is given by the symmetry of the problem [89]. We choose hard wall boundary conditions in most calculations to avoid discontinuities in the phase accumulation of the hopping electrons due to the magnetic field.

To calculate the eigenvalues of 3D systems with the Hamiltonian (7.3) we use an iterative solver based on a general Davidson and Olsen algorithm [195, 195] where the matrix vector multiplication is performed by *Intel MKL Pardiso*. We calculate six eigenvalues around $|E| = 0$ for each configuration with linear system sizes ranging from $L/a = 14$ to $L/a = 40$ lattice points, accumulating between 2×10^5 and 2×10^6 eigenvalues for each system size. Only for the two smallest fluxes $\phi = 8 \times 10^{-4}$ and $\phi = 10^{-3}$ the system sizes are $L/a > 20$ and $L/a > 17$, respectively, to fulfill the condition $L \gg L_B$.

It is expected that a second-order phase transition occurs for a given critical disorder W_c. We study this transition by analyzing the level-spacing distribution $P(s)$ of consecutive eigenvalues E_i, with $s = (E_i - E_{i-1})/\Delta E$ and the mean level spacing ΔE. In the limit of infinite system size the level-spacing distribution $P(s)$ of a disordered system corresponds to a random-matrix theory result if the eigenfunctions are extended. For systems which obey time-reversal symmetry the corresponding random-matrix ensemble is the Gaussian orthogonal ensembles (GOE), well approximated by the Wigner surmise, $P_{\mathrm{GOE}}(s) = (\pi/2)s\exp(-\pi s^2/4)$ (dashed red line in Fig. 7.1). A magnetic field breaks the time reversal symmetry, changing the ensemble to a Gaussian unitary ensemble (GUE), for which the Wigner surmise yields $P_{\mathrm{GUE}}(s) = (32/\pi^2)s^2\exp(-4s^2/\pi)$ (dotted red line in Fig. 7.1). In contrast to the metallic phase, the uncorrelated energy levels of localized states are characterized by a Poisson distribution, $P_{\mathrm{P}}(s) = \exp(-s)$ (dashed dotted purple line in Fig. 7.1), independent of the symmetry. For finite systems $P(s)$ is between P_{GOE}

(or P_{GUE} with a magnetic field) and $P_{\mathrm{P}}(s)$. However, it approaches one of them with increasing system size, remaining system-size independent only at the transition point $W = W_c$.

To determine the critical disorder $W_c(\phi)$ we study the system-size dependence of the second moment of the level spacings $I_0 = \langle s^2 \rangle/2 \equiv \frac{1}{2}\int_0^\infty s^2 P(s)\,ds$, see the inset of Fig. 7.1. From one-parameter finite-size scaling arguments [183, 90, 91] it is expected that I_0 will depend on the disorder W and on the lattice size L if $W \neq W_c$, but become independent of L at $W = W_c$. The second moments of a Poissonian, GOE or GUE distribution can be calculated easily, yielding $I_{0,\mathrm{P}} = 1$, $I_{0,\mathrm{GOE}} = 0.637$ (dashed line in the inset of Fig. 7.1) and $I_{0,\mathrm{GUE}} = 0.589$ (dotted line).

Figure 7.1 shows the level-spacing distributions of a system of size $L/a = 40$ and magnetic flux $\phi = 10^{-3}$ per plaquete. A transition can be observed from a metallic phase, where the level-spacing distribution is close to GUE, ($W = 8$, continuous blue line) to an insulating phase with $P(s)$ close to Poisson, (for $W = 23$, continuous red line). When comparing the continuous blue line with the dotted blue curve, a clear similarity can be observed. This means that the universality class of the metallic state is GUE [$P_{\mathrm{GUE}}(s)$] rather than GOE [$P_{\mathrm{GOE}}(s)$]. There is no smooth crossover between GOE and GUE for linear system sizes larger than L_B. The asymptotic behavior can also be seen in the system size dependence of I_0 shown in the inset of Fig. 7.1. For large system sizes and low disorder ($W = 10$), I_0 reaches the GUE value asymptotically. The critical (system-size independent) level-spacing distribution $P_c(s)$ and the corresponding $I_{0,c}$ occur at $W_c \approx 17.25$ (continuous green line in Fig. 7.1) for $\phi = 10^{-3}$. The form of $P_c(s)$ will be discussed in Section 7.4.

Since we choose hard boundary conditions we need to take care of finite-size corrections due to irrelevant surface effects [187, 186]. Therefore we fit our data to a scaling form including these irrelevant surface effects decaying with system size as a power law, $I_0 = F(\Psi L^{1/\nu}, \Xi L^y)$ with the critical exponent ν, the relevant scaling variable Ψ, the leading irrelevant variable Ξ and the leading irrelevant exponent y. For finite system sizes L no phase transition takes place and F is a smooth analytical function. After expanding F to first order one gets

$$I_0(\phi, W, L) \quad = \quad F_0(\Psi L^{1/\nu}) + \Xi L^y F_1(\Psi L^{1/\nu}) \tag{7.4}$$

where F_0 and F_1 are analytical functions and are expanded to third order in the analysis of the numerical results. The relevant and irrelevant scaling variables are expanded in power series of the dimensionless disorder $w = (W_c - W)/W_c$. The relevant variable is expanded to first order, $\Psi(w) = \Psi_1(W_c - W)/W_c$, whereas we expand to zeroth order the irrelevant variable, $\Xi(w) = \Xi_0$. In total there are eleven independent fit parameters with W_c and ν being the interesting ones (see Ref. [187, 186] for the details of the procedure). In the procedure we fit our results of I_0 to Eq. (7.4) using a least-square method, i. e., a state of the art non-linear least-square fitting algorithm implemented in *Mathematica*.

Figure 7.2(a) shows results of such a non-linear fit for $\phi = 10^{-3}$ together with the simulation results for five system sizes ($L/a = 17, 20, 23, 30, 40$). As expected and already indicated in the inset of Fig. 7.1, I_0 drops with increasing system sizes approaching $I_{0,\mathrm{GUE}}$ for large system sizes if $W < W_c$. For $W > W_c$, on the other hand, I_0 increases with system sizes towards $I_{0,\mathrm{P}}$. At the critical disorder W_c, I_0 is system-size independent. The lines are the result of the simultaneous fit. Although it seems that all lines cross at $W \approx 16.7$ this is not the case as can be seen in the inset. This is due to the non-relevant variables $\Xi L^y F_1$ scaling with system size L.

Figure 7.2(b) shows that subtracting the non-relevant variables leads to a nice crossover for $W_c \approx 17.25$ indicating a system-size independent critical value of $I_{0,c} \approx 0.854$. Taking the whole range of fluxes it is possible to draw a phase diagram of fluxes and critical disorders.

To achieve better accuracy we do not only fit the results for each flux ϕ separately but also calculate combined non-linear fits over two ranges of fluxes form $\phi = 8 \times 10^{-4}$ to 4×10^{-3} and

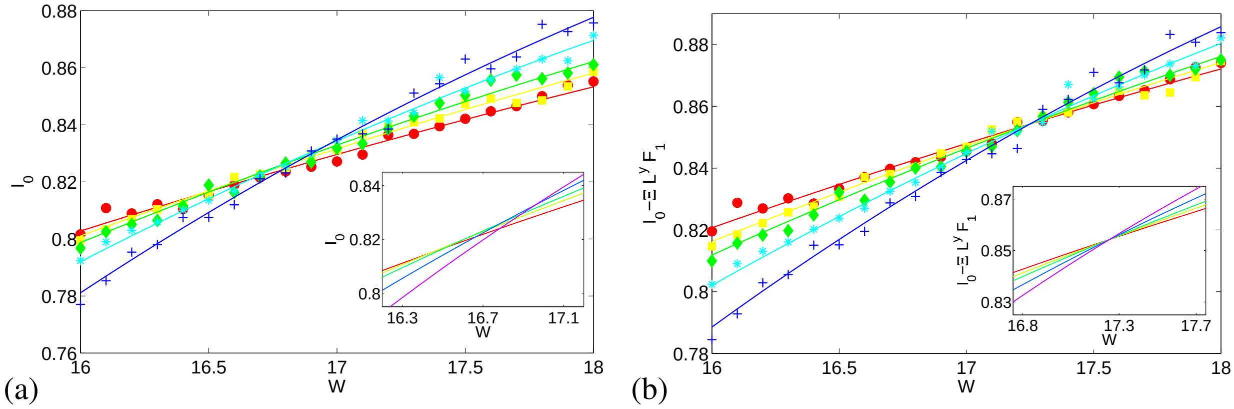

Figure 7.2.: The localization parameter $I_0 = \langle s^2 \rangle/2$ versus disorder W for system sizes $L/a = 17$ (red circles), $L/a = 20$ (yellow squares), $L/a = 23$ (green diamonds), $L/a = 30$ (light blue stars), and $L/a = 40$ (blue crosses) where a magnetic flux of $\phi = 10^{-3}$ is applied. The lines correspond to fits of Eq. (7.4). The symbols correspond to I_0. (a) A transition from extended states for small W to localized ones for large W is seen for all sample sizes. Nevertheless, the critical crossing point cannot be observed directly due to finite size effects. Inset: the region around $W = 16.7$ zoomed in; there is no single crosspoint. (b) Corrected values of I_0 where the influence of the irrelevant variables is subtracted. A clear transition can be seen at $W_c \approx 17.25$; all lines cross at one distinct critical disorder.

$\phi = 7 \times 10^{-3}$ to 0.1. Such an approach is possible since W_c is the only parameter in Eq. (7.4) changing significantly with ϕ for small values of ϕ. To check the stability of the fits we compare the results for combined fits with those for individual fits.

7.3. Phase diagram and scaling behavior of the transition

We have performed extensive numerical calculations for the entire range of magnetic fluxes [89] from $\phi = 0$ to $1/4$. The data is analyzed according to the description given in the previous section. For $\phi = 0$ we retrieve the well-known GOE value for the critical disorder $W_c = 16.57 \pm 0.13$ and the critical exponent $\nu = 1.62 \pm 0.09$ [187, 186]. For maximum flux, $\phi = 1/4$, we find $W_c = 18.14 \pm 0.12$ slightly lower and $\nu = 1.54 \pm 0.08$ slightly higher than previous results [185, 108, 158, 58]. The critical value $I_{0,c}$ is not changing much upon applying the flux; we observe $I_{0,c} = 0.829 \pm 0.006$ and $I_{0,c} = 0.808 \pm 0.008$ for $\phi = 0$ and $\phi = 1/4$, respectively. The result without flux is in agreement with previous work [27].

Figure 7.3 summarizes our numerical results for intermediate fluxes. The blue squares show the results $W_c(\phi)$ for fits of each individual ϕ. The error bars have been calculated as standard deviations obtained from approximately 1000 bootstrap samples each. The black symbols show the results of combined fits for $\phi = 8 \times 10^{-4}$ to 4×10^{-3} (squares) and $\phi = 7 \times 10^{-3}$ to 0.1 (diamonds). The values of the most important parameters W_c, ν and $I_{0,c}$ of the combined fits are also listed in Tab. 7.1. The error bars are the standard deviations for 500 bootstrap samples.

For the critical exponent we obtain $\nu = 1.42 \pm 0.04$ for small ϕ which is slightly lower but within the error bar range of a previous numerical study [185, 108, 158] ($\nu = 1.43 \pm 0.04$). For large ϕ we find $\nu = 1.62 \pm 0.06$. Our main goal, however, is studying the dependence of the critical disorder W_c on ϕ. The purple fit in Fig. 7.3 corresponds to small and the red fit to large

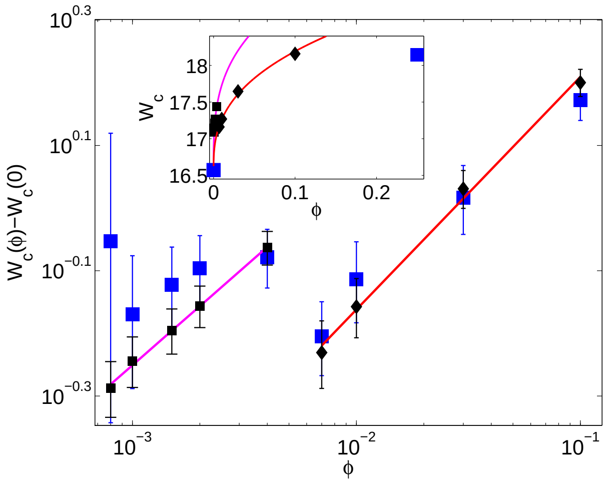

Figure 7.3.: The shift of the critical disorder W_c as function of the magnetic flux $\phi = a^2eB/h$. The blue symbols correspond to non-linear fits of Eq. (7.4) for each individual ϕ. The error bars indicate the standard deviation of approximately 1000 bootstrap samples. The black symbols are based on simultaneous non-linear fit of Eq. (7.4) with fluxes $\phi = 8 \times 10^{-4}$ to 4×10^{-3} (squares) and 7×10^{-3} to 0.1 (diamonds); the error bars are standard deviations of 500 bootstrap samples. The lines are linear fits of Eq. (7.2). Inset: the critical disorder W_c as function of ϕ for all values of the magnetic flux in a linear presentation (same symbols). Scaling holds for $\phi \leq 0.1$ only.

Table 7.1.: Combined fit results for fluxes $\phi = 8 \times 10^{-4}$ to 4×10^{-3} and $\phi = 7 \times 10^{-3}$ to 0.1 of critical disorder W_c, critical exponent ν, and critical $I_{0,c}$. Further parameters are the shift exponent β/ν, the shift pre-factor C and β. The error is estimated as the standard deviation of 500 bootstrap samples.

ϕ	W_c	W_c
0.0008	17.09 ± 0.06	
0.001	17.14 ± 0.06	
0.0015	17.21 ± 0.06	
0.002	17.27 ± 0.06	
0.004	17.44 ± 0.06	
0.007		17.16 ± 0.08
0.01		17.27 ± 0.08
0.03		17.65 ± 0.08
0.1		18.16 ± 0.08
$I_{0,c}$	0.846 ± 0.003	0.825 ± 0.005
ν	1.42 ± 0.04	1.62 ± 0.06
β/ν	0.31 ± 0.03	0.37 ± 0.03
β	0.45 ± 0.05	0.60 ± 0.07
C	4.9 ± 0.4	3.8 ± 0.1

ϕ. Since the calculation of the $W_c(\phi)$ values does not use ϕ as a fitting parameter, the power-law behavior confirms the prediction (7.2) by Larkin and Khmel'nitskii [112] discussed in the introduction. The exponents $\beta = 0.45 \pm 0.05$ for small ϕ and $\beta = 0.6 \pm 0.07$ for large ϕ are approximately in agreement with the predicted exponent $\beta = 1/2$, [112, 219, 137, 35, 213, 159, 18, 179] showing that the predicted power-law holds in both regimes. The crossover between the two regimes is mainly caused by a shift in $I_{0,c}$ (see Table I), i. e., slight modifications in the form of the critical level spacing distribution (see next section). The shift occurs in the same way, if other quantities like, e. g., $\gamma = [\int_2^\infty P(s)ds - \int_2^\infty P_{\mathrm{GUE}}(s)ds]/[\int_2^\infty P_{\mathrm{P}}(s)ds - \int_2^\infty P_{\mathrm{GUE}}(s)ds]$ are studied for determining $W_c(\phi)$. The crossover is comparable with effects caused by changing boundary conditions and might be related with a crossover to fully developped GUE symmetry upon increasing ϕ.

However, the prefactor C in Eq. (7.2) is surprisingly large in both cases, being 4.9 ± 0.4 and 3.8 ± 0.1 for small and large ϕ, respectively. The large C for small ϕ leads to a fast shift of the critical disorder with increasing field (see inset of Fig. 7.3). This result is consistent with a previous study considering larger ϕ only [86]. It is quite surprising how fast the critical disorder rises for small ϕ. Already at $\phi = 0.004$ more than half of the full shift in the critical disorder has taken place [$W_c(0.004) - W_c(0) = 0.87$]. For very high magnetic fluxes ($\phi > 0.1$) deviations from the power-law scaling (7.2) occur. We believe that the observed sensitivity to small magnetic fluxes may be used as a basis for building a magnetic sensor.

7.4. The critical level spacing distribution

In contrast to the critical disorder W_c the critical level-spacing distribution $P_c(s)$ is not universal. It depends on the boundary conditions [27] and the topology of the system. In the absence of a magnetic field the peak of the level distribution is shifted to smaller values of s when the boundary conditions are successively changed from periodic to hard-wall in each of the three spatial directions [27]. The tails of $P_c(s)$ for large s can be fitted by an exponential $P_c(s) \sim \exp(-\kappa s)$ with $\kappa = 1.87$ for periodic boundary conditions [17] and $\kappa = 1.49$ for hard-wall (Dirichlet) boundary conditions [173]. The critical level spacing distribution does not only change with boundary conditions but also when a magnetic flux is applied. The increase for low s changes from nearly linear to nearly quadratic, and the maximum becomes larger for periodic boundary conditions [17]. However, we are not aware of published numerical results of $P_c(s)$ for hard-wall boundary conditions.

Figure 7.4 shows the critical level-spacing distribution functions $P_c(s)$ for the Anderson model with different magnetic fluxes ϕ and periodic as well as hard-wall boundary conditions. The results confirm previous studies in the case of periodic boundary conditions. However, the changes in $P_c(s)$ for hard-wall boundary conditions are hardly significant. The average curves for small and large ϕ are very similar to the GOE curve (for $\phi = 0$), but not fully identical. In the intermediate case, $P_c(s)$ is slightly shifted to the left, possibly indicating a stronger effect of the boundary conditions in this case. The tails of the critical distributions follow the ansatz $P(s) \sim \exp(-\kappa s)$ with $\kappa = 1.88$ for periodic boundary conditions in good agreement with Ref. [17] independent of ϕ. For hard-wall boundary conditions we find two values for κ, depending whether a magnetic field is imposed or not. For $\phi = 0$ the result of Ref. [173] is confirmed, $\kappa = 1.49$. With magnetic field we find $\kappa = 1.38$ for all values of ϕ.

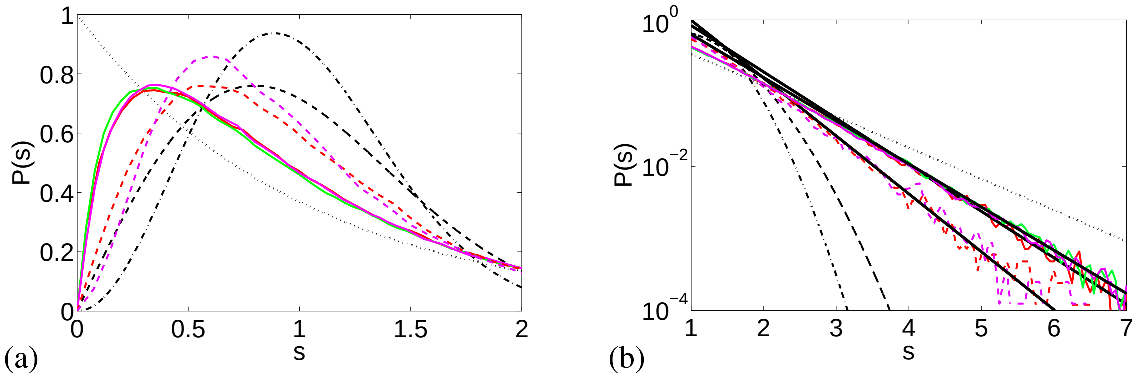

Figure 7.4.: (a) The critical level spacing distribution functions for periodic and hard-wall boundary conditions and different fluxes ϕ. For periodic boundary conditions $P_c(s)$ depends strongly on ϕ; examples for $\phi = 0$ (dashed red line) and $\phi = 0.1$ (dashed purple line) are shown. For hard-wall boundary the dependence nearly vanishes, as can be seen from the behavior of the continuous lines. The red line corresponds to the case without magnetic field, $\phi = 0$. The green and purple lines are the average $P_c(s)$ for $\phi = 8 \times 10^{-4}$ to 4×10^{-3} and $\phi = 7 \times 10^{-3}$ to 0.1, respectively. The limiting distributions are also shown, black dotted line – Poisson distribution, black dashed line – Wigner GOE, black dashed dotted line – Wigner GUE. (b) Semi-logarithmical plots of the same data. The blue lines are fits to the tails with $\kappa = 1.49$ and $\kappa = 1.38$ in hard-wall boundary conditions for $\phi = 0$ and $\phi > 0$, respectively, and $\kappa = 1.88$ for periodic boundary conditions.

7.5. Summary and concluding remarks

Our main goal has been to confirm that the shift in the critical disorder $W_c(\phi)$ for small values of the magnetic flux ϕ follows the scaling behavior $W_c(\phi) - W_c(0) = C\phi^{\beta/\nu}$ with $\beta = 1/2$ as predicted by Larkin and Khmel'nitskii [112]. After a careful numerical study we are able to confirm this prediction, however, the prefactor C is larger than expected from previous numerical studies [58, 86]. Very weak fluxes thus have a strong effect on the resistivity of a sample at low temperatures. This type of behavior naturally leads to the idea that the effect might be used as the basis of a very sensitive low-temperature sensor for magnetic flux.

In addition we have considered the effects of boundary conditions and magnetic fields on the details of the metal-insulator transition of a 3D Anderson model. The results can be summarized as follows. The critical disorder W_c is independent of the boundary conditions although it depends on ϕ. The opposite is true for the second moment $I_{0,c}$ of the critical level spacing distribution $P_c(s)$, which is nearly independent of ϕ in hard-wall boundary conditions and only depends on ϕ for periodic boundary conditions.

Acknowledgment: This work has been supported by the Minerva Foundation, the Israel Science Foundation (Grant 569/07), and the Deutsche Forschungsgemeinschaft (DFG, within SFB 418).

8. Wave localization in complex networks with high clustering

Journal: Physical Review Letters **101**, 175702 (2008)

Authors: Lukas Jahnke and Jan W. Kantelhardt
Institute: Institute of Physics, Theory group, Martin-Luther-Universität Halle-Wittenberg, 06099 Halle, Germany
Authors: Richard Berkovits and Shlomo Havlin
Institute: Minerva Center and Department of Physics, Bar-Ilan University, Ramat-Gan 52900, Israel

Abstract: We show that strong clustering of links in complex networks, i. e. a high probability of triadic closure, can induce a localization-delocalization quantum phase transition (Anderson-like transition) of coherent excitations. For example, the propagation of light wave-packets between two distant nodes of an optical network (composed of fibers and beam splitters) will be absent if the fraction of closed triangles exceeds a certain threshold. We suggest that such an experiment is feasible with current optics technology. We determine the corresponding phase diagram as a function of clustering coefficient and disorder for scale-free networks of different degree distributions $P(k) \sim k^{-\lambda}$. Without disorder, we observe no phase transition for $\lambda < 4$, a quantum transition for $\lambda > 4$ and an additional distinct classical transition for $\lambda > 4.5$. Disorder reduces the critical clustering coefficient such that phase transitions occur for smaller λ.

Anderson localization continues to spur excitement although half a century has passed since it was first conceived in the context of electron transport through disordered metals [9]. Since then new systems in which this phenomenon occurs were suggested and verified, such as light in strongly scattering media [215, 197] or photonic crystals [172, 127], acoustical vibrations in glasses [72] or percolation systems [106], and very recently atomic Bose-Einstein condensates in an aperiodic optical lattice [25, 165]. Clearly, new complex topologies can lead to novel physics. Therefore, in this Letter, we investigate the role played by clustering on the localization of waves in an experimentally realizable system of an optical network.

An optical communication network may be considered as a graph with edges representing optical fibers (or wave guides) and nodes representing optical units (essentially beam splitters) that redistribute incoming waves into outgoing fibers. Although constructing such a small network seems experimentally feasible, to the best of our knowledge it has not been performed. Theoretically, the propagation of electromagnetic or electronic waves in two and three dimensional disordered systems was studied with nodes on a lattice and bonds connecting nearest neighbors only [63]. However, if there are almost no losses along the edges, coherent effects are relevant for all edges including those connecting nodes spatially far from each other. Thus transitions in the transport properties of coherent waves on complex networks with long-range links are relevant to typical real-world communication networks [207, 33] and can be studied experimentally. Alternatively, one might consider a network of wave guides on the nanoscale similar to photonic lattices [172, 127]. Specifically, we suggest that Anderson localization should be observed upon changing the network topology [see Figs. 1(a,b)] instead of tweaking the disorder.

Compared with standard lattices, complex scale-free networks have additional degrees of freedom which define the topology of the network [57, 162, 4]. Focusing on the exponent λ of the power-law degree distribution $P(k) \sim k^{-\lambda}$ in scale-free networks and the clustering coefficient C (see below for exact definitions) [212, 209, 174, 177, 175, 176], we find that: (i) a localization-delocalization transition is induced by increasing C even in the absence of on-node (on-site) disorder W for $\lambda > 4$; (ii) the quantum transition point C_q moves to lower values when W is increased (continuous phase diagram); and (iii) the scaling exponent ν is very close to the mean-field value $\nu = 0.5$ for all values of λ and C_q, as may be expected for a system with high spatial dimension [65, 170]. We have also verified that similar results hold for networks with homogeneous or Erdös-Renyi type degree distribution $P(k)$. For $P(k) \sim k^{-\lambda}$ with $\lambda > 4.5$ (approximately) there is an additional distinct classical transition at a clustering coefficient $C_c > C_q$.

Theoretically, one may attempt to study quantum phase transitions using a scattering formulation of the wave propagation [178], or, as we have chosen here, by studying the spectrum of an Anderson model [9, 119] representing the complex network. Usually, diagonal (on-site) or non-diagonal (bond) disorder is introduced to obtain a localization transition [167]. An alternative approach is percolation, i. e. removing some fraction of all sites or bonds. In this case a classical transition [135] in which the infinite cluster breaks into finite pieces is found after the quantum phase transition [24]. Anderson and quantum percolation transitions, which seems to be in the same universality class, have been studied on different topologies including fractal structures [170], Cayley trees [166], and complex networks [47, 167]. In all cases, the transitions were induced either by on-site disorder or by cutting bonds (percolation) and thus changing the degree distribution of the network [47]. Here we show that it is possible to observe a quantum phase transitions by changing the clustering of the network without introducing on-site disorder or changing the degree distribution, thus keeping the total number of links constant. We find that clustering drives a localization transition in a way similar to disorder. Both clustering and strong backscattering due to disorder increase the probability of closed loops and thus the probability of interference.

Many random network models have been proposed to reproduce important aspects of real-world networks topologies [57, 162, 4]. The properties of such networks are usually characterized by four quantities: the degree distribution $P(k)$ (distribution of the number of neighbors k per node), the characteristic path length ℓ between two arbitrary nodes (small-world property), the clustering coefficient C (probability of triadic closures) and the assortativity (degree-degree correlations) [157].

Real-world networks exhibit a high clustering coefficient C indicating the presence of many loops on short length scales [57, 162, 4]. This global measure can be achieved by averaging over $C_i = 2T_i/[k_i(k_i-1)]$ [212], where T_i is the number of triangles passing through vertex i and k_i is its degree. However, since a global C cannot capture specific aspects of the network (e. g. varying degree-degree correlations can lead to networks with different topology but similar C [177, 175, 176]), it was suggested to average C_i within each degree class [207], yielding $\bar{C}(k)$.

To generate scale-free networks with tunable $P(k) \sim k^{-\lambda}$ (see [47] for details) and $\bar{C}(k)$, we have applied the algorithm suggested recently by Serrano and Boguñá [174]. Here we have chosen

$$\bar{C}(k) = C_0(k-1)^{-1}, \tag{8.1}$$

with C_0 between 0 (no clustering) and 1 (maximum clustering), which can be obtained without degree-degree correlations [177, 175, 176]. In the following, we will use the parameter C_0 instead of C or $\bar{C}(k)$, since a linear relation holds for $C_0 \leq 0.9$ (see inset in Fig. 8.1(d); larger C_0 should be treated with care). We obtained similar, however less reliable, results when generating

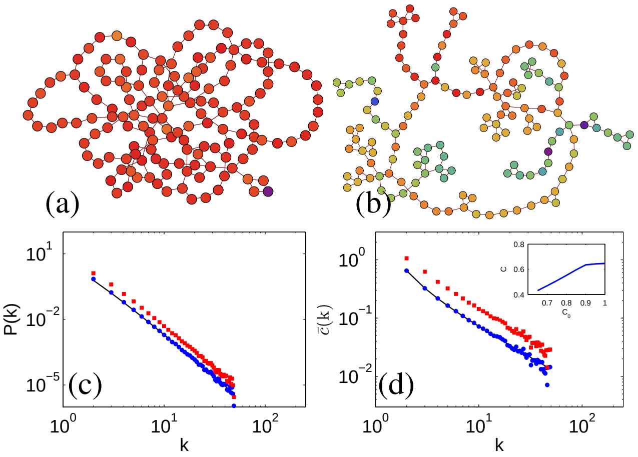

Figure 8.1.: (Color online) Representative pictures of the giant component of scale-free networks ($\lambda = 5$) (a) without and (b) with clustering ($C_0 = 0.6$). Both networks have giant components of similar size ($N \sim 150$); the size of the whole network being $N = 150$ for (a) and $N = 200$ for (b). The logarithmically scaled coloring presents the intensity of a mode with $E \approx 0.2$, red indicating the highest and violet the lowest probability. (c) degree distribution $P(k)$ and (d) clustering coefficients $\bar{C}(k)$ for scale-free networks with $\lambda = 4$ [line in (c)], $C_0 = 0.65$ [line in (d) according to Eq. (8.1)] and $N = 15000$ nodes, averaged over 120 configurations. Blue circles for distributions regarding the whole network and red squares for the giant component (with $\langle N_1 \rangle = 11906$ nodes; shifted vertically by a factor of 2). The inset shows that a linear dependence between C_0 and C holds also for the giant component if $C_0 \leq 0.9$.

networks with the algorithm of Volz [209] fixing C instead of $\bar{C}(k)$.

Figures 8.1(a,b) show two representative pictures of scale-free networks without and with clustering. Figures 8.1(c,d) compare the theoretical $P(k)$ and $\bar{C}(k)$ with the quantities we obtained numerically, considering the whole network or just the giant component. One can see good agreement in both cases. We want to stress that we do not change $P(k)$, the total number of links, and the number of nodes of the whole network, but only its structure by introducing clustering. Basically we rewire the network to achieve a higher clustering. The network can break for high clustering because nodes with low degree aggregate in finite clusters. We checked that the corresponding critical classical coefficient C_c is clearly larger than the critical quantum coefficient C_q if such a classical transition takes place.

Since each triangle represents a very short loop in the network, waves in networks with high clustering will have a high probability to return to the same node and to interfere. Since such interferences are the main reason for quantum localization, one may expect that strong clustering will induce localization. To study wave localization we consider the Anderson Hamiltonian [9, 119],

$$H = \sum_i \epsilon_i a_i^\dagger a_i - \sum_{(i,j)} t_{j,i} a_j^\dagger a_i, \tag{8.2}$$

where the first part represents the disordered on-site (node) potential (homogeneous distribution $-W/2 < \epsilon_i < W/2$) and the second part describes the transfer between each pair of nodes (i, j). For optical waves, one has $t_{i,j} = \exp(i\varphi_{i,j})$ for connected nodes ($\varphi_{i,j}$ is the optical phase accumulated along the bond), and $t_{i,j} = 0$ for disconnected nodes. For simplicity, we restrict $t_{i,j}$ to random values ± 1; the Hamiltonian thus remains in the orthogonal symmetry class. The extension to unitary symmetry is straightforward. In this scenario, the on-site disorder W results from variations in the optical units (beam splitters) located at the nodes.

By exact diagonalization, we have calculated the eigenvalues of the Hamiltonian (8.2) on the largest cluster for scale-free networks with various λ and C_0. Figures 1(a,b) show the intensities corresponding to two eigenmodes. Then we applied level statistics [90, 91] to determine the localization behavior of the modes and to extract the quantum phase-transition points. In disordered systems with extended eigenfunctions the energy spacing distribution $P(s)$ of consecutive eigenvalues (levels) E_i corresponds to the random-matrix theory result, well approximated by the Wigner surmise, $P_{\mathrm{W}}(s) = (\pi/2)s\exp(-\pi s^2/4)$. For localized states the level spacings are described by the Poisson distribution, $P_{\mathrm{P}}(s) = \exp(-s)$. For finite systems $P(s)$ is in between $P_{\mathrm{W}}(s)$ and $P_{\mathrm{P}}(s)$. However, it approaches one of them with increasing system size, remaining system-size independent only at the transition point. To determine this point for model parameters λ (exponent of degree distribution), C_0 [Eq. (8.1)], and W [below Eq. (8.2)], we study the system-size (N) dependence, of

$$\gamma = \frac{\int_2^\infty P(s)\,ds - \int_2^\infty P_{\mathrm{W}}(s)\,ds}{\int_2^\infty P_{\mathrm{P}}(s)\,ds - \int_2^\infty P_{\mathrm{W}}(s)\,ds}, \tag{8.3}$$

where $\gamma \to 0$ with $N \to \infty$ for extended states and $\gamma \to 1$ for localized states [183]. From finite-size scaling arguments [183] we expect that γ around $C_{0,q}$ will not only depend on C_0 but also on the diameter of the network L,

$$\begin{aligned}\gamma(C_0, W, L) \;&=\; \gamma(C_{0,q}, W_c, L) + \qquad\qquad (8.4)\\ &\quad\; [R_1|C_0 - C_{0,q}| + R_2|W - W_c|]\, L^{1/\nu},\end{aligned}$$

where R_1 and R_2 are constants and $L \propto \ln\left(a(C_0)N\right)$ [1]. This relation enables us to obtain the critical clustering coefficient $C_{0,q}$, the critical disorder W_c, and the critical exponent ν. Using Eq. (8.4) we have determined $C_{0,q}$ and W_c for scale-free networks with various λ. We also checked that equivalent results are obtained if other integral measures of $P(s)$ are studied, e. g., $I_0 = \frac{1}{2}\int_0^\infty s^2 P(s)\,ds$.

Considering large scale-free networks without disorder ($W = 0$) but varied C_0, Fig. 8.2 shows $P(s)$ versus s as well as the two limiting cases $P_{\mathrm{W}}(s)$ and $P_{\mathrm{P}}(s)$. One can clearly see that the shape of $P(s)$ changes from Wigner to Poisson with increasing C_0. We thus observe an Anderson-like transition although there are no disorder W and no changes in the degree distribution $P(k)$. The inset of Fig. 8.2 shows γ for five system sizes versus the clustering strength C_0. One can observe the quantum phase transition at the critical value $C_{0,q} \approx 0.69$ by the crossing of the five curves, indicating a system-size independent critical value of $\gamma_c \approx 0.76$.

Figure 8.3(a) shows the phase diagram for the transitions from localized (upper right) to extended (lower left) optical modes. The horizontal axis ($C_0 = 0$) corresponds to the case with no clustering studied before by Sade et al. [167], where the critical disorder W_c depends on λ. The main new finding of the present study regards the transitions on the vertical axis. Without disorder, the transition to the localized phase occurs at a critical clustering $C_{0,q}$ that depend on λ, i. e., the degree distribution. While even the strongest clustering $C_0 = 1$ cannot achieve such a transition if $\lambda < 4$, values of $C_{0,q} < 1$ are observed for $\lambda > 4$. The case $\lambda = 4$ seems to be limiting: this is the broadest degree distribution which allows a quantum phase transition upon increasing clustering.

---

[1] The N dependence is well established [48] but the C_0 dependence seems to be unexplored. Our data for N up to 10^5 suggest $\ln a \propto (C_0 - C_{0,c})^{-\nu_c}$. Since $C_{0,q} < C_{0,c}$, a and thus L depend weakly on C_0 at the quantum transition.

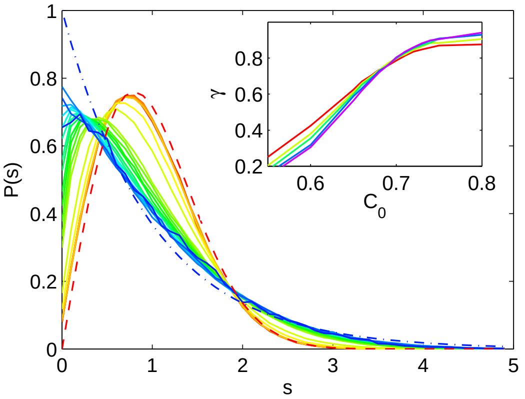

Figure 8.2.: (Color online) Level spacing distribution $P(s)$ for optical modes on scale-free networks with $\lambda = 5$, $N = 12500$ and no disorder, $W = 0$. A clear transition from Wigner (dashed red curve) to Poisson (dash-dotted blue curve) behavior is observed as a function of the clustering coefficient prefactor that is increased from $C_0 = 0.0$ (continuous red curve) to $C_0 = 0.90$ (continuous blue curve). Inset: localization parameter γ [see Eq. (8.3)] versus C_0 for networks with $N = 5000$ (red), $N = 7500$ (light green), $N = 10000$ (green), $N = 12500$ (blue), and $N = 15000$ (purple). A transition from extended modes for small C_0 to localized modes for large C_0 is observed at $C_{0,q} \approx 0.69$. The results are based on eigenvalues around $|E| = 0.2$ and 0.5.

If variations of C_0 and W are considered, the full phase diagram can be explored. Evidently, smaller values of C_0 are sufficient for quantum phase transitions if $W > 0$. We obtained similar phase diagrams for networks with homogeneous or Erdös-Renyi-type degree distributions (not shown). Within our error bars the critical exponent ν corresponds to the mean-field value $\nu = 0.5$ for infinite dimensions (see Fig. 8.3(b)) as expected from the Anderson transition [65].

To make sure that the quantum transition is induced by clustering and not by a classical phase transition we determent the corresponding classical critical clustering coefficient $C_{0,c}$. We find no indications of a classical transition for $\lambda < 4.5$, i. e. the giant component is not broken. For $\lambda = 5$ we find $C_{0,c} \approx 0.85$, significantly larger than $C_{0,q} \approx 0.69$ [see insets of Fig. 8.2 and Fig. 8.3(c)]. We thus conclude that the quantum transition for $W = 0$ is clearly different from the classical one in two ways: (i) there is no classical transition between $4 < \lambda < 4.5$ although a quantum transition is clearly seen, and (ii) for $\lambda > 4.5$, the quantum transition occurs for lower C_0 values than the classical one. This leaves an intermediate regime ($C_{0,q} < C_0 < C_{0,c} \leq 1$) in which all modes are localized although there is a spanning giant cluster.

In summary, we have shown that quantum phase transitions of wave-like modes (similar to the Anderson transition and to the quantum percolation transition) can be obtained in a complex network without introducing on-site disorder or bond disorder or tampering with the degree distribution (i. e. the number and distribution of links). One only needs to change the clustering coefficient of the network, which corresponds to a rewiring procedure.

We conclude that clustering represents a new degree of freedom that can be used to induce and study phase transitions in complex networks. Comparing systems with different clustering properties might enable one to find the most relevant cause of quantum localization. We propose that the phenomenon should be observable experimentally and relevant in complex coherent optical networks made of fibers and beam splitters. Such experiments will directly probe the influence of complex network topology on the Anderson localization of light [215, 197, 172, 127].

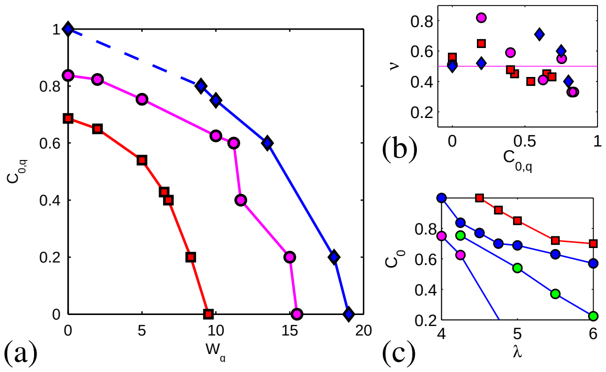

Figure 8.3.: (Color online) (a) Phase diagram for transitions from localized optical modes (upper right) to extended modes in parts of the spectrum (lower left) for different degree distribution exponents λ, $\lambda = 4$ (blue diamonds), 4.25 (magenta circles), and 5 (red squares). Data for $C_0 > 0.9$ are not reliable for network generation reasons, and the error bar for the point at $C_0 = 1$ is about 0.1. (b) Exponent ν for different λ and $C_{0,q}$. The values are, within the error bars (not shown), consistent with the mean-field prediction $\nu = 0.5$. (c) Quantum transitions without disorder (blue circles) and classical transitions (red squares) as a function of the degree exponent λ. In the regime $4 < \lambda < 4.5$ only quantum transitions occur. For $W > 0$ the curves move downwards making quantum transitions possible for $\lambda < 4$ (green circles for $W = 5$ and magenta circles for $W = 10$).

Acknowledgment: This work has been supported by the Minerva Foundation, the Israel Science Foundation (Grant 569/07 and National Center for Networks), the Israel Center for Complexity Science and the Deutsche Forschungsgemeinschaft (DFG, within SFB 418).

9. Wave localization on complex networks

Book: Information Theory and Statistics in Complex Networks
Editors: Frank Emmert-Streib and Matthias Dehmer

Author: Richard Berkovits
Institute: Minerva Center and Department of Physics, Bar-Ilan University, Ramat-Gan 52900, Israel
Authors: Lukas Jahnke and Jan W. Kantelhardt
Institute: Institute of Physics, Theory group, Martin-Luther-Universität Halle-Wittenberg, 06099 Halle, Germany

9.1. Introduction

9.1.1. Motivation

Anderson localization continues to spur excitement although half a century has passed since it was first conceived in the context of electron transport through disordered metals [9, 119]. Since then new systems in which this phenomenon occurs were suggested and verified, such as light in strongly scattering media [215, 197] or photonic crystals [172, 127], acoustical vibrations in glasses [72] or percolation systems [106], and very recently atomic Bose-Einstein condensates in an aperiodic optical lattice [25, 165]. The Anderson transition, first predicted in 1958 [9], has been a central topic in condensed matter physics for the last half century. The main idea is that a phase transition from extended (metallic) to localized (insulating) eigenstates exists as a function of the disorder or energy of a quantum system. This transition will be manifested by a change in the transport through the system from metallic to insulating conductance. The transition is conceptually different from the canonical explanation for the existence of insulators in solid state (i. e., the Fermi energy is in the gap between energy band), since for the Anderson insulator the Fermi energy is in the middle of the band. Nevertheless, since the states available are localized due to the disorder, no current can pass through the system.

Although the insulating behavior is due to disorder, it is nevertheless quite different in origin from the percolation transition. While in the percolation transition no direct path exists between the two edges of the sample, in the Anderson transition such paths do exist, nevertheless the probability of current transversing the sample is exponentially small due to constructive interference between time reversed paths. Thus, the Anderson transition takes into account the quantum (or wave) nature of the particle diffusing through the sample, while the percolation transition is classical in nature.

The fact that the Anderson transition depends on interference effects between time reversed paths leads to an interesting dependence of the Anderson transition on the dimensionality of the

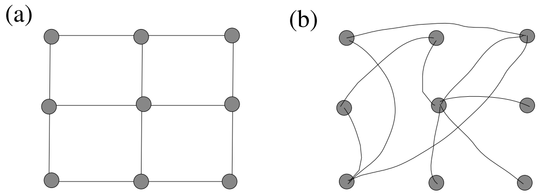

Figure 9.1.: Possible realizations of optical networks constructed from beam splitters (cavities) represented by circles and optical fibers (wave guides) represented by lines. (a) A regular lattice. (b) A complex network.

system. The lower critical dimension, below which the system is localized for all values of disorder, is believed to be two [1], since the probability of returning to the origin (i. e., constructive interference due to time reversal symmetry) stays non-zero in the limit of infinite system size for $d \leq 2$. The upper critical dimension (for which the system remains metallic for any amount of disorder) remains uncertain although it is generally believed to be infinity [34, 122, 198, 136, 65].

Most of the studies concerning the Anderson transition have considered regular lattices with on-site or bond disorder. Interest in the influence of the unusual topologies of complex networks on the properties of quantum interference is rising. Indeed, recently the Anderson transition in particular networks, namely small-world networks [222, 79, 81], the Cayley tree [166], random regular graphs, Erdös-Rényi graphs and scale-free networks [167] were studied. One may justify this interest by the light the study of the Anderson transition on complex networks sheds on the general properties of the transition, but here we would like to emphasis that complex networks could be actually realized in real-world situations such as optical networks.

Hence we shall begin by describing an example of an experimentally realizable system of a complex network, i. e., an optical network. We shall show that optical networks may be described using a tight binding Hamiltonian. We shall then describe how one can determine the properties of the Anderson transition using our knowledge of the statistical properties of the eigenvalues of the Hamiltonian. Then the Anderson transition properties of different complex networks will be studied. Finally we investigate the role played by clustering on the localization of waves. We shall show that new complex topologies lead to novel physics, specifically clustering may lead to localization.

9.1.2. Optical network

A fresh view on the relevance of complex network models to real-world localization comes from considering optical networks. There is a long history of considering optical (or microwave) systems as a tool to analyze localization behavior. In 1982 Shapiro [178] has generalized a model proposed by Anderson *et al.* [8] to describe localization in disordered systems. Instead of considering a tight-binding description of a lattice, Shapiro considers a model in which sites are represented by beam splitters or cavities and bonds by optical fibers or wave guides (see Fig. 9.1(a)). From a theoretical point of view, this description is convenient in order to describe the system using the scattering matrix formalism. This description was taken a step further by Edrei *et al.* [63] who applied it to describe the dynamics of wave propagation (for example acoustic or light waves) in a disordered medium.

One should realize that such a description can form the basis of a realistic network which may be built in a lab. For example a network of beam splitters and optical fibers similar to the one sketched in Fig. 9.1(b) may be constructed and its localization properties experimentally studied. Since optical fibers have a very low loss rate, there is no essential difference between connecting neighboring nodes of the network, or far away ones. Moreover, since in any realistic optical set-up the length of the optical fiber is much longer than the wave length even for nearest-neighbor nodes, there is no correlation between the phase gained by the wave as it transverses the distance between two nodes and the physical distance between the nodes. Thus, in principal any form of a complex network (small-world network, Cayley tree, random regular graph, Erdös-Rényi graph and scale-free network) can be constructed and measured on an optical bench. Although constructing such a small network seems experimentally feasible, to the best of our knowledge it has not been performed.

Thus transitions in the transport properties of coherent waves on complex networks with long-range links are relevant to typical real-world communication networks [33, 207] and can be studied experimentally. Alternatively, one might consider a network of wave guides on the nanoscale similar to photonic lattices [172, 127].

Although we illustrated the analogy between optical and electronic systems using the scattering matrix formulation it is nevertheless quite general. It is known that the scalar wave equation is a good approximation for the propagation of an optical wave in an inhomogeneous medium as long as polarization effects are not important. The scalar wave equation may be written as

$$\nabla^2\Psi + \frac{\epsilon(\mathbf{r})}{c^2}\frac{\partial^2}{\partial^2 t}\Psi = 0, \tag{9.1}$$

where $\epsilon(\mathbf{r}) = 1+\delta\epsilon(\mathbf{r})$ describes the local fluctuations in the dielectric constant and c is the speed of light. Assuming a monochromatic wave one may rewrite $\Psi(\mathbf{r},t) = \psi(\mathbf{r})\exp(i\omega t)$, where ω is the frequency of the wave. Inserting $\Psi(\mathbf{r},t)$ into the scalar wave equation (Eq. (9.1)) will result in

$$-\nabla^2\psi - \delta\epsilon(\mathbf{r})\psi = \left(\frac{\omega}{c}\right)^2\psi. \tag{9.2}$$

When this is compared with the stationary Schrödinger equation with a varying potential $U(\mathbf{r}) = U + \delta U(\mathbf{r})$,

$$-\nabla^2\psi + \frac{2m}{\hbar^2}\delta U(\mathbf{r})\psi = \frac{2m}{\hbar^2}(E-U)\psi, \tag{9.3}$$

it can be seen that the Schrödinger equation and the scalar wave equation in random media are identical up to constants. Thus, one may use techniques developed in the field of electronic localization in order to study the properties of optical networks. One such approach is determining the Anderson transition from the statistics of the eigenvalues of the Hamiltonian describing the system. In the extended phase the distribution of the eigenvalues is expected to follow the appropriate Gaussian ensemble (i. e., if the Hamiltonian follows time-reversal symmetry it should follow the Gaussian orthogonal ensemble, GOE, while in the presence of a magnetic field which breaks time-reversal symmetry it is expected to follow the Gaussian unitary ensemble, GUE). On the other hand in the localized regime the eigenvalues are expected to follow Poissonian statistics. Thus, by changing the disorder a system described by Eq. (9.3) should exhibit a transition from the appropriate Gaussian ensemble in the metallic phase to a Poisson statistics in the localized phase. This transition should show the usual finite-size behavior expected for a second order phase transition, and thus finite-size scaling may be used to determine the transition point [183].

9.1.3. Introduction Anderson model and level statistics

To study wave localization we consider the Anderson Hamiltonian [9],

$$H = \sum_i \epsilon_i a_i^\dagger a_i - \sum_{(i,j)} t_{j,i} a_j^\dagger a_i, \tag{9.4}$$

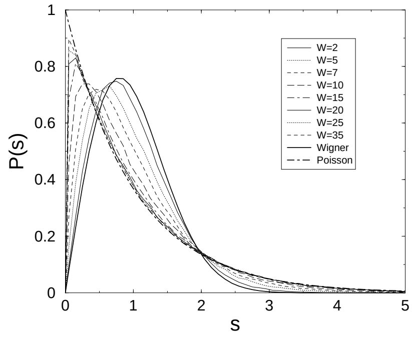

Figure 9.2.: The distribution $P(s)$ for a 500 sites scale-free graph with $\lambda = 4$ ($m = 2$). A clear transition from Wigner to Poisson is observed as a function of disorder.

where the first part represents the disordered on-site (node) potential (homogeneous distribution $-W/2 < \epsilon_i < W/2$) and the second part describes the transfer between each pair of nodes (i, j). For optical waves, one has $t_{i,j} = \exp(i\varphi_{i,j})$ for connected nodes ($\varphi_{i,j}$ is the optical phase accumulated along the bond), and $t_{i,j} = 0$ for disconnected nodes. For simplicity, we restrict $t_{i,j}$ to random values ± 1; the Hamiltonian thus remains in the orthogonal symmetry class. The extension to unitary symmetry is straightforward. In this scenario, the on-site disorder W results from variations in the optical units (beam splitters) located at the nodes.

Then we applied level statistics [91] to determine the localization behavior of the modes and to extract the quantum phase-transition points. The Hamiltonian is diagonalized, and one obtains N eigenvalues E_i (where N is the number of nodes in the graph). A very useful characterization of the statistics of the eigenvalues is the distribution $P(s)$ of adjacent level spacings s, where $s = (E_{i+1} - E_i)/\langle E_{i+1} - E_i\rangle$, and $\langle \ldots \rangle$ denotes averaging over different realizations of disorder or other random features of the network such as different realizations of node connectivities.

One expects the distribution to shift as function of disorder from the Wigner surmise distribution (characteristic of Gaussian orthogonal ensembles),

$$P_{GOE}(s) = \frac{\pi s}{2} \exp\left[-\frac{\pi s^2}{4}\right], \tag{9.5}$$

at weak disorder to a Poisson distribution (characteristic of localized states) at strong disorder,

$$P_P(s) = \exp[-s]. \tag{9.6}$$

Examples of such transitions for a particular complex network can be seen in the following sections (Fig. 9.2). As the on-site disorder W increases, $P(s)$ shifts from the GOE toward the Poisson distribution. Additional features of the Anderson transition, such as the fact that all curves intersects at $s = 2$ and the peak of the distribution climbs along the Poisson curve for larger values of W are also seen.

At the transition the distribution will not change as function of the system size while for weaker disorder the distribution will become more GOE like as the system size increases and for stronger disorder it will become more Poisson like as function of the system size. The transition point can thus be determined by a finite-size scaling procedure [183], which will be described in detail further on.

9.2. Statistical properties of the spectra of complex networks

In the following section we shall present the results of numerical studies of the spectral statistics of different classes of complex networks which have been mainly published in Ref. [167]. The features of the Anderson metal-insulator transition are found to be similar for a wide range of different networks. A metal-insulator transition as a function of the disorder can be observed for different classes of complex networks for which the average connectivity is small. The critical index of the transition corresponds to the mean field expectation (i. e., $\nu = 0.5$). When the connectivity is higher, the amount of disorder needed to reach a certain degree of localization is proportional to the average connectivity, though a precise transition cannot be identified. The absence of a clear transition at high connectivity is probably due to the very compact structure of the highly connected networks, resulting in a small diameter even for a large number of sites.

9.2.1. Characteristics of the different Networks

We shall begin by a short definition of the characteristics of the different networks we consider.

Random graph

A random graph (or- random regular graph) is a graph with N nodes, each is connected to exactly k random neighbors [4]. The diameter of a graph is the maximal distance between any pair of its nodes. In a random graph the diameter d is proportional to $\ln N$. In Sect. 9.2.3 we shall present results of the level spacing distribution for random-regular graphs with $k = 3$.

Erdös-Rényi graphs

In their classical model from 1959 Erdös and Rényi (ER) [67] describe a graph with N nodes where every pair of nodes is connected with probability p resulting in $\langle k\rangle = Np$. For a large random graph the degree distribution follows the Poisson distribution:

$$P(k) = e^{-\langle k\rangle}\frac{\langle k\rangle^k}{k!}. \tag{9.7}$$

The diameter of such a graph follows: $d \sim \ln N$, similar to a random graph. In Sect. 9.2.3 we have specifically calculated the level distribution for $\langle k\rangle = 3, 3.1, 3.2, 3.5, 4, 5, 7.5$ and 10.

Scale-free networks

Scale-free (SF) networks [5] are networks where the degree distribution (i. e., fraction of sites with k connections) decays as a power-law. The degree distribution is given by [104] :

$$P(k) = ck^{-\lambda}, m < k < K,$$

where $c = (\lambda - 1)m^{\lambda-1}$ and $K = mN^{1/(\lambda-1)}$ [47], λ is the power-law exponent, m is a lower cutoff, and K is an upper cutoff . Thus, there are no sites with degree below m or above K. The diameter of the SF network can be regarded as the mean distance of the sites from the site with the highest degree. For graphs with $2 < \lambda < 3$ the distance behaves as $d \sim \ln(\ln(N))$

[48], and for $\lambda = 3$ as $d \sim \ln(N)/\ln(\ln(N))$ [26]. This anomalous behavior stems from the structure of the network where a small core containing most of the high degree sites has a very small diameter. For higher values of λ the distance behaves as in ER, i. e., $d \sim \ln(N)$. The $\langle k \rangle$ of a SF graph is obtained by the following expression:

$$\langle k \rangle = \frac{1-\lambda}{2-\lambda} \times \frac{K^{2-\lambda} - m^{2-\lambda}}{K^{1-\lambda} - m^{1-\lambda}} \tag{9.8}$$

For $\lambda > 2$ and large enough N the average degree ,$\langle k \rangle$, is a constant. The results for SF networks presented in Sect. 9.2.2 correspond to $\lambda = 3.5, 4, 5$ with $m = 2$ (lower cutoff), and $\lambda = 4, 5$ with $m = 3$. Due to their small diameter, SF networks with $\lambda < 3$ were not considered.

Double peaked distributions

In order to find hierarchical relation between the different graphs, we studied also some variations on these graphs. For a random graph we changed the degree of a small percent of the nodes, so we have a graph with double peaked distribution. Thus, the average connectivity, $\langle k \rangle$, is the average degree of the nodes. Several examples were taken: changing 5% of the nodes to $k = 5$ (instead of $k = 3$) resulting in $\langle k \rangle = 3.1$, or changing 5% of the nodes to $k = 10$ ($\langle k \rangle = 3.35$). Replacing 20% of the nodes connectivity for the previous cases will result in $\langle k \rangle = 3.4$ (for $k = 5$ nodes) and $\langle k \rangle = 4.4$ (for $k = 10$ nodes). Additionally, in order to relate with previous results of the metal insulator transition on a Cayley-tree [166] we checked a tree in which 5% of its nodes have higher degree ($k = 4$) resulting in an average connectivity 3.05 and creating few closed trajectories - loops.

9.2.2. Method

Now we turn to the calculation of the spectral statistics of these networks. First, one must construct the appropriate network structure, i. e., to determine which node is connected to which. This is achieved using the following algorithm [47, 149]:
1. For each site choose a degree from the required distribution.
2. Create a list in which each site is repeated as many times as its degree.
3. Choose randomly two sites from the list and connect this pair of site as long as they are different sites.
4. Remove the pair from the list. Return to 3.

The diameter of a graph is calculated by building shells of sites [104]. The inner shell contains the node with the highest degree, the next contains all of its neighbors, and so on. Of course, each node is counted only once. The diameter of the system is then determined by the number of shells. Two more options which were considered are defining the diameter by the most highly populated shell, or by averaging over the shells. The diameter obtained by the various methods are quite similar.

The energy spectrum is calculated using the usual tight-binding Hamiltonian defined in Eq. (9.4). The on-site energies, ε_i are uniformly distributed over the range $-W/2 \leq \varepsilon_i \leq W/2$. The hopping matrix element $t_{j,i}$ is set to 1 for nearest neighbor nodes which are determined according to the network structure, and to 0 for unconnected nodes. We diagonalize the Hamiltonian exactly, and obtain N eigenvalues E_i (where N is the number of nodes in the graph) and eigenvectors ψ_i. Then we calculate the distribution $P(s)$ of adjacent level spacings s defined above.

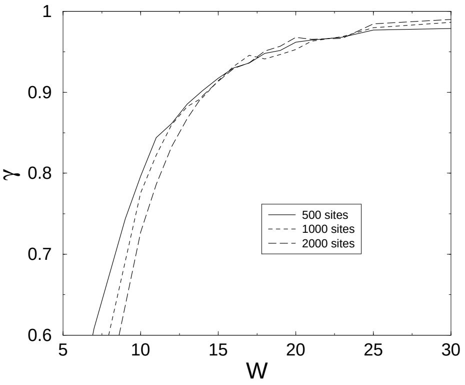

Figure 9.3.: γ as function of W for different SF graphs sizes ($\lambda = 4$ and $m = 2$). The typical behavior for finite size transition is seen, where a crossing in the size dependence of γ between the metallic (small values of W) and localize (large value of W) regime is seen.

An example for such a transition is presented in Fig. 9.2 where a scale-free graph with $\lambda = 4$ and $m = 2$ was considered. As W increases $P(s)$ shifts toward the Poisson distribution. Additional hallmark features of the Anderson transition, such as the fact that all curves intersects at $s = 2$ and the peak of the distribution "climbs" along the Poisson curve for larger values of W are also apparent. Similar transition from Wigner to Poisson statistics is seen also for the other networks considered in this study.

The transition point can be determined more accurately from calculating [183]

$$\gamma = \frac{\int_2^\infty P(s)ds - \int_2^\infty P_w(s)ds}{\int_2^\infty P_p(s)ds - \int_2^\infty P_w(s)ds}, \tag{9.9}$$

where $\gamma \to 0$ as the distribution tends toward the Wigner distribution, and $\gamma \to 1$ if the distribution approaches the Poisson distribution. One expects that as the system size increases, the finite size corrections will become smaller resulting in a distribution closer to a Wigner distribution in the metallic regime and to Poisson in the localized one. At the transition point the distribution should be independent of the system size. In Fig. 9.3 we plot the behavior of γ as function of W for several sizes of a scale-free graph. Indeed, γ decreases with system size for small values of W while it increases with size for large values of W.

All curves should cross around a particular value of disorder signifying the critical disorder. From finite size scaling arguments [183] one expects that γ around the critical disorder will depend on the disorder and network size, L, in the following way:

$$\gamma(W, L) = \gamma(W_c, L) + C \left| \frac{W}{W_c} - 1 \right| L^{1/\nu}, \tag{9.10}$$

where C is a constant. This relation enables us to extract both the critical disorder W_c and the critical index ν. Scaling of the numerical data according to Eq. (9.10) yields two branches corresponding to the metallic and localized regimes, that are clearly seen in Fig. 9.4. The estimated values of ν and W_c (see Table I) are extracted by fitting the branches to a 4th order polynomial.

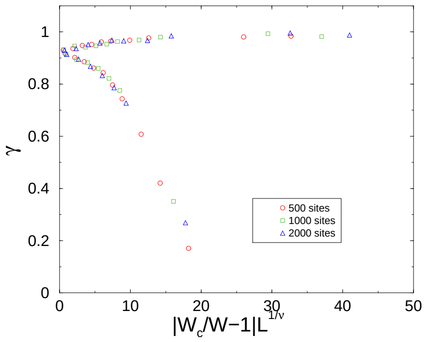

Figure 9.4.: The scaling of γ according to Eq. (9.10) for different SF, $\lambda = 4, m = 2$, networks sizes. Two branches, corresponding to the metallic and localized regimes, appear.

Network	$\langle k \rangle$	l	W_c	ν
Scale-Free , $\lambda = 4$, $m = 2$	2.97	12.46	15.7±0.9	0.55±0.11
Random-Regular (RR)	3	11.8	11.9±0.26	0.66±0.08
Erdös-Rényi	3	9.45	20.5±0.23	0.68±0.08
Cayley-Tree	3	10	11.44±0.06	0.51±0.045
Cayley-Tree with loops	3.05	10	12.4±0.1	0.54±0.075
RR "double peak"	3.1	10.28	14.1±0.3	0.85±0.41

Table 9.1.: Networks showing the localization transition. The value of l is for $N = 1000$.

9.2.3. Results

The calculations for all networks mentioned above are performed for M different realizations, where $M = 1000, 400, 200, \ldots, 50$ for the corresponding number of nodes: $N = 200, 500, 1000, \ldots, 4000$. Except for the Cayley-tree networks for which $M = 4000, 2000, 1000, \ldots, 125, 64$ for the corresponding tree sizes: $N = 63, 127, 255, \ldots, 2047, 4095$ or $L = 6, 7, 8, \ldots, 11, 12$ (where L is the number of "generations" of the tree). Another exception is for Erdös-Rényi graphs in which $\langle k \rangle$ is between 3 and 3.5. The low connectivity of the graphs, results in one main cluster and relatively large number of not-connected nodes (about 5%). Thus, the calculations are made only for the largest cluster of each realization, since a procedure that considers all the nodes is skewed by the eigenvalues of small disconnected clusters [24]. A clear localization transition is observed for a group of graphs which are all characterized by an average degree $\langle k \rangle$ smaller than 3.1, and an averaged last occupied shell l (for $N = 1000$ sites) larger or equal to 9.45. The results are summarized in Table 9.1.

The results for all the graphs (including those which show no clear signs of transition) can be scaled according to their average degree $\langle k \rangle$. The higher the value of $\langle k \rangle$ is - the higher is the value of W needed in order to obtain a specific value of γ. Thus, the higher the average degree, the more metallic the system is, which makes sense. A cross section at $\gamma = 0.6$ of all curves is shown in Fig. 9.5 as a function of $\langle k \rangle$. The $\langle k \rangle$ of the networks studied in Fig. 9.5 as well as the averaged last occupied shell l for $N = 1000$ sites are presented in Table 9.2.

9.2.4. Observations

The following observations can be gleaned out of the data for the different networks:
(1) For all the networks that show a metal-insulator transition, ν is of order $1/2$ except for the

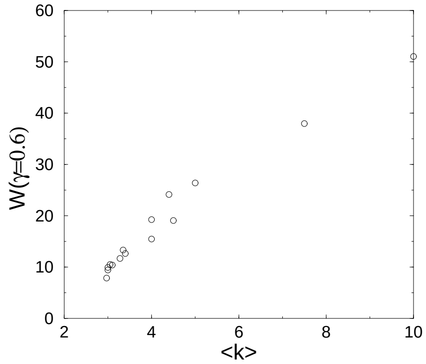

Figure 9.5.: The γ curves of the checked networks can be ordered by their $\langle k \rangle$. The values of their $W(\gamma = 0.6)$ are presented as a function of $\langle k \rangle$. One can notice the increasing W with $\langle k \rangle$.

Network	$\langle k \rangle$	l (for $N = 1000$)
Scale-Free , $\lambda = 4$, $m = 2$	2.97	12.46
Random-Regular	3	11.8
Random-Regular "double peak" ($p = 0.95 \to k = 3$, $p = 0.05 \to k = 5$)	3.1	10.28
Cayley-Tree	3	10
Cayley-Tree with loops	3.05	10
Erdös-Rényi	3	9.45
Scale-Free , $\lambda = 3.5$, $m = 2$	3.28	9.36
Erdös-Rényi	3.1	9.31
Erdös-Rényi	3.2	9.03
Random-Regular "double peak" ($p = 0.8 \to k = 3$, $p = 0.2 \to k = 5$)	3.4	9
Erdös-Rényi	3.5	8.33
Random-Regular "double peak" ($p = 0.95 \to k = 3$, $p = 0.05 \to k = 10$)	3.35	7.99
Erdös-Rényi	4	7.51
Scale-Free , $\lambda = 5$, $m = 3$	4	7.37
Scale-Free , $\lambda = 4$, $m = 3$	4.5	6.05
Random-Regular "double peak" ($p = 0.8 \to k = 3$, $p = 0.2 \to k = 10$)	4.4	6.13
Erdös-Rényi	5	6.31
Erdös-Rényi	7.5	5.02
Erdös-Rényi	10	4.1

Table 9.2.: The average connectivity $\langle k \rangle$ of all the networks considered in this study, as well as the averaged last occupied shell l for $N = 1000$ sites

Random-Regular "double-peak" network which is the one with the highest value of connectivity that still shows a clear transition. A critical index of $\nu = 0.5$ is expected for a system of infinite dimensionality. At $\langle k \rangle = 3.1$ the value of ν is significantly higher, but so is the estimate of the error bar. On the other hand for the Erdös-Rényi graph with $\langle k \rangle = 3.1$ no clear transition is observed.
(2) All networks with connectivity above 3.1 do not show clear signs of a metal-insulator transition. Nevertheless, one should be rather careful in interpreting this observation since, as is clear from Table 9.2, larger values of $\langle k \rangle$ lead to smaller size, l, of the network for the same number of nodes. Moreover, from the two networks which have the same $\langle k \rangle = 3.1$, only the one with the higher value of l shows clear signs of the metal insulator transition. Thus, the absence of transition may be an artifact of the small size of networks with high average connectivity.
(3) The critical disorder W_c fluctuates in the range of $12 - 20$ (Table 9.2). Due to the small range of $\langle k \rangle$ $(2.97 - 3.1)$, it is hard to determine any relation between k and W_c.
(4) On the other hand, there is a clear relation between the amount of disorder needed in order to reach a particular value of γ (i. e., the value of W needed to reach a certain degree of localization) and $\langle k \rangle$. As can be seen in Fig. 9.5, a linear dependence $W(\gamma = 0.6) \propto \langle k \rangle$ is observed.

9.2.5. Discussion

Thus, the gross features of the Anderson metal-insulator transition are similar for a wide range of different networks. The critical index for all the networks studied here are within the range expected for a system of infinite dimensionality, and the connectivity influences the degree of localization. On the other hand, the fact that networks with high connectivity are very compact raises the problem of identifying the transition point. It is hard to extend the usual finite-size scaling method to networks with high connectivity since the number of sites grows very rapidly with size, while for small network sizes the crossover behavior of the γ curves is very noisy. This results in an inability to clearly identify the Anderson transition, although it can not be ruled out the possibility that there is a critical connectivity for complex networks above which no transition exist.

It is also worthwhile to add a general comment on the statistical method we have used in order to identify the transition. The Anderson transition is one of the best known examples of a quantum phase transition. Non-analyticities of the free energy is the clearest sign for a classical phase transitions. One would expect that for quantum phase transitions the free energy will be replaced by the ground state energy. Surprisingly this is not the case for the Anderson transition, since only the ground state wave function, not the the ground state energy exhibit a signature of the transition. Traditionally, numerically identifying the phase transition was performed by calculating the conductance or transmission through the system, which directly probes the properties of the wave functions.

Later it has been realized by Shklovskii and his coworkers [183] that although the ground state energy does not contain information regarding the phase transition, statistical properties of the single-electron electrons encode such information. As we explained in the previous sections the statistics of the energy spacings can be used to identify the transition and study its properties.

Recently it was realized that information entropy can also be used as a tool to identify a quantum phase transition, even for the Anderson transition [116]. Constructing a density matrix of some part A of the system ρ_A by tracing out all other degrees of freedom , one may define the von Neumann entropy of the system $S_A = -Tr(\rho_A \ln \rho_A)$. Averaging over different parts and realizations of disorder, one can use finite size scaling in a similar fashion to the one described for the spacing statistics to colaps the singular part of the entropy on two branches in a similar fashion to the one depicted in Fig. 9.4. Thus, the von Neumann entropy may be used as an additional method to identify the Anderson transition for complex networks and could be used to augment the statistical methods described in this chapter.

9.3. Complex networks with high clustering

As introduced in the last sections it is possible to study quantum phase transition by analyzing the spectrum of an Anderson model [9, 119] representing the complex network. The transition was obtained in Sect. 9.2.2 by introducing diagonal (on-site) disorder [167]. Alternative approaches would be non-diagonal (bond) disorder or percolation, i. e. removing some fraction of all sites or bonds. In this case a classical transition [135] in which the infinite cluster breaks into finite pieces is found after the quantum phase transition [24]. Anderson and quantum percolation transitions, which seem to be in the same universality class, have been studied on different topologies including fractal structures [170], Cayley trees [166], and complex networks [47, 167]. In all cases, the transitions were induced either by on-site disorder or by cutting bonds (percolation) and thus changing the degree distribution of the network [47].

In this section we want to show that it is possible to observe quantum and classical phase transitions by a mere topological change of the network. Even for zero disorder and unchanged degree distribution we find a quantum phase transition by increasing the clustering of the network. Most of the results in this section have been published in [100].

9.3.1. Clustering

Complex networks have additional degrees of freedoms compared with standard lattices. The basic property of a network is its degree distribution $P(k)$ which defines the type of network. Some examples were discussed in Sect. 9.2.1. A property related to the degree distribution is the diameter d or the characteristic path length ℓ between two arbitrary nodes (small-world property) of the system. These are important global properties, but in real-world network one also observe local degrees of freedom [4, 57, 162]. Two of the most important ones are clustering and assortativity [157]. The latter describes the degree-degree correlation of the network. Although the assortativity is definitely an interesting subject we will focus on the effect of clustering. To prevent interference between both we keep the degree-degree correlation as low as possible.

Clustering measures the cliquishness of a typical neighborhood and was introduced in the study of 'small-world' networks [212]. Regular non-random networks with constant degree have high clustering and a large diameter comparable to standard lattices. When a fraction of the links is reconnected randomly the diameter and the clustering drop. A completely random network has nearly zero clustering. On the other hand, real-world networks exhibit high clustering indicating the presence of many loops on short length scales [4, 57, 162].

Quantitatively clustering can be defined as the probability of triadic closure, $C_i = 2T_i/[k_i(k_i - 1)]$ [212], where T_i is the number of triangles passing through vertex i and k_i is its degree. Although clustering is a local quantity a global measure C can be achieved by averaging over C_i. A global C cannot capture specific aspects of the network, e.g. varying degree-degree correlations can lead to networks with different topology but similar C [177, 175, 176]. On the other hand the fully local C_i is hard to analyze. Therefore it was suggested to average C_i within each degree class, yielding $\bar{C}(k)$[207].

It is not possible to achieve all possible functional dependences of $\bar{C}(k)$ with k. To achieve high clustering of the higher degrees the assortativity of the network has to be strong. When

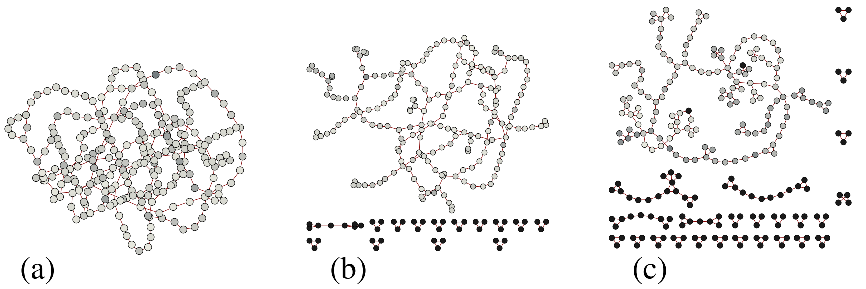

Figure 9.6.: Representative pictures of scale-free networks ($\lambda = 5$) (a) without and (b,c) with clustering ($C_0 = 0.4, 0.6$). All three networks have the same size of $N = 250$. The giant component has a size of (a) $N_g = 250$, (b) $N_g = 203$, and (c) $N_g = 145$. The actual global clustering coefficient is (a) $C = 8 \times 10^{-4}$, (b) $C = 0.34$, and (c) $C = 0.53$. The global clustering coefficient of the giant component is (b) $C_g = 0.10$ and (c) $C_g = 0.17$. The logarithmically scaled gray scales presents the intensity of a mode with $E \approx 0.45$, light gray indicating the highest and black the lowest probability

nodes with large degrees are connected to nodes with lower degrees they can not achieve a high clustering because the nodes with lower degrees do not have enough connections to participate in a large number of triangles. Depending on the strength of the degree-degree correlation one finds an upper limit which can be approximated by

$$\bar{C}(k) = C_0(k-1)^{-\alpha}, \tag{9.11}$$

with α between 1 for no and 0 for high assortativity. Because we want to study a phase transition induced by clustering we want to keep the assortativity as low as possible. Therefore we will restrict ourselves to $\alpha = 1$. An explicit linear dependence between C and C_0 exists and variation of C_0 between 0 (no clustering) and 1 (maximum clustering) are unambiguous. The connection between the global clustering coefficient C and C_0 is a constant Δ which only depends on λ, $C = C_0\Delta(\lambda)$ with $\Delta = \sum_{k=m}^{K}(k-1)P(k)$. It is possible to write Δ using the basic parameters (m, K, λ, N), using (9.8) and the paragraph following.

We apply an algorithm suggested recently by Serrano and Boguñá [174] to generate scale-free networks with tunable degree distribution $P(k) \sim k^{-\lambda}$ (9.8) and $\bar{C}(k)$. In Fig. 9.6(a)-(c) we show three representative pictures of scale-free networks as a result of the algorithm. They all have the same number of nodes with a rising C_0 from left to right. One sees clearly that for higher clustering more and more nodes disintegrate from the giant component. The reason is that for nodes with low degree it is easier to achieve higher clustering in some small clusters. For example nodes with a degree of two can achieve the highest clustering in triangles.

In Fig. 9.7(a) and (b) we show the degree distribution $P(k)$ and the degree dependent clustering coefficient $\bar{C}(k)$, respectively. The lines are the theoretical values which were demanded. The circles correspond to results of the full network and the squares to results of the giant component. While the degree distribution is quite stable when going from the full system to the giant component, the clustering changes for all degrees drastically. It drops by at least a factor of two.

A metal-insulator transition is well defined only on the giant component since the other clusters do not grow with system size. In the language of percolation it is the infinite cluster because it becomes infinite for an infinite system size while the small clusters remain finite. Therefore a localized state and an extended state are unambiguously defined only on the giant component.

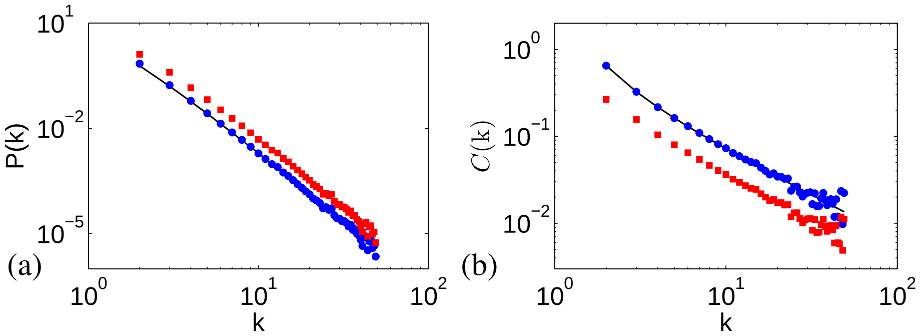

Figure 9.7.: (a) degree distribution $P(k)$ and (b) clustering coefficients $\bar{C}(k)$ for scale-free networks with $\lambda = 4$ [line in (a)], $C_0 = 0.65$ [line in (b) according to (9.11)] and $N = 15000$ nodes, averaged over 120 configurations. Circles for distributions regarding the whole network and squares for the giant component (with $\langle N_1 \rangle = 11906$ nodes; shifted vertically by a factor of 2 for degree distribution)

For the finite components a localized state with a localization length larger than the system size can not be distinguish from an extended state.

Since the clustering of the giant component C_g differs from that of the full network C it is a priori not clear which of them is a good order parameter for the transition. The ambiguity can be resolved by analyzing the functional dependence of C_0 with the average clustering coefficient of the full network C and its giant component C_g. An illustrative results is shown in Fig. 9.8. Not only C is linearly dependent on C_0 but also C_g if $C_0 \leq 0.9$. We find no system size dependence which is important because we want to use a finite size scaling formalism to analyze the phase transition. Values for $C_0 \geq 0.85$ should be treated with care because the algorithm fails to achieve such high clustering. Due to the linear dependence of all three versions of clustering coefficient they are interchangeable. In the following, we will use the parameter C_0 instead of C or $\bar{C}(k)$.

The results shown in Fig. 9.8 are also a good measure for the quality of the algorithm. The black line is the theoretically achievable clustering with the given C_0. The algorithm does not achieve the theoretically possible clustering but is very near this value. But still a linear dependence holds for C and C_0, which is more important. In the inset the gradient of the linear dependence Δ is shown for different power-law exponent λ. One sees that for all λ the algorithm does not achieve the theoretically possible clustering. Interestingly Δ for the clustering dependence of the giant component is nearly constant.

We obtained similar, however less reliable, results when generating networks with the algorithm of Volz [209] fixing C instead of $\bar{C}(k)$. The problem of this algorithm is that it is not possible to control the assortativity. Therefore when C is changed also the assortativity changes making it difficult to judge whether both networks are comparable.

Since each triangle represents a very short loop in the network, waves in networks with high clustering will have a high probability to return to the same node and to interfere. Since such interferences are the main reason for quantum localization, one may expect that strong clustering will induce localization.

9.3.2. Results

To analyze the metal-insulator transition for networks with clustering we use the formalism as introduced in 9.1.3. We study scale-free networks with various λ and C_0. The eigenvalues and

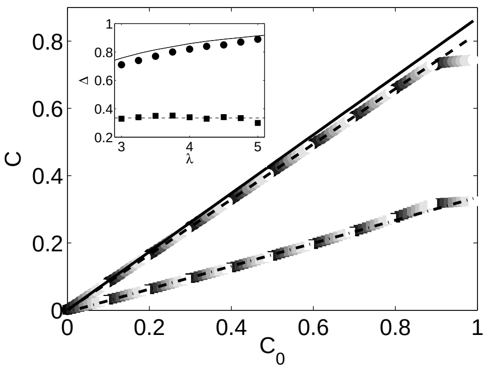

Figure 9.8.: Test of the relation $C = C_0\Delta(\lambda)$ for a scale-free network with $\lambda = 4$ and $m = 2$. The black line is the ideal curve. The circles (squares) are results for the full network (giant component). The different gray scales represent different system sizes from $N = 2000$ (black) to $N = 20000$ (white). The dashed (dashed dotted) line is a linear fit for the full network (giant component). Inset: Results of the fits for $\Delta(\lambda)$. Line is the ideal curve. The circles (squares) are the results for the full network (giant component). The dashed line is the mean of Δ for the giant component with $\langle\Delta\rangle = 0.34$.

eigenvectors are calculated by exact diagonalisation of the Hamiltonian (9.4). Figures 9.6(a-c) show the intensities corresponding to three eigenmodes. For all three cases the state is extended on the whole giant component and not present on the finite clusters.

To extract the critical clustering $C_{0,q}$, the critical disorder W_c, and critical exponent ν we have to extend (9.10) to also include C_0. As in the case for the disorder W we expect from finite-size scaling arguments [183] that γ around $C_{0,q}$ will behave exactly as around W_c,

$$\begin{aligned} \gamma(C_0, W, L) &= \gamma(C_{0,q}, W_c, L) + \\ &\quad \left[R_1|C_0 - C_{0,q}| + R_2|W - W_c|\right] L^{1/\nu}, \end{aligned} \tag{9.12}$$

where R_1 and R_2 are constants and $L \propto \ln(a(C_0)N)$ [1]. Using (9.12) we have determined $C_{0,q}$ and W_c for scale-free networks with various λ. We also checked that equivalent results are obtained if other integral measures of $P(s)$ are studied, e.g., $I_0 = \frac{1}{2}\int_0^\infty s^2 P(s)\, ds$.

To convince the reader that clustering indeed induces a phase transition we show in Fig. 9.9 the level spacing distribution $P(s)$ of a large scale-free network without disorder ($W = 0$) but varied C_0, as well the two limiting cases $P_\mathrm{W}(s)$ and $P_\mathrm{P}(s)$. One can clearly see that the shape of $P(s)$ changes from Wigner to Poisson with increasing C_0. Comparing Fig. 9.9 with Fig. 9.2 one finds no deviation from the typical behavior known from disorder. We thus observe an Anderson-like transition although there are no disorder W and no changes in the degree distribution $P(k)$. The inset of Fig. 9.9 shows γ for five system sizes versus the clustering strength C_0. One can observe the quantum phase transition at the critical value $C_{0,q} \approx 0.69$ by the crossing of the five curves, indicating a system-size independent critical value of $\gamma_c \approx 0.76$.

The phase diagram for the transition from localized (upper right) to extended (lower left) optical modes is shown in Fig. 9.10(a). The horizontal axis ($C_0 = 0$) corresponds to the case with no clustering studied before in Sect. 9.2.2, where the critical disorder W_c depends on λ. The main new finding of the present study regards the transitions on the vertical axis. Without disorder,

---

[1] The N dependence is well established [48] but the C_0 dependence seems to be unexplored. Our data for N up to 10^5 suggest $\ln a \propto (C_0 - C_{0,c})^{-\nu_c}$. Since $C_{0,q} < C_{0,c}$, a and thus L depend weakly on C_0 at the quantum transition.

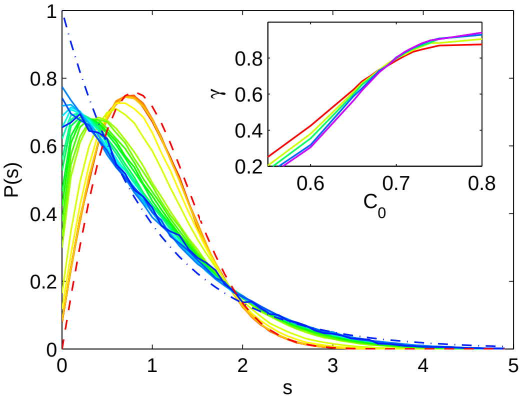

Figure 9.9.: Level spacing distribution $P(s)$ for optical modes on scale-free networks with $\lambda = 5$, $N = 12500$ and no disorder, $W = 0$. A clear transition from Wigner (dashed curve) to Poisson (dash-dotted curve) behavior is observed as a function of the clustering coefficient prefactor that is increased from $C_0 = 0.0$ (continuous red curve; light gray curve nearest to dashed curve) to $C_0 = 0.90$ (continuous blue curve; dark gray curve nearest to dashed dotted curve). Inset: localization parameter γ [see (9.9)] versus C_0 for networks with $N = 5000$ (red), $N = 7500$ (light green), $N = 10000$ (green) , $N = 12500$ (blue), and $N = 15000$ (purple). A transition from extended modes for small C_0 to localized modes for large C_0 is observed at $C_{0,q} \approx 0.69$. The results are based on eigenvalues around $|E| = 0.2$ and 0.5 (taken from [100])

the transition to the localized phase occurs at a critical clustering $C_{0,q}$ that depend on λ, i. e., the degree distribution. While even the strongest clustering $C_0 = 1$ cannot achieve such a transition if $\lambda < 4$, values of $C_{0,q} < 1$ are observed for $\lambda > 4$. The case $\lambda = 4$ seems to be limiting: this is the broadest degree distribution which allows a quantum phase transition upon increasing clustering.

If variations of C_0 and W are considered, the full phase diagram can be explored. Evidently, smaller values of C_0 are sufficient for quantum phase transitions if $W > 0$. Within our error bars the critical exponent ν corresponds to the mean-field value $\nu = 0.5$ for infinite dimensions (see Fig. 9.10(b)) as expected from the Anderson transition [65]. We obtained similar phase diagrams for networks with homogeneous or Erdös-Renyi-type degree distributions (not shown).

There are some similarities between the phase transition induced by clustering and quantum percolation. In both cases the giant component becomes smaller for larger values of the order parameters. We also find a classical phase transition after the quantum phase transition. The relation between both types of transitions is still an open question. The changes in the degree distribution of the giant component are not sufficient to explain the classical transition.

To make sure that the quantum transition is induced by clustering and not by a classical phase transition we determine the corresponding classical critical clustering coefficient $C_{0,c}$. For that we have analyzed the size N_2 of the second largest cluster in the system which should increase with C_0 if the giant component exists ($C_0 < C_{0,c}$) and decrease for higher values of C_0 if it broke down ($C_0 > C_{0,c}$) [47]. We find no indications of a classical transition for $\lambda < 4.5$, i. e. the giant component is not broken. For $\lambda = 5$ we find $C_{0,c} \approx 0.85$, significantly larger than $C_{0,q} \approx 0.69$ [see insets of Fig. 9.9 and Fig. 9.10(c)]. We thus conclude that the quantum transition for $W = 0$ is clearly different from the classical one in two ways: (i) there is no classical transition between $4 < \lambda < 4.5$ although a quantum transition is clearly seen, and (ii) for $\lambda > 4.5$, the quantum transition occurs for lower C_0 values than the classical one. This leaves an intermediate regime

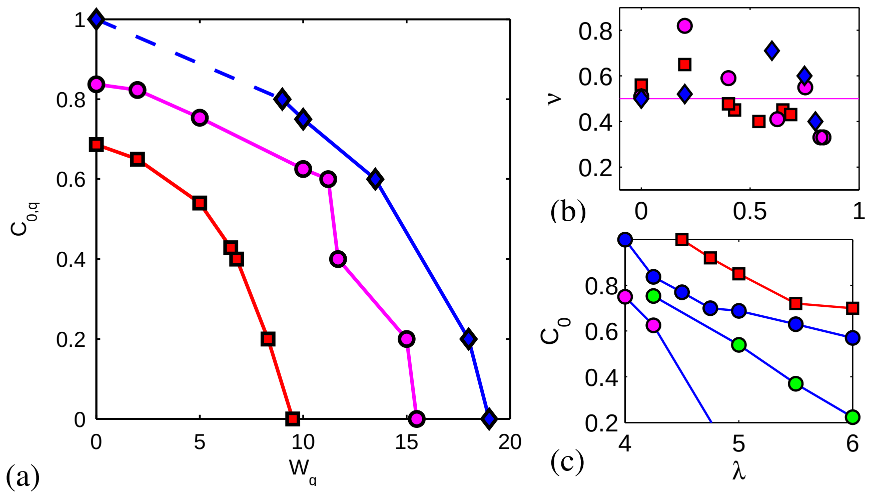

Figure 9.10.: (a) Phase diagram for transitions from localized optical modes (upper right) to extended modes in parts of the spectrum (lower left) for different degree distribution exponents λ, $\lambda = 4$ (blue diamonds), 4.25 (pink circles), and 5 (red squares). Data for $C_0 > 0.9$ are not reliable for network generation reasons, and the error bar for the point at $C_0 = 1$ is about 0.1. (b) Exponent ν for different λ and $C_{0,q}$. The values are, within the error bars (not shown), consistent with the mean-field prediction $\nu = 0.5$. (c) Quantum transitions without disorder (blue circles) and classical transitions (red squares) as a function of the degree exponent λ. In the regime $4 < \lambda < 4.5$ only quantum transitions occur. For $W > 0$ the curves move downwards making quantum transitions possible for $\lambda < 4$ (green circles for $W = 5$ and pink circles for $W = 10$). The figures are taken from [100]

($C_{0,q} < C_0 < C_{0,c} \leq 1$) in which all modes are localized although there is a spanning giant cluster.

9.4. Summary

In summary, we have shown that quantum phase transitions of wave-like modes (similar to the Anderson transition and to the quantum percolation transition) can be obtained in a complex network without introducing on-site disorder or bond disorder or tampering with the degree distribution (i. e. the number and distribution of links). One only needs to change the clustering coefficient of the network, which corresponds to a rewiring procedure.

We conclude that clustering represents a new degree of freedom that can be used to induce and study phase transitions in complex networks. Comparing systems with different clustering properties might enable one to find the most relevant cause of quantum localization. We propose that the phenomenon should be observable experimentally and relevant in complex coherent optical networks made of fibers and beam splitters. Such experiments will directly probe the influence of complex network topology on the Anderson localization of light [215, 197, 127, 172].

Bibliography

[1] E. Abrahams, P. Anderson, D. Licciardello, and T. Ramakrishnan. Scaling theory of localization – absence of quantum diffusion in 2 dimensions. Phys. Rev. Lett. **42**, 673 (1979)

[2] M. Abramowitz and I. A. Stegun (editors). *Handbook of mathematical functions with formulas, graphs, and mathematical tables* (Dover Publications, 1972)

[3] R. Aharonov and D. Bohm. Significance of electromagnetic potentials in the quantum theory. Phys. Rev. **115**, 485 (1959)

[4] R. Albert and A. L. Barabási. Statistical mechanics of complex networks. Rev. Mod. Phys. **74**, 47 (2002)

[5] R. Albert, H. Jeong, and A. L. Barabási. Error attack tolerance of complex networks. Nature **406**, 378 (2000)

[6] B. L. Altshuler and B. I. Shklovskii. Repulsion of energy-levels and the conductance of small metallic samples. Sov. Phys. JETP **64**, 127 (1986)

[7] B. L. Altshuler, I. K. Zharekeshev, S. A. Kotochigova, and B. I. Shklovskii. Energy-level repulsion and the metal-insulator-transition. Sov. Phys. JETP **67**, 625 (1988)

[8] P. Anderson, D. Thouless, E. Abrahams, and D. Fisher. New method for a scaling theory of localization. Phys. Rev. B **22**, 3519 (1980)

[9] P. W. Anderson. Absence of diffusion in certain random lattices. Phys. Rev. **109**, 1492 (1958)

[10] T. Antal, I. Bena, M. Droz, K. Martens, and Z. Racz. Guiding fields for phase separation: controlling Liesegang patterns. Phys. Rev. E **76**, 046203 (2007)

[11] T. Antal, M. Droz, J. Magnin, A. Pekalski, and Z. Racz. Formation of Liesegang patterns: Simulations using a kinetic Ising model. J. Chem. Phys. **114**, 3770 (2001)

[12] T. Antal, M. Droz, J. Magnin, and Z. Racz. Formation of Liesegang patterns: a spinodal decomposition scenario. Phys. Rev. Lett. **83**, 2880 (1999)

[13] T. Antal, M. Droz, J. Magnin, Z. Racz, and M. Zrinyi. Derivation of the Matalon-Packter law for Liesegang patterns. J. Chem. Phys. **109**, 9479 (1998)

[14] D. Avnir and M. Kagan. Spatial structures generated by chemical reactions at interfaces. Nature **307**, 717 (1984)

[15] P. Ball. *The self-made tapestry: pattern formation in nature* (Oxford University Press, 2001)

[16] A. Barabási and R. Albert. Emergence of scaling in random networks. Science **286**, 509 (1999)

[17] M. Batsch, L. Schweitzer, I. K. Zharekeshev, and B. Kramer. Crossover from critical orthogonal to critical unitary statistics at the Anderson transition. Phys. Rev. Lett. **77**, 1552 (1996)

[18] D. Belitz. Theory of Anderson localization in weak magnetic-fields. Solid State Commun. **52**, 989 (1984)

[19] D. Belitz and T. Kirkpatrick. The Anderson-Mott transition. Rev. Mod. Phys. **66**, 261 (1994)

[20] I. Bena, F. Coppex, M. Droz, and Z. Racz. Front motion in an $A + B \to C$ type reaction-diffusion process: effects of an electric field. J. Chem. Phys. **122**, 024512 (2005)

[21] I. Bena, M. Droz, I. Lagzi, K. Martens, Z. Racz, and A. Volford. Designer patterns: flexible control of precipitation through electric currents. Phys. Rev. Lett. **101**, 075701 (2008)

[22] I. Bena, M. Droz, and Z. Racz. Formation of Liesegang patterns in the presence of an electric field. J. Chem. Phys. **122**, 204502 (2005)

[23] I. T. Bensemann, M. Fialkowski, and B. A. Grzybowski. Wet stamping of microscale periodic precipitation patterns. J. Phys. Chem. B **109**, 2774 (2005)

[24] R. Berkovits and Y. Avishai. Spectral statistics near the quantum percolation threshold. Phys. Rev. B **53**, R16125 (1996)

[25] J. Billy, V. Josse, Z. Zuo, A. Bernard, B. Hambrecht, P. Lugan, D. Clément, L. Sanchez-Palencia, P. Bouyer, and A. Aspect. Direct observation of Anderson localization of matter waves in a controlled disorder. Nature **453**, 891 (2008)

[26] B. Bollobas and O. Riordan. *Handboook of graphs and networks: mathematical results on scale-free random graphs* (Wiley-VCH Berlin, 2002)

[27] D. Braun, G. Montambaux, and M. Pascaud. Boundary conditions at the mobility edge. Phys. Rev. Lett. **81**, 1062 (1998)

[28] A. Buki, E. Karpatismidroczki, and M. Zrinyi. Computer simulation of regular Liesegang structures. J. Chem. Phys. **103**, 10387 (1995)

[29] A. Bunde and S. Havlin (editors). *Fractals and disordered systems* (Springer Berlin, 1996)

[30] J. W. Cahn. On spinodal decomposition. Acta Metall. **9**, 795 (1961)

[31] J. W. Cahn and J. E. Hilliard. Free energy of a nonuniform system. I. Interfacial free energy. J. Chem. Phys. **28**, 258 (1958)

[32] R. Cain, A. Römer, and M. Schreiber. Phase diagram of the three-dimensional Anderson model of localization with random hopping. Ann. Phys. (Leipzig) **8**, SI33 (1999)

[33] S. Carmi, S. Havlin, S. Kirkpatrick, Y. Shavitt, and E. Shir. A model of Internet topology using k-shell decomposition. PNAS **104**, 11150 (2007)

[34] C. Castellani, C. DiCastro, and L. Peliti. On the upper critical dimension in Anderson localization. J. Phys. A **19**, 1099 (1986)

[35] C. Castellani and G. Kotliar. The magnetic-field crossover exponent problem revisited. Physica A **167**, 294 (1990)

[36] V. Castets, E. Dulos, J. Boissonade, and P. Dekepper. Experimental evidence of a sustained standing Turing-type non-equilibrium chemical pattern. Phys. Rev. Lett. **64**, 2953 (1990)

[37] M. Chacron and I. L'Heureux. A new model of periodic precipitation incorporating nucleation, growth and ripening. Phys. Lett. A **263**, 70 (1999)

[38] I. Chang, Z. Lev, Y. Meir, A. B. Harris, J. Adler, and A. Aharony. Localization length exponent in quantum percolation. Phys. Rev. Lett. **74**, 2094 (1995)

[39] A. C. Chatterji and N. R. Dahr. Das Liesegang'sche Phänomen und Niederschlagsbildung. Kolloid-Z. **31**, 15 (1922)

[40] D. S. Chernavskii, A. A. Polezhaev, and S. C. Müller. A model of pattern formation by precipitation. Physica D **54**, 160 (1991)

[41] B. Chopard and M. Droz. Cellular automata model for the diffusion equation. J. Stat. Phys. **64**, 859 (1991)

[42] B. Chopard and M. Droz. Microscopic study of the properties of the reaction front in an $A + B \to C$ reaction-diffusion process. Europhys. Lett. **15**, 459 (1991)

[43] B. Chopard, M. Droz, J. Magnin, Z. Racz, and M. Zrinyi. Liesegang patterns: Effect of dissociation of the invading electrolyte. J. Phys. Chem. A **103**, 1432 (1999)

[44] B. Chopard, P. Luthi, and M. Droz. Microscopic approach to the formation of Liesegang patterns. J. Stat. Phys. **76**, 661 (1994)

[45] B. Chopard, P. Luthi, and M. Droz. Reaction-diffusion cellular automata model for the formation of Leisegang patterns. Phys. Rev. Lett. **72**, 1384 (1994)

[46] R. Cohen, D. ben Avraham, and S. Havlin. Perclation critical exponents in scale-free networks. Phys. Rev. E **66**, 036113 (2002)

[47] R. Cohen, K. Erez, D. ben Avraham, and S. Havlin. Resilience of the Internet to random breakdowns. Phys. Rev. Lett. **85**, 4626 (2000)

[48] R. Cohen and S. Havlin. Scale-free networks are ultrasmall. Phys. Rev. Lett. **90**, 058701 (2003)

[49] S. Cornell, M. Droz, and B. Chopard. Role of fluctuations for inhomogeneous reaction-diffusion phenomena. Phys. Rev. A **44**, 4826 (1991)

[50] J. Crank. *The mathematics of diffusion* (Oxford Science Publications, 1996)

[51] M. C. Cross and P. C. Hohenberg. Pattern formation outside of equilibrium. Rev. Mod. Phys. **65**, 851 (1993)

[52] G. Czycholl. *Theoretische Festkörperphysik* (Springer Berlin, 2004)

[53] N. R. Dahr and A. C. Chatterji. Studies on the formation of periodic precipitates. II. J. Phys. Chem. **28**, 41 (1924)

[54] I. Dasgupta, T. Saha, and A. Mookerjee. Analysis of stochastic resonances in a two-dimensional quantum percolation model. Phys. Rev. B **47**, 3097 (1993)

[55] G. T. Dee. Patterns produced by precipitation at a moving reaction front. Phys. Rev. Lett. **57**, 275 (1986)

[56] C. Domb and J. L. Lebowitz (editors). *Phase transition and critical phenomena* (Academic Press London, 1982)

[57] S. N. Dorogovtsev and J. F. F. Mendes. *Evolution of networks: from biological nets to the Internet and WWW* (Oxford University Press, 2003)

[58] T. Dröse, M. Batsch, I. K. Zharekeshev, and B. Kramer. Phase diagram of localization in a magnetic field. Phys. Rev. B **57**, 37 (1998)

[59] M. Droz. Recent theoretical developments on the formation of Liesegang patterns. J. Stat. Phys. **101**, 509 (2000)

[60] M. Droz, J. Magnin, and M. Zrinyi. Liesegang patterns: Studies on the width law. J. Chem. Phys. **110**, 9618 (1999)

[61] M. Droz, Z. Racz, and J. Schmidt. One-dimensional kinetic Ising model with competing dynamics: steady-state correlations and relaxation times. Phys. Rev. A **39**, 2141 (1989)

[62] F. J. Dyson. Statistical theory of the energy levels of complex systems. J. Math. Phys. **3**, 140 (1962)

[63] I. Edrei, M. Kaveh, and B. Shapiro. Probability distribution functions for transmission of waves through random media: A new numerical method. Phys. Rev. Lett **62**, 2120 (1989)

[64] K. B. Efetov. Supersymmetry and theory of disordered metals. Adv. Phys. **32**, 53 (1983)

[65] K. B. Efetov. Anderson metal-insulator transition in a system of metal granules: existence of a minimum metallic conductivity and a maximum dielectric constant. Sov. Phys. JETP **61**, 606 (1985)

[66] A. Einstein. Über die von der molekularkinetischen Theorie der Wärme geforderte Bewegung von in ruhenden Flüssigkeiten suspendierten Teilchen. Ann. Phys. (Leipzig) **17**, 549 (1905)

[67] P. Erdös and A. Rényi. On Random Graphs. Publ. Math. Debrecen **6**, 290 (1959)

[68] R. Feeney, S. L. Schmidt, P. Strickholm, J. Chadam, and P. Ortoleva. Periodic precipitation and coarsening waves: applications of the competitive particle growth model. J. Chem. Phys. **78**, 1293 (1983)

[69] M. Fialkowski, A. Bitner, and B. A. Grzybowski. Wave optics of Liesegang rings. Phys. Rev. Lett. **94**, 018303 (2005)

[70] S. B. Field and T. F. Rosenbaum. Critical behavior of the Hall conductivity at the metal-insulator transition. Phys. Rev. Lett. **55**, 522 (1985)

[71] M. Flicker and J. Ross. Mechanism of chemical instability for periodic precipitation phenomenon. J. Chem. Phys. **60**, 3458 (1974)

[72] M. Foret, E. Courtens, R. Vacher, and J.-B. Suck. Scattering investigation of acoustic localization in fused silica. Phys. Rev. Lett. **77**, 3831 (1996)

[73] L. Galfi and Z. Racz. Properties of the reaction front in an $A + B \rightarrow C$ type reaction-diffusion process. Phys. Rev. A **38**, 3151 (1988)

[74] L. Gammaitoni, P. Hänggi, P. Jung, and F. Marchesoni. Stochastic resonance. Rev. Mod. Phys. **70**, 223 (1998)

[75] J. George and G. Varghese. Formation of periodic precipitation patterns: a moving boundary problem. Chem. Phys. Lett. **362**, 8 (2002)

[76] J. George and G. Varghese. Intermediate colloidal formation and the varying width of periodic precipitation bands in reaction-diffusion systems. J. Colloid Interface Sci. **282**, 397 (2005)

[77] O. Giraldo, S. L. Brock, M. Marquez, S. L. Suib, H. Hillhouse, and M. Tsapatsis. Spontaneous formation of inorganic helices. Nature **405**, 38 (2000)

[78] O. Giraldo, J. P. Durand, H. Ramanan, K. Laubernds, S. L. Suib, M. Tsapatsis, S. L. Brock, and M. Marquez. Dynamic organization of inorganic nanoparticles into periodic micrometer-scale patterns. Angew. Chem. Int. Ed. **42**, 2905 (2003)

[79] O. Giraud, B. Georgeot, and D. Shepelyansky. Computing of delocalization in small-world networks. Phys. Rev. E **72**, 036203 (2005)

[80] R. J. Glauber. Time-dependent statistics of the Ising model. J. Math. Phys. **4**, 294 (1963)

[81] L. Gong and P. Tong. von Neumann entropy and localization-delocalization transition of electron States in Quantum Small-World Networks. Phys. Rev. E **74**, 056103 (2006)

[82] B. A. Grzybowski, K. J. M. Bishop, C. J. Campbell, M. Fialkowski, and S. K. Smoukov. Micro- and nanotechnology via reaction-diffusion. Soft Matter **1**, 114 (2005)

[83] T. Guhr, A. Müller-Groeling, and H. A. Weidenmüller. Random-matrix theories in quantum physics: common concepts. Phys. Rep. **299**, 189 (1998)

[84] J. D. Gunton and M. Droz. *Introduction to the theory of metastable and unstable states* (Springer Berlin, 1983)

[85] H. Henisch. *Crystals in gels and Liesegang rings* (Cambridge University Press, 1988)

[86] M. Henneke, B. Kramer, and T. Ohtsuki. Anderson transition in a strong magnetic field. Europhys. Lett. **27**, 389 (1994)

[87] M. J. Hirsh, U. Thomanschefsky, and D. F. Holcomb. Critical behavior of the zero-temperature conductivity in compensated silicon, Si:(P,B). Phys. Rev. B. **37**, 8257 (1988)

[88] K. H. Hoffmann and M. Schreiber (editors). *Computational statistical physics. From billiards to Monte Carlo* (Springer Berlin, 2002)

[89] D. R. Hofstadter. Energy levels and wave functions of Bloch electrons in rational and irrational magnetic fields. Phys. Rev. B **14**, 2239 (1976)

[90] E. Hofstetter and M. Schreiber. Statistical properties of the eigenvalue spectrum of the three-dimensional Anderson Hamiltonian. Phys. Rev. B **48**, 16979 (1993)

[91] E. Hofstetter and M. Schreiber. Relation between energy-level statistics and phase transition and its application to the Anderson model. Phys. Rev. B **49**, 14726 (1994)

[92] P. C. Hohenberg and B. I. Halperin. Theory of dynamic critical phenomena. Rev. Mod. Phys. **49**, 435 (1977)

[93] R. Hoyle. *Pattern formation. An introduction to methods* (Cambridge University Press, 2006)

[94] M. Imada, A. Fujimori, and Y. Tokura. Metal-insulator transitions. Rev. Mod. Phys. **70**, 1039 (1998)

[95] F. Izsak and I. Lagzi. Precipitate pattern formation in fluctuating media. J. Chem. Phys. **120**, 1837 (2004)

[96] F. Izsak and I. Lagzi. A new universal law for the Liesegang pattern formation. J. Chem. Phys. **122**, 184707 (2005)

[97] K. Jablczynski. La formation rythmique des précipités: Les anneaux de Liesegang. Bull. Soc. Chim. France **33**, 1592 (1923)

[98] L. Jahnke and J. W. Kantelhardt. Comparison of models and lattice-gas simulations for Liesegang patterns. Eur. Phys. J. ST **161**, 121 (2008)

[99] L. Jahnke and J. W. Kantelhardt. Consequences of fluctuations in Liesegang pattern formation. EPL **84**, 48006 (2008)

[100] L. Jahnke, J. W. Kantelhardt, R. Berkovits, and S. Havlin. Wave localization in complex networks with high clustering. Phys. Rev. Lett. **101**, 175702 (2008)

[101] S. Kadar, J. C. Wang, and K. Showalter. Noise-supported traveling waves in sub-excitable media. Nature **391**, 770 (1998)

[102] Y. Kaganovskii, A. Lipovskii, M. Rosenbluh, and V. Zhurikhina. Formation of nanoclusters through silver reduction in glasses: the model. J. Non-Cryst. Solids **353**, 2263 (2007)

[103] S. Kai, S. C. Müller, and J. Ross. Measurements of temporal and spatial sequences of events in periodic precipitation processes. J. Chem. Phys. **76**, 1392 (1982)

[104] T. Kalisky, R. Cohen, D. ben Avraham, and S. Havlin. *Lecture notes in physics: proceedings of the 23rd LANL-CNLS conference, "complex networks", Santa-Fe 2003: tomography and stability of complex networks* (Springer Berlin, 2004)

[105] A. Kaneko and T. Ohtsuki. Three-dimensional quantum percolation studied by level statistics. J. Phys. Soc. Jpn. **68**, 1488 (1999)

[106] J. W. Kantelhardt, A. Bunde, and L. Schweitzer. Extended fractons and localized phonons on percolation clusters. Phys. Rev. Lett. **81**, 4907 (1998)

[107] H. Katsuragi. Diffusion-induced spontaneous pattern formation on gelation surfaces. Europhys. Lett. **73**, 793 (2006)

[108] T. Kawarabayashi, B. Kramer, and T. Ohtsuki. Anderson transitions in three-dimensional disordered systems with randomly varying magnetic flux. Phys. Rev. B **57**, 11842 (1998)

[109] K. Kawasaki. Diffusion constants near the critical point for time-dependent Ising models. I. Phys. Rev. **145**, 224 (1966)

[110] K. W. Kehr, K. Mussawisade, G. M. Schütz, and T. Wichmann. *Diffusion in condensed matter, Chap. 18: Diffusion of particles on lattices* (Springer Berlin, 2005)

[111] J. B. Keller and S. I. Rubinow. Recurrent precipitation and Liesegang rings. J. Chem. Phys. **74**, 5000 (1981)

[112] D. E. Khmel'nitskii and A. I. Larkin. Mobility edge shift in external magnetic-field. Solid State Commun. **39**, 1069 (1981)

[113] A. Kiesow, S. Strohkark, K. Loschner, A. Heilmann, A. Podlipensky, A. Abdolvand, and G. Seifert. Generation of wavelength-dependent, periodic line pattern in metal nanoparticle-containing polymer films by femtosecond laser irradiation. Appl. Phys. Lett. **86**, 153111 (2005)

[114] C. Kitell. *Einführung in die Festkörperphysik* (R. Oldenbourg Verlag München, 1989)

[115] T. Kkarapiperis and B. Blankleider. Cellular automation model of reaction-transport processes. Physica D **78**, 30 (1994)

[116] A. Kopp, X. Jia, and S. Chakravarty. Replacing energy by von Neumann entropy in quantum phase transitions. Annals of Physics **322**, 1466 (2007)

[117] T. Koslowski and W. v. Niessen. Mobility edges for the quantum percolation problem in two and three dimensions. Phys. Rev. B **42**, 10342 (1990)

[118] Z. Koza. The long-time behavior of initially separated $A + B \to 0$ reaction-diffusion systems with arbitrary diffusion constants. J. Stat. Phys. **85**, 179 (1996)

[119] B. Kramer and A. MacKinnon. Localization: theory and experiment. Rep. Prog. Phys. **56**, 1469 (1993)

[120] H. Kronmüller and S. Parkin (editors). *Handbook of magnetism and advanced magnetic materials* (John Wiley & Sons, 2007)

[121] H. J. Krug and H. Brandtstadter. Morphological characteristics of Liesegang rings and their simulations. J. Phys. Chem. A **103**, 7811 (1999)

[122] H. Kunz and B. Souillard. On the upper critical dimension and the critical exponents of the localization transition. J. Phys. Lett. **44**, L503 (1983)

[123] A. Kusy, A. W. Stadler, G. Haldas, and R. Sikora. Quantum percolation in electronic transport of metal-insulator systems: numerical studies of conductance. Physica A **241**, 403 (1997)

[124] I. Lagzi and F. Izsak. Stochastic description of precipitate pattern formation in an electric field. Phys. Chem. Chem. Phys. **5**, 4144 (2003)

[125] I. Lagzi and F. Izsak. Regular precipitation patterns and precipitation waves in an open system. Phys. Chem. Chem. Phys. **7**, 3845 (2005)

[126] I. Lagzi and D. Ueyama. Pattern transition between periodic Liesegang pattern and crystal growth regime in reaction-diffusion systems. Chem. Phys. Lett. **468**, 188 (2009)

[127] Y. Lahini, A. Avidan, F. Pozzi, M. Sorel, R. Morandotti, D. N. Christodoulides, and Y. Silberberg. Anderson localization and nonlinearity in one-dimensional disordered photonic lattices. Phys. Rev. Lett. **100**, 013906 (2008)

[128] A. Lampert and E. Meron. Localized structures as spatial hosts for unstable modes. EPL **78**, 14002 (2007)

[129] H. Larralde, M. Araujo, S. Havlin, and H. E. Stanley. Diffusion-reaction kinetics for $A + B$(static)$\rightarrow$ C(inert) for one-dimensional systems with initially separated reactants. Phys. Rev. A **46**, R6121 (1992)

[130] M. I. Lebedeva, D. G. Vlachos, and M. Tsapatsis. Bifurcation analysis of Liesegang ring pattern formation. Phys. Rev. Lett. **92**, 088301 (2004)

[131] M. I. Lebedeva, D. G. Vlachos, and M. Tsapatsis. Pattern formation in porous media via the Liesegang ring mechanism. Ind. Eng. Chem. Res. **43**, 3073 (2004)

[132] P. A. Lee and T. V. Ramakrishnan. Disordered electronic systems. Rev. Mod. Phys. **57**, 287 (1985)

[133] M. E. Levan and J. Ross. Measurements and a hypothesis on periodic precipitation processes. J. Phys. Chem. **91**, 6300 (1987)

[134] R. E. Liesegang. Ueber einige Eigenschaften von Gallerten. Naturw. Wochschr. **11**, 353 (1896)

[135] C. D. Lorenz and R. M. Ziff. Precise determination of the bond percolation thresholds and finite-size scaling corrections for the sc, fcc, and bcc lattices. Phys. Rev. E **57**, 230 (1998)

[136] T. Lukes. Critical dimensionality in the Anderson-Mott transition. J. Phys. C **12**, L797 (1979)

[137] C. C. M. Biafore and G. Kotliar. Crossover exponent for a weak magnetic-field at the localization orthogonal fixed-point. Nucl. Phys. B **340**, 617 (1990)

[138] A. MacKinnon and B. Kramer. One-parameter scaling of localization length and conductance in disordered systems. Phys. Rev. Lett. **47**, 1546 (1981)

[139] A. MacKinnon and B. Kramer. The scaling theory of electrons in disordered solids - additional numerical results. Z. Phy. B **53**, 1 (1983)

[140] R. Madueno, M. Raisanen, C. Silien, and M. Buck. Functionalizing hydrogen-bonded surface networks with self-assembled monolayers. Nature **454**, 618 (2008)

[141] A. Manor and N. M. Shnerb. Dynamical failure of Turing patterns. Europhys. Lett. **74**, 837 (2006)

[142] K. Martens, I. Bena, M. Droz, and Z. Rácz. Encoding information into precipitation structures. J. Stat. Mech. P12003 (2008)

[143] R. Matalon and A. Packter. The Liesegang phenomenon I. Sol protection and diffusion. J. Colloid Sci. **10**, 46 (1955)

[144] Y. Meir, A. Aharony, and A. B. Harris. Delocalization transition in two-dimensional quantum percolation. Europhys. Lett. **10**, 275 (1989)

[145] M. L. Metha. *Random matrices* (Academic Press Boston, 1991)

[146] A. D. Mirlin. Statistics of energy levels and eigenfunctions in disordered systems. Phys. Rep. **326**, 260 (2000)

[147] V. F. Mitin, V. K. Dugaev, and G. G. Ihas. Large negative magnetoresistance in Ge films at ultralow temperatures and low magnetic fields. App. Phys. Lett. **91**, 202107 (2007)

[148] C. Mohr, M. Dubiel, and H. Hofmeister. Formation of silver particles and periodic precipitate layers in silicate glass induced by thermally assisted hydrogen permeation. J. Phys.: Condens. Matter **13**, 525 (2001)

[149] M. Molloy and B. Reed. The size of the giant component of a random graph with a given degree sequence. Combinatorics, Probability & Computing **7**, 295 (1998)

[150] F. Molnar, F. Izsak, and I. Lagzi. Design of equidistant and revert type precipitation patterns in reaction-diffusion systems. Phys. Chem. Chem. Phys. **10**, 2368 (2008)

[151] A. Mookerjee, B. K. Chakrabarti, I. Dasgupta, and T. Saha. Quantum percolation and breakdown – absence of the delocalization transition in 2 dimensions. Physica A **186**, 258 (1992)

[152] H. W. Morse and G. W. Pierce. Diffusion and supersaturation in gelatine. Phys. Rev. **17**, 129 (1903)

[153] M. Msharrafieh and R. Sultan. Dynamics of a complex diffusion-precipitation-redissolution Liesegang pattern. Chem. Phys. Lett. **421**, 221 (2006)

[154] S. C. Müller, S. Kai, and J. Ross. Periodic precipitation patterns in the presence of concentration gradients. 1. Dependence on ion product and concentration difference. J. Phys. Chem. **86**, 4078 (1982)

[155] S. C. Müller and J. Ross. Spatial structure formation in precipitation reactions. J. Phys. Chem. A **107**, 7997 (2003)

[156] T. Narita and M. Tokita. Liesegang pattern formation in κ-carrageenan gel. Langmuir **22**, 349 (2006)

[157] M. E. J. Newman. Assortative mixing in networks. Phys. Rev. Lett. **89**, 208701 (2002)

[158] T. Ohtsuki, K. Slevin, and T. Kawarabayashi. Review of recent progress on numerical studies of the Anderson transition. Ann. Phys. (Leipzig) **8**, 655 (1999)

[159] R. Oppermann. Magnetic-field induced crossover in weakly localized regimes and scaling of the conductivity. J. Phys. Lett. (Paris) **45**, 1161 (1984)

[160] W. Ostwald. *Lehrbuch der Allgemeinen Chemie* (Engelmann Leipzig, 1897)

[161] A. Packter. The Liesegang phenomenon. IV: Reprecipitation from ammonia peptised sols. Kolloid-Z. **142**, 109 (1955)

[162] R. Pastor-Satorras and A. Vespignani. *Evolution and structure of the Internet* (Cambridge University Press, 2004)

[163] S. Prager. Periodic precipitation. J. Chem. Phys. **25**, 279 (1956)

[164] Z. Racz. Formation of Liesegang patterns. Physica A **274**, 50 (1999)

[165] G. Roati, C. D'Errico, L. Fallani, M. Fattori, C. Fort, M. Zaccanti, G. Modugno, M. Modugno, and M. Inguscio. Anderson localization of a non-interacting Bose-Einstein condensate. Nature **453**, 895 (2008)

[166] M. Sade and R. Berkovits. Localization transition on a Cayley tree via spectral statistics. Phys. Rev. B **68**, 193102 (2003)

[167] M. Sade, T. Kalisky, S. Havlin, and R. Berkovits. Localization transition on complex networks via spectral statistics. Phys. Rev. E. **72**, 066123 (2005)

[168] F. Scheffold, R. Lenke, R. Tweer, and G. Maret. Localization or classical diffusion of light? Nature **398**, 206 (1999)

[169] M. Schreiber and H. Grussbach. Multifractal wave functions at the Anderson transition. Phys. Rev. Lett. **67**, 607 (1991)

[170] M. Schreiber and H. Grussbach. Dimensionality dependence of the metal-insulator transition in the Anderson model of localization. Phys. Rev. Lett. **76**, 1687 (1996)

[171] G. Schubert, A. Weiße, and H. Fehske. Localization effects in quantum percolation. Phys. Rev. B **71**, 045126 (2005)

[172] T. Schwartz, G. Bartal, S. Fishman, and M. Segev. Transport and Anderson localization in disordered two-dimensional photonic lattices. Nature **446**, 52 (2007)

[173] L. Schweitzer and H. Potempa. Influence of boundary conditions on level statistics and eigenstates at the metal-insulator transition. Physica A **266**, 486 (1999)

[174] M. A. Serrano and M. Boguñá. Tuning clustering in random networks with arbitrary degree distributions. Phys. Rev. E **72**, 036133 (2005)

[175] M. A. Serrano and M. Boguñá. Clustering in complex networks. I. General formalism. Phys. Rev. E **74**, 056114 (2006)

[176] M. A. Serrano and M. Boguñá. Clustering in complex networks. II. Percolation properties. Phys. Rev. E **74**, 056115 (2006)

[177] M. A. Serrano and M. Boguñá. Percolation and epidemic thresholds in clustered networks. Phys. Rev. Lett. **97**, 088701 (2006)

[178] B. Shapiro. Renormalization-group transformation for the Anderson transition. Phys. Rev. Lett. **48**, 823 (1982)

[179] B. Shapiro. Anderson transition in a magnetic-field - a possible phase-diagram. Philos. Mag. B **50**, 241 (1984)

[180] P. Sheng. *Introduction to wave scattering, localization and mesoscopic phenomena* (Springer Berlin, 2006)

[181] T. Shinbrot and F. J. Muzzio. Noise to order. Nature **410**, 251 (2001)

[182] S. Shinohar. Theory of one-dimensional Liesegang phenomena. J. Phys. Soc. Jpn. **29**, 1073 (1970)

[183] B. I. Shklovskii, B. Shapiro, B. R. Sears, P. Lambrianides, and H. B. Shore. Statistics of spectra of disordered systems near the metal-insulator transition. Phys. Rev. B **47**, 11487 (1993)

[184] Z. Shreif, L. Mandalian, A. Abi-Haydar, and R. Sultan. Taming ring morphology in 2D $\mathrm{Co(OH)_2}$ Liesegang patterns. Phys. Chem. Chem. Phys. **6**, 3461 (2004)

[185] K. Slevin and T. Ohtsuki. The Anderson transition: time reversal symmetry and universality. Phys. Rev. Lett. **78**, 4083 (1997)

[186] K. Slevin and T. Ohtsuki. Corrections to scaling at the Anderson transition. Phys. Rev. Lett. **82** (1999)

[187] K. Slevin, T. Ohtsuki, and T. Kawarabayashi. Topology dependent quantities at the Anderson transition. Phys. Rev. Lett. **84** (2000)

[188] E. Smits, S. Mathijssen, P. van Hal, S. Setayesh, T. Geuns, K. Mutsaers, E. Cantatore, H. Wondergern, O. Werzer, R. Resel, M. Kemerink, S. Kirchmeyer, A. Muzafarov, S. Ponomarenki, B. de Boer, P. Blom, and D. de Leeuw. Bottom-up organic integrated circuits. Nature **455**, 956 (2008)

[189] S. K. Smoukov, A. Bitner, C. J. Campbell, K. Kandere-Grzybowska, and B. A. Grzybowski. Nano- and microscopic surface wrinkles of linearly increasing heights prepared by periodic precipitation. JACS **127**, 17803 (2005)

[190] C. M. Soukoulis and G. S. Grest. Localization in two-dimensional quantum percolation. Phys. Rev. B **44**, 4685 (1991)

[191] C. M. Soukoulis, Q. Li, and G. S. Grest. Quantum percolation in three-dimensional systems. Phys. Rev. B **45**, 7724 (1992)

[192] A. W. Stadler, A. Kusy, and R. Sikora. Numerical studies of the Anderson transition in three-dimensional quantum site percolation. J. Phys. Cond. Mat. **8**, 2981 (1996)

[193] H. E. Stanley. Ghost fields, pair connectedness, and scaling – exact results in one-dimensional percolation. J. Phys. A **10**, L211 (1977)

[194] J. Starke, C. Reichert, M. Eiswirth, H. H. Rotermund, and G. Ertl. Fluctuation-induced pattern formation in a surface reaction. Europhys. Lett. **73**, 820 (2006)

[195] A. Stathopoulos. Nearly optimal preconditioned methods for Hermitian eigenproblems under limited memory. Part I: Seeking one eigenvalue. SIAM J. Sci. Comput. **29**, 481 (2007)

[196] M. Stoneham. How soft materials control harder ones: routes to bio-organization. Rep. Prog. Phys. **70**, 1055 (2007)

[197] M. Störzer, P. Gross, C. M. Aegerter, and G. Maret. Observation of the critical regime near Anderson localization of light. Phys. Rev. Lett. **96**, 063904 (2006)

[198] J. Straley. Conductivity near the localization threshold in the high-dimensionality limit. Phys. Rev. B **28**, 5393 (1983)

[199] R. F. Sultan. Propagating fronts in periodic precipitation systems with redissolution. Phys. Chem. Chem. Phys. **4**, 1253 (2002)

[200] J. P. G. Taylor and A. MacKinnon. A study of the two-dimensional bond quantum percolation model. J. Phys. Condens. Mat. **1**, 9963 (1989)

[201] G. A. Thomas, Y. Ootuka, S. Katsumoto, S. Kobayashi, and W. Sasaki. Evidence for localization effects in compensated semiconductors. Phys. Rev. B **25**, 4288 (1982)

[202] D. Thouless. Electrons in disordered systems and the theory of localization. Phys. Rep. **13**, 93 (1974)

[203] E. Tousson, V. Volterra, E. P. Rubenstein, R. Rosenbaum, and Z. Ovadyahu. A shift of the mobility edge at weak magnetic-fields. Philos. Mag. B **56**, 875 (1987)

[204] M. Tsapatsis, D. Vlachos, S. Kim, H. Ramanan, and G. Gavalas. Spontaneous formation of periodically patterned deposits by chemical vapor deposition. JACS **122**, 12864 (2000)

[205] A. M. Turing. The chemical basis of morphogenesis. Philos. T. Roy. Soc. B **237**, 37 (1952)

[206] A. Varshneya. *Fundamentals of inorganic glasses* (Academic Press Inc. San Diego, 1994)

[207] A. Vázquez, R. Pastor-Satorras, and A. Vespignani. Large-scale topological and dynamical properties of the Internet. Phys. Rev. E **65**, 066130 (2002)

[208] G. Venzl. Pattern formation in precipitation processes. I. The theory of competitive coarsening. J. Chem. Phys. **85**, 1996 (1986)

[209] E. Volz. Random networks with tunable degree distribution and clustering. Phys. Rev. E **70**, 056115 (2004)

[210] C. Wagner. Mathematical analysis of the formation of periodic precipitations. J. Coll. Sci. **5**, 85 (1950)

[211] M. Watanabe, K. M. Itoh, Y. Ootuka, and E. E. Haller. Metal-insulator transition of isotopically enriched neutron-transmutation-doped $^{70}\mathrm{Ge:Ga}$ in magnetic fields. Phys. Rev. B **60**, 15817 (1999)

[212] S. S. Watts, D.J. Collective dynamics of 'small-world' networks. Nature **393**, 440 (1998)

[213] F. Wegner. Phase transition in lattice surface systems with gonihedric action. Nucl. Phys. B **270**, 1 (1996)

[214] G. M. Whitesides and B. A. Grzybowski. Self-assembly at all scales. Science **295**, 2418 (2002)

[215] D. S. Wiersma, P. Bartolini, A. Lagendijk, and R. Righini. Localization of light in a disordered medium. Nature **390**, 671 (1997)

[216] D. S. Wiersma, J. G. Rivas, P. Bartolini, A. Lagendijk, and R. Righini. Localization or classical diffusion of light? Reply. Nature **398**, 207 (1999)

[217] K. Wiesenfeld and F. Moss. Stochastic resonance and the benefits of noise: from ice ages to crayfish and SQUIDs. Nature **373**, 33 (1995)

[218] E. P. Wigner. On a class of analytic functions from the quantum theory of collisions. Ann. Math. **53**, 36 (1951)

[219] J. Yuan and T. R. Kirkpatrick. Crossover-behavior for a noninteracting disordered electronic system in the presence of a weak magnetic-field. J. Stat. Phys. **64**, 309 (1991)

[220] A. G. Zabrodskii and K. Zinov'eva. Conductivity in the metal-dielectric transition range and its application in wide-range low-temperature converters. Sov. Phys. JETP **59**, 425 (1984)

[221] Y. Zeldovich, R. L. Salganik, and G. I. Barenblatt. Quasiperiodical settling of precipitates upon mutual diffusion of 2 substances (Liesegang rings). Dokl. Akad. Nauk **140**, 1281 (1961)

[222] C. Zhu and S. Xiong. Localization-delocalization transition of electron states in a disordered quantum small-world network. Phys. Rev. B **62**, 14780 (2000)

[223] M. Zrinyi, L. Galfi, E. Smidroczki, Z. Racz, and F. Horkay. Direct observation of a crossover from heterogeneous traveling wave to Liesegang pattern formation. J. Phys. Chem. **95**, 1618 (1991)

Veröffentlichungen

1. Lukas Jahnke und Stefan Leupold. Relativistic description of the $N^*(1520)$. Nuclear Physics A **778**, 53-94 (2006)
2. Lukas Jahnke und Jan W. Kantelhardt. Comparison of models and lattice-gas simulations for Liesegang pattern. European Physical Journal Special-Topics **161**, 121-141 (2008)
3. Lukas Jahnke, Jan W. Kantelhardt, Richard Berkovits und Shlomo Havlin. Wave localization in complex networks with high clustering. Physical Review Letters **101**, 175702 (2008)
4. Lukas Jahnke und Jan W. Kantelhardt. Consequences of fluctuations in Liesegang pattern formation. EPL **84**, 48006 (2008)
5. Richard Berkovits, Lukas Jahnke und Jan W. Kantelhardt. Wave localization on complex networks. Angenommen zur Veröffentlichung in Frank Emmert-Streib und Matthias Dehmer (Editoren): *Information Theory and Statistics in Complex Networks* . (Springer Berlin, 2009)
6. Lukas Jahnke, Jan W. Kantelhardt und Richard Berkovits. The effect of a small magnetic flux on the metal-insulator transition. Eingereicht bei Physical Review B
7. Lukas Jahnke and Jan W. Kantelhardt. Equidistant band formation of precipitation in a reaction-diffusion process. Eingereicht bei New Journal of Physics

Danksagung

Ich danke Herrn Prof. Jan W. Kantelhardt für die erstklassige Betreuung dieser Arbeit. Ich bin ihm dankbar für die Ermöglichung der Mitarbeit an interessanten Projekten, für die vielen guten Gespräche und wichtigen Anregungen. Neben seiner außerordentlichen fachlichen Kompetenz schätze ich auch seine freundschaftliche und offene Art.

Bei Herrn Prof. Richard Berkovits und Herrn Prof. Shlomo Havlin bedanke ich mich für ihre Impulse, Ideen und die anregenden Diskussionen. Zusätzlich möchte ich mich für die schöne Zeit in Ramat Gan und Tel Aviv bedanken.

Prof. Steffen Trimper danke ich für seine Hilfsbereitschaft bei Fragen und die Einbindung in die Theoriegruppe. Ich möchte Herrn PD Dr. Dubiel für die Zusammenarbeit, die Bereitstellung experimenteller Daten und die Durchführung von Experimenten danken. Für die Wartung des Clusters und die konstante Unterstützung bei allen Fragen danke ich Dr. Markus Däne, Michael Czerner und Steven Walczak. Für die ausgezeichnete Hilfe bei allen administrativen Dingen möchte ich mich bei Frau Helgard Meyn und Frau Daniela Lemke bedanken.

Besonders möchte ich mich bei Aicko Schumann für die gemeinsame Zeit im Büro bedanken. Danke Aicko, auch für die schönen Abende und deine Hilfe bei der Durchsicht dieser Arbeit. Ich hoffe, unsere Freundschaft hält auch weiter, wenn sich unsere Wege trennen. Bei Frau Dr. Beatrix M. Schulz bedanke ich mich für die gute Aufnahme und die freundliche Atmosphäre im Büro. Bei Christian Langheinrich bedanke ich mich für die interessanten Gespräche. Bei Ronny Bartsch möchte ich mich für die Bereicherung meiner Zeit in Israel bedanken. Die vielen anregenden Gespräche beim Mittagessen und in der Freizeit habe ich immer genossen. Allen Kollegen der Fachgruppe Theorie danke ich für das angenehme Arbeitsklima.

Ich möchte mich bei der Deutschen Forschungsgemeinschaft bedanken, die mir im Rahmen des SFB 418 die Anfertigung dieser Arbeit ermöglicht hat. Auch der Minerva Stiftung gilt mein Dank für die großzügige finanzielle Unterstützung meiner Zeit in Israel.

Und nicht zuletzt danke ich meiner Frau Sonja für ihre Geduld und Motivation. Danke, dass du an mich glaubst und mich immer unterstützt. Bei meinen Töchtern Talea und Madita möchte ich mich bedanken, dass sie es immer wieder geschafft haben, mich von der Physik abzuholen in ihre Welt. Bei meinen Eltern und Schwiegereltern möchte ich mich für ihre Unterstützung bedanken. Schön, dass Ihr immer für mich da seid.

Eidesstattliche Erklärung

Hiermit erkläre ich, dass ich keine anderen als die von mir angegebenen Quellen und Hilfsmittel zur Erstellung meiner Dissertation verwendet habe. Den benutzten Werken wörtlich oder inhaltlich entnommene Stellen sind als solche gekennzeichnet. Ich erkläre, die Angaben wahrheitsgemäß gemacht und die wissenschaftliche Arbeit an keiner anderen wissenschaftlichen Einrichtung zur Erlangung eines akademischen Grades eingereicht zu haben.

Lukas Jahnke
Halle (Saale), den 28. Mai 2009

Lebenslauf

Lukas Jahnke
Humboldtstr. 10
06114 Halle (Saale)

Persönliche Daten

Name:	Lukas Jahnke
Geburtsdatum:	28. September 1978
Geburtsort:	Manna (Indonesien)
Staatsangehörigkeit:	deutsch
Familienstand:	verheiratet, zwei Kinder

Ausbildung

seit März 2006	Promotion zum Dr. rer. nat am Lehrstuhl Computational Nanosciences, Fachbereich Physik, Martin-Luther-Universität Halle-Wittenberg
2004 bis 2005	Diplomarbeit: Theoretische Hadronenphysik Thema: Complete relativistic description of the $N^*(1520)$ resonance
1999 bis 2005	Studium der Physik an der Justus-Liebig-Universität Gießen Abschluss: Diplom Physiker
2002 bis 2006	Studium der Mathematik an der Justus-Liebig-Universität Gießen Abschluss: Vordiplom
1998	Allgemeine Hochschulreife, erworben in Bremen

Lukas Jahnke
Halle (Saale), den 28. Mai 2009